

Czech technical university in Prague
Faculty of nuclear sciences and physical
engineering

Department of physics
Programme: Nuclear and particle physics



Study of Upsilon meson production
dependence on charged particle
multiplicity in $p+p$ collisions
measured with the STAR experiment

DIPLOMA THESIS

Author: Bc. Jakub Češka
Supervisor: Leszek Kosarzewski, BEng., Ph.D.
Year: 2022

České vysoké učení technické v Praze
Fakulta jaderná a fyzikálně inženýrská

Katedra fyziky
Program: Jaderná a částicová fyzika



Studium závislosti produkce Upsilon
mezonů na multiplicitě nabitých
částic v $p+p$ srážkách měřených na
experimentu STAR

DIPLOMOVÁ PRÁCE

Vypracoval: Bc. Jakub Češka
Vedoucí práce: Leszek Kosarzewski, BEng., Ph.D.
Rok: 2022



Katedra: fyziky

Akademický rok: 2021/2022

ZADÁNÍ DIPLOMOVÉ PRÁCE

Student: Bc. Jakub Češka

Studijní program: Jaderná a částicová fyzika

Název práce: Studium závislosti produkce Upsilon mezonů na multiplicitě nabitých částic v p+p srážkách měřených na experimentu STAR
(česky)

Název práce: Study of Upsilon meson production dependence on charged particle multiplicity in p+p collisions measured with the STAR experiment
(anglicky)

Pokyny pro vypracování:

1. Relativistic heavy-ion collisions
2. Upsilon production at RHIC and LHC
3. STAR experiment at RHIC
4. Upsilon signal reconstruction
5. Efficiency corrections
6. Upsilon yield dependence on charged particle multiplicity
5. Results and discussion

Doporučená literatura:

- [1] A. M. Sirunyan, et al.: Investigation into the event-activity dependence of Upsilon(nS) relative production in proton-proton collisions at $\sqrt{s} = 7$ TeV. JHEP, 2020(11), 1
- [2] A. Andronic, et al.: Heavy-flavour and quarkonium production in the LHC era: from proton-proton to heavy-ion collisions. EPJC, 76(3), 107
- [3] L. Kosarzewski: Overview of Upsilon production studies performed with the STAR experiment. PoS(ICHEP2020), Vol. 390, p. 545
- [4] E. Levin, I. Schmidt and M. Siddikov: Multiplicity dependence of quarkonia production in the CGC approach. Eur. Phys. J. C, 80(6), 560
- [5] J. Adam, et al.: J/ψ production cross section and its dependence on charged-particle multiplicity in p+p collisions at $\sqrt{s} = 200$ GeV. Phys. Lett. B, 786, 87–93

Jméno a pracoviště vedoucího diplomové práce:

Mgr. Ing. Leszek Kosarzewski, Ph.D., Katedra fyziky,
Fakulta jaderná a fyzikálně inženýrská ČVUT v Praze

Kontultant: doc. Mgr. Jaroslav Bielčík, Ph.D., Katedra fyziky,
Fakulta jaderná a fyzikálně inženýrská ČVUT v Praze

Datum zadání diplomové práce: 20.10.2021

Termín odevzdání diplomové práce: 02.05.2022

Doba platnosti zadání je dva roky od data zadání.



.....
garant studijního programu


.....
vedoucí katedry
.....
děkan

V Praze dne 20.10.2021

Prohlášení

Prohlašuji, že jsem svou diplomovou práci vypracoval samostatně a použil jsem pouze podklady (literaturu, projekty, SW atd.) uvedené v příloženém seznamu.

Nemám závažný důvod proti použití tohoto díla ve smyslu § 60 Zákona č. 121/1200 Sb., o právu autorském, o právech souvisejících s právem autorským a o změně některých zákonů (autorský zákon).

V Praze dne

.....
Bc. Jakub Češka

Acknowledgement

First of all, I would like to thank to the two people most responsible for this thesis seeing the light of day, Dr. Leszek Kosarzewski and doc. Jaroslav Bielčík, for their patience, understanding and very valuable leadership. Additionally, I would like to appreciate my friends and family, all of the people close to me, for their support and belief. This helped me to complete the thesis.

Bc. Jakub Češka

Název práce:

Studium závislosti produkce Upsilon mezonů na multiplicitě nabitých částic v p+p srážkách měřených na experimentu STAR

Autor: Bc. Jakub Češka

Studijní program: Jaderná a částicová fyzika

Druh práce: Diplomová práce

Vedoucí práce: Leszek Kosarzewski, BEng., Ph.D.
Katedra fyziky, Fakulta jaderná a fyzikálně inženýrská,
České vysoké učení technické v Praze

Konzultant: doc. Mgr. Jaroslav Bielčík, Ph.D.
Katedra fyziky, Fakulta jaderná a fyzikálně inženýrská,
České vysoké učení technické v Praze

Abstrakt: Studium závislosti výtěžku kvarkonií na multiplicitě nabitých částic slouží k pochopení produkčních mechanismů kvarkonií, zlepšení modelů jejich produkce a zkoumání propojení mezi tvrdými a měkými procesy. Tato práce představuje analýzu měření Υ mezonu v proton-protonových srážkách při 510 GeV těžištové energii, které byly naměřeny detektorem STAR v průběhu Run 17. Nebyl pozorován žádný signál v rekonstrukci provedené pouze pomocí dostupných TPC dat. Byla provedena studie pomocí Monte Carlo generátoru PYTHIA, zaměřená na zkoumání jednotlivých stavů Υ mezonu a jejich produkce pomocí feed-down efektu. Nebyly pozorovány rozdíly v závislosti na multiplicitě pro jednotlivé stavy Υ mezonu. Podobně, nebyly pozorovány rozdíly mezi přímo produkovanými Υ mezony a těmi z rozpadu excitovaných stavů.

Klíčová slova: Upsilon mezon, experiment STAR, proton-protonové srážky, multiplicita

Title:

Study of Upsilon meson production dependence on charged particle multiplicity in p+p collisions measured with the STAR experiment

Author: Bc. Jakub Češka

Abstract: The study of quarkonium yield dependence on charged particle multiplicity serves to help our understanding of quarkonium production mechanism, improve the production models and to investigate a link between hard and soft processes involved. This thesis presents an analysis of Υ meson production in 510 GeV centre-of-mass energy proton-proton collisions recorded by the STAR experiment during Run 17. No signal was observed when reconstructed with only the available TPC information. A PYTHIA Monte Carlo event generator study of the Υ meson states and their feed-down contribution is performed. No difference for each Υ state was observed in the normalised multiplicity dependence in the simulations. Similarly, no difference was observed for directly produced Υ mesons compared to those originating from excited state feed-down.

Key words: Upsilon meson, STAR experiment, proton-proton collisions, multiplicity

Contents

Introduction	13
1 Relativistic hadron collisions	15
1.1 Standard model of particle physics	15
1.1.1 Fermions	16
1.1.2 Bosons	19
1.1.3 Problems of the Standard Model	21
2 Quarkonia	23
2.1 Introduction to quarkonia	23
2.2 Bottomonia	24
2.3 Production	29
2.3.1 Colour Singlet Model	30
2.3.2 Colour Octet Model	31
2.3.3 Colour Evaporation Model	31
2.3.4 Colour Glass Condensate + non-relativistic QCD	32
2.4 Quarkonium suppression	32
2.5 Multiplicity dependence of quarkonium production	33
3 Recent results of quarkonia measurements	35
3.1 Cross section transverse momentum and rapidity dependence	35
3.1.1 J/ψ meson spectra	35
3.1.2 Υ meson spectra	39
3.2 Quarkonium yield event multiplicity dependence	43
3.2.1 J/ψ meson multiplicity dependence	43
3.2.2 Υ meson multiplicity dependence	44
4 The STAR experiment	47
4.1 RHIC	47
4.2 STAR	49
4.2.1 Time Projection Chamber	51
4.2.2 Barrel Electromagnetic Calorimeter	52
5 Monte Carlo simulations of Upsilon meson production	56
5.1 Monte Carlo event generators	56
5.2 Simulation	58
6 Experimental data analysis	64

6.1	Software and resources	64
6.2	Dataset	65
6.3	Data analysis	66
6.3.1	Event selection	66
6.3.2	Track selection	68
6.3.3	Electron and positron identification	70
6.3.4	Candidate reconstruction	73
6.3.5	Charged particle multiplicity	74
6.4	Tests and validation of data reproduction	75
7	Results and discussion	80
	Conclusion	83
	Bibliography	85

List of Figures

1.1	Standard Model	17
2.1	Bottomonium family	25
2.2	Υ meson sources	28
2.3	Quarkoniums production	29
3.1	STAR and PHENIX J/ψ cross section measurements	36
3.2	PHENIX J/ψ cross section measurement	37
3.3	STAR J/ψ cross section measurement	38
3.4	ALICE J/ψ cross section measurement	39
3.5	STAR Υ cross section measurement	40
3.6	STAR Υ cross section measurement	41
3.7	CMS Υ cross section measurement	42
3.8	STAR J/ψ multiplicity dependence measurement	43
3.9	ALICE J/ψ multiplicity dependence measurement	44
3.10	STAR Υ multiplicity dependence measurement	45
3.11	STAR Υ multiplicity dependence measurement	45
3.12	ALICE J/ψ and Υ multiplicity dependence measurement	46
4.1	RHIC accelerator complex	49
4.2	STAR detector scheme	50
4.3	TPC detector schematic	53
4.4	STAR detector schematics	54
4.5	BEMC tower schematic	55
5.1	Multiplicity spectra generated by PYTHIA	59
5.2	p_T spectra generated by PYTHIA	60
5.3	Multiplicity and p_T spectra generated by PYTHIA	61
5.4	$\Upsilon(1S)$ multiplicity dependence generated by PYTHIA	62
5.5	$\Upsilon(1S)$ multiplicity dependence generated by PYTHIA	62
5.6	$\Upsilon(2S)$ multiplicity dependence generated by PYTHIA	63
5.7	$\Upsilon(3S)$ multiplicity dependence simulated by PYTHIA	63
5.8	$\Upsilon(1S)$, $\Upsilon(2S)$ and $\Upsilon(3S)$ multiplicity dependence simulated by PYTHIA	63
6.1	Selected number of events by event acceptance steps	67
6.2	$nHitsFit$ distributions	69
6.3	$nHitsRatio$ distributions	69
6.4	DCA_x vs DCA_y distributions	70
6.5	p_T distributions	70

6.6	dE/dx vp p distribution	71
6.7	$n\sigma$ vs p distributions	72
6.8	Invariant mass spectra	75
6.9	$TofMult$ distribution	76
6.10	E_{CLU} distribution	76
6.11	L0 $DSMadc$ distribution	77
6.12	L0 $DCMadc$ vs $towerID$ distribution	78
6.13	E_{CLU} vs E_{TOW} distribution	78
6.14	E_{CLU} vs p distribution	79
7.1	Invariant mass spectra from J/ψ analysis	81
7.2	Invariant mass spectrum from J/ψ analysis after background subtraction	82

List of Tables

1.1	Properties of quarks	18
1.2	Properties of leptons	18
1.3	Properties of bosons	19
2.1	Spectroscopic notation	24
2.2	Υ meson properties	26
2.3	χ_{b0} properties	27
2.4	χ_{b1} properties	27
2.5	χ_{b2} properties	28
6.1	Event selection cuts	67
6.2	Track selection cuts	68
6.3	Electron selection cuts	73
6.4	Υ candidate reconstruction cuts	74
6.5	<i>TofMult</i> cuts	75

Introduction

The study of quarkonia in relativistic proton-proton collisions is an important part of today's high energy experiments. Due to the early formation of the heavy quark-antiquark pair, which they are made of, they are utilised in studying the quark gluon plasma in heavy ion collisions. This allows the measurement of such plasma due to quarkonia interacting with the plasma via the strong interaction. Measurements of quarkonium production in proton-proton collisions serves as a baseline for studies in heavy ion collisions. Furthermore, the proton-proton collisions create a small system, which may be used for the study of the production mechanism involved in the pair creation and bound state formation.

The dependence of quarkonium yield on charged particle event multiplicity has been observed to be strong, rising at a faster than linear rate. It may be linked to several phenomena connected with proton-proton collisions, such as multi-parton interactions, colour glass condensate initial conditions or string percolation. It may also help in the development of phenomenological models used for describing the transformation of a heavy quark and antiquark into a quarkonium and the interplay between soft and hard processes involved in its production.

This thesis summarises the work done in analysing the proton-proton collisions at 510 GeV centre-of-mass energy recorded by the STAR detector during its Run17. Firstly, a general theoretical framework on the basis of particle physics, the Standard Model, is introduced. Furthermore, an overview of quarkonium states is presented. This includes the discussion of bottomonia - bound states of $b\bar{b}$, the quarkonium production models, quarkonium suppression and the dependence of quarkonium yield on event multiplicity. An overview of recent measurements performed at the LHC and RHIC particle colliders is compiled and described. Additionally, the RHIC particle collider and the STAR experiment are introduced and the technical details discussed.

This thesis also includes the study of the Υ meson yield in dependence on charged particle multiplicity performed using the Monte Carlo event generator PYTHIA. This study investigates the comparison between the $\Upsilon(1S)$, $\Upsilon(2S)$ and $\Upsilon(3S)$ states, as well as the influence of the feed-down effect contributions. These results, produced as a result of collaborative work, where the author trained other collaborators in running the simulations, are presented in Chapter 5. They were presented at the 10th International Conference on New Frontiers in Physics (ICNFP 2021) and the proceedings were submitted to the *Physica Scripta* journal for publication.

The analysis of Υ meson yield performed with the data recorded by the STAR detector is introduced and described. The thesis discusses the various steps included in the analysis. Also described is the author's contribution towards the reproduction of the data, which needed to be performed by the STAR collaboration, as the original dataset did not include the information from the Barrel Electromagnetic Calorimeter. The results of the analysis and the outlook are presented.

Chapter 1

Relativistic hadron collisions

1.1 Standard model of particle physics

Before delving into the properties of the Υ meson, it is important to review the groundwork of particle physics. Since the 19th century the physicists of the world have been trying to form a description of the fundamental building blocks of the universe. Nowadays, the wide scientific community accepts one unified description of most of the observed phenomena on an elementary level - the so called "**Standard Model** (SM) of particle physics."

The development of the Standard Model occurred in the latter half of the 20th century with both theoretical and experimental contributions playing a key role. Currently it is considered theoretically self-consistent and agrees closely with most experimental predictions and observables. However, there are some phenomena, which remain unexplained (such as the baryon asymmetry), and the matter of gravity is not addressed in the framework of the model.

Any theory attempting to offer a complete picture of the physical aspects of the universe has to reflect that in our current understanding, there are four fundamental forces, which act on all of the particles present in the universe: *weak (nuclear) force*, *strong (nuclear) force*, *electromagnetic force* and *gravity*. The first three forces listed can all be formulated in the framework of quantum field theory (QFT), with the weak interaction and electromagnetism being united in a unified description called a electroweak interaction - essentially meaning that they are two different manifestations of a one single force. This has been confirmed by experimental observations. There are also attempts at formulating a Grand Unified Theory (GUT) - a model where at high energies the electroweak and strong interactions are unified (much in a similar matter as the electroweak description.) The predicted energies in the order of magnitude of 10^{15} GeV [1] lay outside the possibilities offered by current experimental methods and thus the GUT has to remain without any corroborative data. Since the Standard Model is built up from the cornerstone of the quantum mechanics (QM), it offers a description containing all three of the so far discussed forces (strong, weak and electromagnetic).

This leaves just one of the interactions unaddressed - gravity. Here the Standard Model falls short. All attempts at unifying the general relativity (the theoretical framework currently accepted as a description of gravity) with the quantum field theory - the mythical Theory of Everything (TOE) - have so far come up empty handed. The issues often lay in the inability to confirm any predictions experimentally. Therefore, the Standard Model as is now, is still an incomplete picture of the universe and further theories continue to be developed. Nevertheless, it is very successful in some aspects - e.g. the Quantum Electrodynamics (QED) part of the SM offers extremely precise and experimentally verified observables, such as the magnetic moment of the electron.

The fundamental forces described by the Standard Model offer only half of the picture - there are also particles, which are governed by these interactions. There are many ways, by which we can categorise particles contained in the model - their spin, the forces, which influence them, even their generations. The matter of the number of the particles (such as the number of gluons - it is one actual particle, but with eight independent colour combinations) is also open to interpretation. These questions will be addressed in the following subsections, which will try to shine the light at the elementary building blocks of the universe.

Particles are characterised by their quantum numbers. These include among others spin, parity, electric charge, colour charge and mass. Spin is one of these fundamental properties of particles. It is a quantum number used to represent particle's inherent angular momentum. Its SI unit is $\text{N}\cdot\text{m}\cdot\text{s}$, but by dividing the spin angular momentum by the reduced Planck constant \hbar a dimensionless quantity is derived. This value is commonly used in particle physics. It is helpful in dividing the Standard Model particles into two distinct groups with different properties: **fermions**, which have a half-integer spin value and follow the Fermi-Dirac statistics, and **bosons** with a full-integer spin described by the Bose-Einstein statistics. This is connected to the symmetric and antisymmetric properties of their wavefunctions in a system with indistinguishable particles. A brief scheme showing the particles of the Standard Model is shown on Fig. 1.1.

1.1.1 Fermions

As mentioned in the previous paragraph, a fermion is generally any half-integer spin particle. All of the fermions contained in the Standard Model have a spin value of $1/2$. The model includes two distinct groups of fermions: **quarks** and **leptons**. The main difference between those two groups of particles is whether they interact via the strong interaction - quarks do, whereas leptons do not. There are 6 quarks and 6 leptons currently recognised in the Standard Model, which are divided into three generations. Additionally, each of those particles has a corresponding antiparticle. It has the same mass as the particle, but opposite physical charges (such as the electrical charge, colour charge or the weak isospin). In total, there are 12 fundamental fermionic particles and 12 antiparticles.

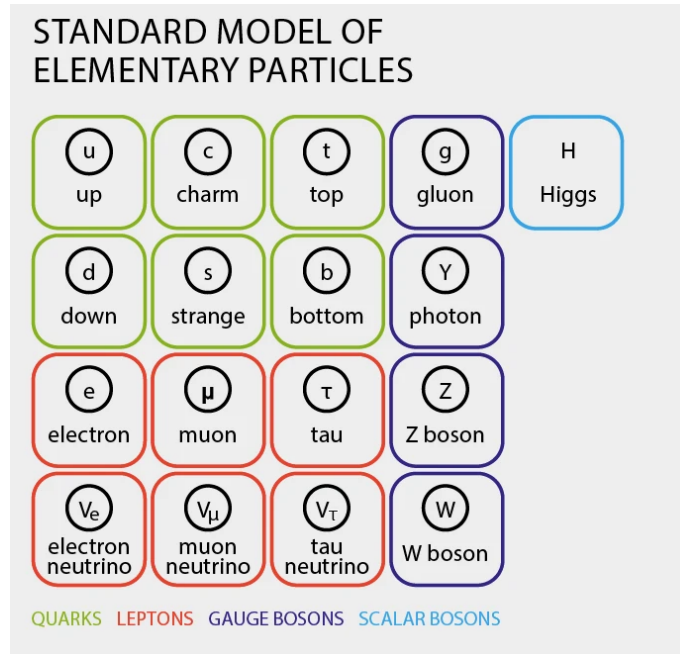


Figure 1.1: A scheme illustrating the Standard Model particles. Taken from [2].

Quarks

Quarks are the only particles in the Standard Model, which can interact via all of the four fundamental forces. Furthermore, they are the only known particles to have a non-integer electric charge (in multiples of the elementary electric charge e). Since they interact via the strong nuclear force, they possess a physical charge named *colour* (or *colour charge*). This quantity has three possible values for quarks (called *red*, *green* and *blue*) and three 'opposite' for antiparticles (*anti-red*, *anti-green* and *anti-blue*). The field of study, which is concerned with the phenomenology of the strong interaction, is called the Quantum Chromodynamics (QCD). Due to a phenomenon called *colour confinement*, which is linked to the strong interaction, they can not exist freely under the Hagedorn temperature ($T_H \sim 150$ MeV [3]). Instead, they are bound in 'colourless', composite particles - hadrons. These are mostly *mesons*, which are comprised of a single quark and an antiquark, and *(anti)baryons*, which are comprised of three (anti)quarks. There have been confirmed heavier hadrons; the tetraquarks [4] (comprised of two quarks and two antiquarks) and the pentaquarks [5] (made of four quarks and one antiquark). However these are rare and have been observed only under laboratory conditions. Their structure is being studied in order to reveal, whether their coupling is a strong quark one, or a weak baryon-meson or meson-meson one.

Each generation of quarks contains one with a positive, $2/3 e$ electric charge and one with a negative, $-1/3 e$ electric charge. As mentioned before, there are three generations of quarks currently contained in the Standard Model. The vast majority of the universe is comprised only of the u and d quarks (the proton contains two u quarks and one d quark, whereas the neutron is made of one u quark and two d quarks), as the other ones gradually decay into these lighter, more stable ones via

the weak interaction. A brief overview of the quarks can be seen on Tab. 1.1.

Quark	q [e]	m [MeV/ c^2]	generation
d (down)	-1/3	$4.7^{+0.5}_{-0.3}$	I
u (up)	2/3	$2.2^{+0.5}_{-0.4}$	I
s (strange)	-1/3	95^{+9}_{-3}	II
c (charm)	2/3	1275^{+25}_{-35}	II
b (bottom/beauty)	-1/3	4180^{+30}_{-40}	III
t (top/truth)	2/3	173000 ± 400	III

Table 1.1: Overview of the quarks and their electric charge q , mass m and generation. The values are taken from [6].

Leptons

Unlike the quarks, the leptons do not interact via the strong nuclear force. Generally, all leptons interact only via gravity and the weak interaction. Additionally, leptons can be split into two categories (containing three particles each) - *charged* and *neutral* leptons. The charged leptons carry an electric charge (meaning they are under the influence of electromagnetism), whereas the neutral ones do not. As the quarks, they are also split into three generations - each containing a charged lepton and its neutral counterpart (called a neutrino) - and each one has a corresponding antiparticle. The neutrinos have been confirmed to possess mass [7], but the exact value is not certain. Only the upper bound is currently known and the measurements continue to lower the value [8]. An overview is shown in Tab. 1.2.

Lepton	q [e]	m [MeV/ c^2]	generation
e (electron)	-1	$0.5109989461 \pm 0.0000000031$	I
μ (muon)	-1	$105.6583745 \pm 0.0000024$	II
τ (tau/tauon)	-1	1776.86 ± 0.12	III
ν_e (electron neutrino)	0	< 0.0000008 [8]	I
ν_{μ} (muon neutrino)	0	< 0.0000011	II
ν_{τ} (tau/tauon neutrino)	0	< 0.0000011	III

Table 1.2: Overview of the leptons and their electric charge q , mass m and generation. The values (except for the electron neutrino mass, which is cited from [8]) are taken from [6].

1.1.2 Bosons

The other main group of particles contained in the Standard Model of particle physics are the aforementioned bosons with a full-integer spin value. Based on this value they can be further categorised as either *scalar* bosons ($S = 0$) or *vector* bosons ($S = 1$). While there is nothing fundamentally prohibiting the existence of a higher spin value elementary boson (e.g. a *tensor* boson with $S = 2$), there have been no measurements suggesting their presence. If fermions are the particles making up the matter of the universe, bosons (often called gauge bosons), act as the carriers of the fundamental forces. In the frame of quantum field theory, any interaction (either electromagnetic, strong or weak) between particles is essentially an exchange of a gauge boson. The current Standard Model contains *gluons* g (present in 8 distinct colour states), *photon* γ , the W^\pm *bosons*, the Z^0 *boson* and the *Higgs boson* H^0 . An overview is shown in Tab. 1.3.

Lepton	S	q [e]	m [MeV/ c^2]
g (gluon)	1	0	< 1.3
γ (photon)	1	$< 10^{-35}$	$< 10^{-24}$
W^\pm (W boson)	1	± 1	80379 ± 12
Z^0 (Z boson)	1	0	91187.6 ± 2.3
H^0 (Higgs boson)	0	0	125250 ± 170

Table 1.3: Overview of the bosons and their spin S , electric charge q , mass m and generation. The values are taken from [6].

Photon

Photon is a stable massless vector boson, which acts as the force carrier for the electromagnetic interaction. The manifestation of the electromagnetic force is an exchange of a photon between two particles, which have an electric charge. These photons carry energy (in a form of momentum p , since they are massless), as well as the spin and orbital angular momenta. The fact, that the photon is massless is an implied assumption in the Standard Model of particle physics. The current upper limit on the photon mass given by the Particle Data Group (PDG) [6] is $m < 10^{-18}$ eV. It is described via the Quantum Electrodynamics, which is an abelian group theory, using an unitary symmetry group $U(1)$ with one gauge field.

Gluons

As the photon is the mediator of the electromagnetic interaction, the gluon serves the same role for the strong nuclear force. Instead of interacting with the electromagnetic charge it instead interacts with the colour charge - therefore it has zero electrical charge. It is similarly a massless scalar boson, where the zero mass is also a theoretical assumption and the actual upper bound is $1.3 \text{ MeV}/c^2$ [6]. Since the strong interaction is described via QCD using a special unitary group $SU(3)$, the

gluon can be thought of as carrying both colour and anticolour (compared to colour for quarks and anticolour for antiquarks) and it can find itself in eight different states (which form a so called colour octet). This can be represented in multiple ways, for example:

$$\begin{aligned}
 & (r\bar{b} + b\bar{r})/\sqrt{2} & (b\bar{g} + g\bar{b})/\sqrt{2} \\
 & -i(r\bar{b} - b\bar{r})/\sqrt{2} & -i(b\bar{g} - g\bar{b})/\sqrt{2} \\
 & (r\bar{g} + g\bar{r})/\sqrt{2} & (r\bar{r} - b\bar{b})/\sqrt{2} \\
 & -i(r\bar{g} - g\bar{r})/\sqrt{2} & (r\bar{r} + b\bar{b} - 2g\bar{g})/\sqrt{6}.
 \end{aligned} \tag{1.1}$$

***W* and *Z* bosons**

The last fundamental interaction contained in the Standard Model, the weak force, is in many ways unique compared to the other two. It is the only force, which can change the *flavour* of the Standard Model fermions (i.e. changing the type of quark or lepton), unlike the others violates parity and charge-parity symmetry and the particles, which mediate it, the *W* and *Z* bosons are massive (the photon and gluon are considered to be massless). It is often split into electrically charged currents (the exchange of an electrically charged *W* boson, which has either a positive or negative elementary charge) and electrically neutral currents (where the chargeless *Z* boson is exchanged). Their exceptionally heavy mass (over 80 GeV/*c*² - for a precise value see Tab. 1.3) results in a short lifetime of less than 10⁻²⁴ s [6]. Their mass is caused by the Higgs mechanism, which will be discussed in the following text. The name 'weak force' stems from the value of its coupling constant (which is a measure of the strength/frequency of the interaction): it is around 10⁻⁶ to 10⁻⁷, whereas for electromagnetism it is about 10⁻² and for strong interaction it is 1 [6]. The weak interaction acts on all fundamental fermions, as well as the Higgs boson.

Higgs boson

The Higgs boson *H*⁰ is the newest addition to the particle physics' Standard Model. Theorised as a key part of the subsequently called Higgs mechanism in 1964 and named after Peter Higgs, one of the scientists responsible for this theory, it has been confirmed by the ATLAS collaboration at the CERN's Large Hadron Collider (LHC) in 2012 [9]. Its mass (as is the case with all of the particles after all) is subject to change with new measurements, with the value given by the PDG, an average of documented measurements, being *m*_{*H*⁰} = 125.25 ± 0.17 GeV/*c*² [6] and one of the most recent values (measured in the diphoton decay channel, *H*⁰ → γγ) given as *m*_{*H*⁰} = 125.78 ± 0.16 GeV/*c*² [10].

The Higgs mechanism is essential in explaining the mass generation for gauge bosons. Without this part of the theoretical framework, all of the bosons would be massless, which is inconsistent with the measurements for *W*[±] and *Z*⁰ bosons. The mechanism can be simplified as adding another quantum field (called a Higgs field) to the

field theory used to build the model. This field, below some temperature (which is extreme in relation to the present universe), causes spontaneous symmetry breaking, triggering the mechanism and causing the bosons interacting with the field to gain mass. Within the Standard Model this mechanism refers explicitly to the electroweak symmetry breaking by the W and Z bosons.

1.1.3 Problems of the Standard Model

As mentioned before, the Standard Model is not a complete theory linking all the physical aspects of the universe. The most obvious issue, which has already been discussed in this chapter, is the matter of gravity. Gravity is the fourth fundamental force and the only one, which is not included in this model's framework. There have been proposals to extend this model to include gravity by adding another gauge boson - the tensor *graviton*. This would be a natural assumption based on all of the previous forces implemented in the model. However, this is not consistent with experimental measurements, without having to change the Standard Model in a greater extent (and no such way has been found yet). The matter of unifying the quantum field theory (the basis of the SM) with the general relativity (a theory being considered the most successful description of gravity to date) has been the subject of many attempts. One of the most noteworthy to date has been string theory. Nonetheless, no such complete theory has produced convincing predictions so far.

Another matter is the problem of the baryon asymmetry. While a world made of particles, rather than antiparticles, may be naively natural, there is no inherent reason why this should be. By the predictions given by the Standard Model, at the beginning of the universe matter and antimatter should have been created in equal amounts (given by an assumption, that the initial conditions did not involve a significant abundance of matter). Nevertheless, this is not the case and there is no convincing theory explaining this phenomenon.

While this thesis focuses on studying the Standard Model in laboratory setting, a particle accelerator, there is another vast area of particle physics - cosmology. Cosmological observations indicate, that only a small fraction (about 5% [6]) of the energy of the universe is in the form of the SM particles. another 26% [6] should be in a form of dark matter - particles behaving similarly to the Standard Model ones, but with fields, which interact very weakly with the fields described by the usual quantum field theory of the SM. The remaining 69% [6] are believed to be dark energy, a constant vacuum energy. The measurements have found no convincing dark matter particles and there is no theory of dark energy which gives predictions in similar orders of magnitude compatible with the Standard Model.

There is also the matter of the neutrino mass. As mentioned in section 1.1.1, the upper limit of the neutrino mass is given (in the order of eV). This is consistent with experimental measurements, since neutrino oscillations (which require massive neutrinos) have been confirmed. Yet, this is not consistent with the Standard Model, as it requires massless neutrinos and adding their mass afterwards creates additional

theoretical problems due to their small mass. The exact mechanism, which could be responsible for the neutrino mass is also not obvious.

Chapter 2

Quarkonia

2.1 Introduction to quarkonia

Since the 1950s, physicists have been studying a bound state of an electron and its antiparticle, the positron, in order to gain an insight into the bound states in the quantum field theory. This state is called a *positronium*. The suffix *-onium* has since been adopted to refer to any bound state of a particle and its corresponding antiparticle (except for muon-antimuon, which is called the 'true muonium'). **Quarkonia** can be thus understood as a bound state of a quark and its antiquark, which form a flavourless meson. In practice, only the charm and bottom quark-antiquark states have been called quarkonia (**charmonia** and **bottomonium** respectively), as the physical states consisting of lighter quarks (u , d and s) have only been experimentally observed as quantum mechanical mixtures of the lighter quark states. Since the c and b quarks have significantly higher masses (an order of magnitude, as stated in Tab. 1.1), their quark-antiquark pairs form a well defined states in terms of flavour. The t quark, which is two orders of magnitude heavier than c or b , is not expected to form any naturally occurring bound states (since it decays faster than any such state can be formed) and no such states have measured; therefore, no *toponia* exist.

Charmonia are therefore mesons (compound particles formed by one quark and one antiquark) with the composition $c\bar{c}$ and bottomonium $b\bar{b}$. While their composition may not indicate this, there is a variety of states in each of the families. The reason is, that the particles may occupy different quantum states, changing their properties, such as mass, lifetime or binding energy. A commonly used way to uniquely represent the quantum state of one particular quarkonium is the so called **term symbol**, which takes into account the angular momentum quantum numbers and the LS coupling - a relativistic interaction between a particle's spin and a magnetic field generated by its motion inside a potential. It takes the form of:

$$n^{2S+1}L_J, \tag{2.1}$$

where S is the *total spin quantum number*, L the *total orbital momentum quantum*

number and J the total orbital momentum quantum number. n signifies the number of the particular state with the same quantum configuration (ordered by their ascending mass). For the orbital number L a letter is usually used in the so called *spectroscopic notation*, where the numerical value is instead represented via a capital letter. An overview of the values used for quarkonia can be seen in Tab. 2.1.

L	letter
1	S
2	P
3	D

Table 2.1: An overview of the spectroscopic notation, which assigns a letter to each total orbital momentum number L .

Quarkonia can also be referred to by their name, with the specific nL appended to it in brackets. An illustration can be the $\Upsilon(1S)$, which can be equivalently understood as the 1^3S_1 bottomonium state. This thesis uses the *name(nL)* naming nomenclature.

Furthermore, there are other quantum numbers, which are important when examining particles' properties. These include, but are not limited to, the *isospin* I , the P-parity P (related to the parity transformation), the C-parity C (referring to the charge conjugation) and the G-parity G (a generalisation of the C-parity to isospin multiplets [11]). These quantities are represented in the

$$I^G(J^{PC}) \tag{2.2}$$

format and will be also listed later in the thesis when bottomonium states will be discussed.

2.2 Bottomonia

Bottomonia, or the *bottomonium family*, are aforementioned $b\bar{b}$ bound states. An illustration of most of the bottomonia (all bottomonia under the $B\bar{B}$ threshold, which will be discussed later) is shown of Fig. 2.1. As can be seen, the states are split into six distinct columns according to their J^{PC} state. Before introducing the particles further, few things need to be said about resonances in high energy physics and their widths.

In high energy physics scattering experiments are used among other things to search for particles. The results of such measurements can be used to plot a spectrum of differential cross section, which is dependent on energy. This is called a formation experiment, which studies the dependence of cross section on collision energy, in contrast to a production experiment, aimed at measuring the invariant mass distribution of a system of particles. If a peak in the differential cross section plot is found

around a certain energy, it may be an indication of a particle existing in this region. This peak can be called a resonance. In practical use, the term *resonance* refers to short-lived particles with a *mean lifetime* $\tau < 10^{-23}$ s.

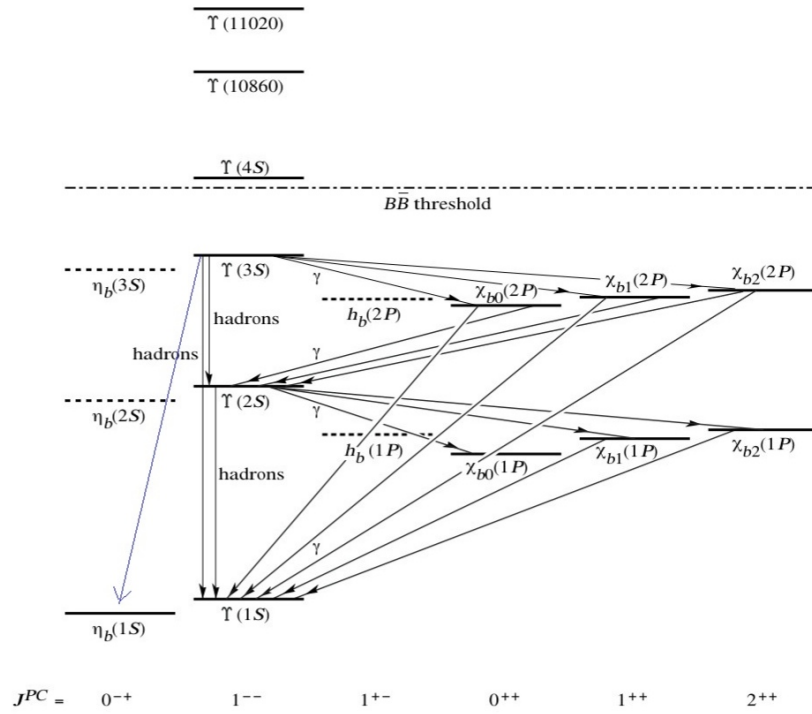


Figure 2.1: A scheme of the members of the bottomonium family. Possible feed-down decay channels are signified by arrows and the $B\bar{B}$ threshold is illustrated by the dash-dotted line.

The mean lifetime of such a particle is used in the definition of the so called *resonance width* Γ . It is defined using the relation:

$$\Gamma = \frac{\hbar}{\tau}. \quad (2.3)$$

Fig. 2.1 offers a schematic view of the bottomonium family. It also illustrates a so called *feed-down effect*, a phenomenon, where a heavier quarkonium state decays to a lighter one. While it will be elaborated on later in more detail, it may shine a light on what bottomonium states will play a larger role in this study. The Υ meson is the focus of this thesis and therefore will be the first to be mentioned. Tab. 2.2 offers a brief overview of the three lightest states of the Υ meson, which occupies the $0^-(1^{--})$ quantum state. While other, heavier Υ states also exist, they are too heavy to contribute in a significant way to the bottomonium yield at the RHIC particle collider, as they primarily decay into a $B\bar{B}$ pair. The table offers their masses and resonance widths, which are well measured, as the Υ meson is the most studied and easiest to measure state of the bottomonium family. This is given by its quantum state, which is the most stable one for quarkonia.

Other states, which attribute significantly to the Υ yield are the χ_{b0} ($0^+(0^{++})$), χ_{b1} ($0^+(1^{++})$) and χ_{b2} ($0^+(2^{++})$), which are summarised in Tab. 2.3, Tab. 2.4 and Tab. 2.5 respectively. The remaining states will not be introduced, as they do not play a significant role in the analysis from either the experimental or theoretical standpoint and are thus deemed outside the scope of this thesis.

Particle	m [MeV/c ²]	Γ [keV]
$\Upsilon(1S)$	9460.30 ± 0.26	54.02 ± 1.25
$\Upsilon(2S)$	10023.26 ± 0.31	31.98 ± 2.63
$\Upsilon(3S)$	10355.2 ± 0.5	20.32 ± 1.85

Table 2.2: A summary table of the mass m and resonance width Γ of the first three $\Upsilon(nS)$ mesons. Values taken from [6].

With the states introduced, the decays of quarkonia can now be properly discussed. The Υ meson exhibits a very strong tendency to decay into gluons. For reference, the appropriate branching ratios (BRs) given by the PDG are $\text{BR}(\Upsilon(1S) \rightarrow ggg) = (81.7 \pm 0.7)\%$ and $\text{BR}(\Upsilon(1S) \rightarrow \gamma gg) = (2.2 \pm 0.6)\%$ [6]. While these decay modes are suppressed by the so called OZI rule, they nevertheless dominate. The OZI rule suppresses hadronic decays compared to the leptonic, which occur via the electromagnetic interaction. Since the electromagnetic interaction is about two orders of magnitude weaker than the strong interaction (see Chapter 1 for coupling constants), the lifetime of Υ (and for this matter even J/Ψ , its charmonium equivalent) is longer than expected. The practical issue with these decay channels is the fact, that gluons cannot be measured on their own and they fragment into hadrons in a process called hadronisation. These hadrons interact strongly in the medium and therefore their precise measurement would be very complicated. Therefore, other, more convenient methods of detecting quarkonia have to be used. There is a notable contribution of leptonic decays. Leptons have the benefit of not being influenced by the strong

interaction and therefore retain a clear signature due to not interacting strongly with the medium. Three (charged) leptonic decays are possible - dielectron, dimuon and ditauon. The $\tau^-\tau^+$ channel would be inconvenient to measure due to the tau lepton's short lifetime.

Particle	m [MeV/c ²]
$\chi_{b0}(1P)$	$9859.44 \pm 0.42 \pm 0.31$
$\chi_{b0}(2P)$	$10232.5 \pm 0.4 \pm 0.5$

Table 2.3: A summary table of the mass m of the first two $\chi_{b0}(nP)$ mesons. Values taken from [6].

This leaves the electron-positron and muon-antimuon decays, which provide a straight and practical way to obtain a clear signal of the quarkonium resonance. The downside is the amount of statistics needed due to Υ meson's branching ratios into those channels of about 2%. Modern detectors often are constructed with subsystems intended for muon detection (the Resistive Plate Chambers at LHC's CMS or the Muon Telescope Detector at RHIC's STAR), which makes the Υ signal extraction convenient. Nevertheless, this analysis has a goal of reconstructing the Υ meson's three lightest states in the dielectron (or rather electron-positron) decay channel. The branching ratios for these are:

- $\text{BR}(\Upsilon(1S) \rightarrow e^-e^+) = (2.38 \pm 0.11)\%$,
- $\text{BR}(\Upsilon(2S) \rightarrow e^-e^+) = (1.91 \pm 0.16)\%$,
- $\text{BR}(\Upsilon(3S) \rightarrow e^-e^+) = (2.18 \pm 0.20)\%$.

Particle	m [MeV/c ²]
$\chi_{b1}(1P)$	$9892.78 \pm 0.26 \pm 0.31$
$\chi_{b1}(2P)$	$10255.46 \pm 0.22 \pm 0.50$
$\chi_{b1}(3P)$	$10513.42 \pm 0.41 \pm 0.53$

Table 2.4: A summary table of the mass m of the first three $\chi_{b1}(nP)$ mesons. Values taken from [6].

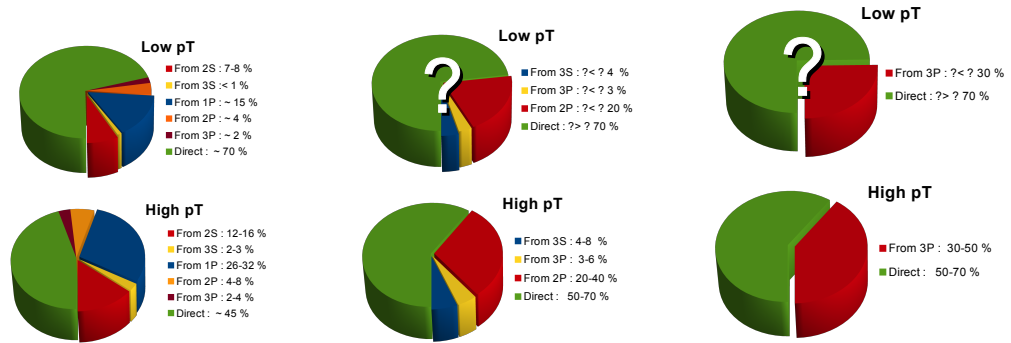


Figure 2.2: An estimate of $\Upsilon(1S)$, $\Upsilon(2S)$ and $\Upsilon(3S)$ (left, middle and right respectively) sources at low ($\lesssim 20$ GeV/c) and high ($\gtrsim 20$ GeV/c) Υ p_T . Values assume negligible rapidity dependence. Taken from [12].

The matter of feed-down decays also needs to be brought to attention. As mentioned before, this phenomenon refers to the decay of a quarkonium state into a lighter one with a simultaneous emission of other particles. Some examples include $\Upsilon(2S) \rightarrow \Upsilon(1S)\pi^+\pi^-$ with a branching ratio of $(17.82 \pm 0.26)\%$ or $\chi_{b0}(1P) \rightarrow \Upsilon(1S)\gamma$ with a BR of $(1.94 \pm 0.27)\%$ [6]. This modifies the production rates of the bottomonia, since they are produced not only directly (more on that later), but also via this mechanism. A rough estimate of $\Upsilon(1S)$, $\Upsilon(2S)$ and $\Upsilon(3S)$ sources based on the LHC experiments' measurements can be seen on Fig. 2.2. It shows, that with increasing Υ meson p_T the fraction of directly produced particles decrease, as the feed-down contribution increases.

Particle	m [MeV/c ²]
$\chi_{b2}(1P)$	$9912.21 \pm 0.26 \pm 0.31$
$\chi_{b2}(2P)$	$10268.65 \pm 0.22 \pm 0.50$
$\chi_{b2}(3P)$	$10524.02 \pm 0.57 \pm 0.53$

Table 2.5: A summary table of the mass m of the first three $\chi_{b2}(nP)$ mesons. Values taken from [6].

2.3 Production

The precise nature of quarkonium production is not yet exactly understood. It is known, that it consists of two distinct parts: the creation of the heavy quark and antiquark and the formation of the $Q\bar{Q}$ bound state (here the $Q\bar{Q}$ signifies the heavy quark and its corresponding antiquark). The quark production occurs in the early stages of the collision and due to the high mass of the quarks (see Tab. 1.1, $m_b = 4180_{-40}^{+30}$ MeV/ c^2 [6]), it has to be in a hard process (one that can be described using perturbative quantum chromodynamics - pQCD). The second part is the formation of the bound state - here the energies are lower and thus the pQCD can be used no more. This is a soft process which is non-perturbative in nature and models attempt to describe it.

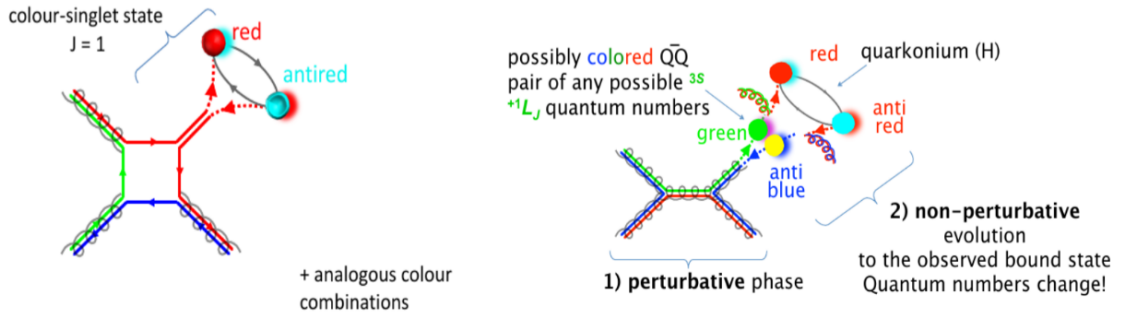


Figure 2.3: An illustration of the two steps involved in quarkonium production - 1) the creation of a heavy quark-antiquark pair, 2) the formation of a bound state. Taken from [13].

This can occur in two possible ways, depending on the $Q\bar{Q}$ quantum state. The bound state can be produced as a colour singlet (CS), which is a colourless (or colour-neutral) state, whose quantum numbers are the same as those of the final quarkonium (in the case of the Υ meson therefore 3S_1). The other option is a colour octet (CO) state, which has any possible combination of quantum numbers $^{+1}L_J$ and colour. This state then has to "lose" its colour in order to exist as a colour neutral state. An illustration of the two production channels can be seen on Fig. 2.3.

Before introducing the prevalent models of quarkonium formation in more detail, there are a few more things to be mentioned regarding the $Q\bar{Q}$ production. In hard scattering, the pQCD process where the production occurs, quarkonia are predominantly created via gluon fusion $gg \rightarrow Q\bar{Q}g$ at RHIC energies and higher. Other significant contributions come from quark-antiquark interaction ($q\bar{q} \rightarrow Q\bar{Q}g$) or quark-gluon interaction ($qg \rightarrow Q\bar{Q}g$).

There is also the matter of the quarkonium mass. Naturally, one would assume that the lower bound of the quarkonium mass would be the sum of its constituents ($m_{Q\bar{Q}} \leq 2m_Q$). Taking into the fact, that the binding energy of a formed bound state can never be zero, the relation will never be equal. That is indeed the case, as the lightest bottomonium $\eta_b(1S)$ ($m_{\eta_b(1S)} = 9398.7 \pm 2.0$ GeV/ c^2 [6]) is heavier than

a sum of two b quarks ($2m_b \simeq 8360 \text{ MeV}/c^2$ [6]). Is there any such relation for a heaviest possible bottomonium?

This chapter has already mentioned the $B\bar{B}$ threshold, when talking about the possible bottomonium states (see Fig. 2.1). This refers to a charged B^\pm meson, which is the lightest particle containing a b quark. The valence quark composition of a B^+ is $u\bar{b}$, whereas the B^- is its antiparticle. It's mass is given as $m_{B^\pm} = 5279.34 \pm 0.12 \text{ MeV}/c^2$ [6]. The aforementioned $B\bar{B}$ threshold is a mass equal to two B^\pm mesons. If a quarkonium is heavier than this invariant mass threshold, it can decay into B^+B^- (generally $B\bar{B}$ is used, as it can refer to other B mesons - charged, neutral, strange or charmed). This is more energetically beneficial, and thus is the favoured decay channel and on top of that, it is not affected by the OZI rule.

This can be nicely illustrated on the case of $\Upsilon(4S)$. This state was omitted in Tab. 2.2, because it was not studied in this study. It can nevertheless be seen in Fig. 2.1, which conveniently includes the $B\bar{B}$ threshold. The $\Upsilon(4S)$ with its mass $m_{\Upsilon(4S)} = 10579.4 \pm 1.2 \text{ MeV}/c^2$ [6], compared to an approximation of $m_{B\bar{B}} = 10560 \text{ MeV}/c^2$. This should mean, that the $\Upsilon(4S) \rightarrow B\bar{B}$ is possible. The data shows, that indeed, the $\Upsilon(4S)$ decays into $B\bar{B}$ in more than 96% cases with a confidence level of 95% [6].

Getting back to the quarkonium production models, in the following subsections this thesis will present a brief overview of the most commonly used ones. These include the *Colour Singlet Model*, *Colour Octet Model*, *Colour Evaporation Model* and the *Colour Glass Condensate + non-relativistic QCD*.

2.3.1 Colour Singlet Model

The Colour Singlet Model (CSM) [14–16] is based on the assumption, that the quark-antiquark pair $Q\bar{Q}$ is produced already in a colour neutral state and thus the evolution of the colour state up until hadronisation can be simplified by not requiring additional gluon emissions. It also assumes a non-relativistic description of the quarkonium. This model provides a way to calculate the quarkonium production cross section $d\sigma_{Q\bar{Q}+X}$ via the equation:

$$d\sigma_{Q\bar{Q}+X} = \sum_{a,b} \int f_{a/A}(x_a, \mu_F) f_{b/B}(x_b, \mu_F) d\sigma_{ab \rightarrow (Q\bar{Q})+X}(s, \mu_F, \mu_R, \alpha_s) |\psi(0)|^2, \quad (2.4)$$

which includes the *parton distribution functions* (PDFs) $f_{a/A}, f_{b/B}$, the scales for factorisation μ_F and renormalisation μ_R , as well as the wavefunction $\psi(0)$, which can be obtained from data or theoretical calculations.

The CSM works at describing a large fraction of the quarkonium cross section, when compared to data from the experiments at the LHC and RHIC [12]. A large fraction

of the produced quarkonia is assumed to be in the colour singlet channel (especially for high- p_T quarkonia). However, there are other components, the next-to-leading-order (NLO) and next-to-next-to-leading-order (NNLO) expansions, needed to describe the whole production.

2.3.2 Colour Octet Model

The Colour Octet Model (COM) [17] set a goal to take into account all of the possible quark-antiquark pair states before the bound state hadronisation. Its basis is non-relativistic QCD (NRQCD) description [18, 19], as (same with the CSM), the quarks are considered non-relativistic due to their large mass. It also utilises the expansion in the powers of the velocity v for the non-perturbative part, where the leading contribution corresponds to the colourless CO state. The cross section can similarly be expressed as:

$$d\sigma_{Q\bar{Q}+X} = \sum_{a,b,n} \int f_{a/A}(x_a, \mu_F) f_{b/B}(x_b, \mu_F) d\sigma_{ab \rightarrow (Q\bar{Q})_n+X}(s, \mu_F, \mu_R, \mu_\lambda, \alpha_s) \langle O_{Q\bar{Q}}^n \rangle, \quad (2.5)$$

where the $\langle O_{Q\bar{Q}}^n \rangle$ corresponds to a long distance matrix element (LDME), which is a key ingredient of quarkonium production models used in Monte Carlo event generators. These are used to describe the bound state formation probability and can either be calculated from theory or extracted from experimental data. It also utilises another scale μ_λ in order to correct for divergences. This model works only for high- p_T quarkonia (due to requiring $p_T/m > 1$ for sufficiently hard process to be treated perturbatively), but is consistent with experimental data [20].

2.3.3 Colour Evaporation Model

The Colour Evaporation Model (CEM) [21–23] employs a so called quark-hadron duality principle. This results in a direct connection between the quarkonium and the created $Q\bar{Q}$ pair. The quark-antiquark pair can be formed in any colour state and has to neutralise its colour via a soft gluon radiation in order to bind into a hadronised quarkonium. The cross section is given by:

$$d\sigma_{Q\bar{Q}} = F_{Q\bar{Q}} \int_{2m_Q}^{2m_H} \frac{d\sigma_{Q\bar{Q}}}{dm_{Q\bar{Q}}} dm_{Q\bar{Q}}, \quad (2.6)$$

where the m_H corresponds to the lightest open flavour meson corresponding to the quark flavour. The factor $F_{Q\bar{Q}}$ is simply a number, which represents a probability of a hadronisation for a particular state and is calculated from experimental values.

The original CEM works well at reproducing the trends in the experimentally observed cross sections [24, 25]. However, it does not describe the quantum state of the

particles and neither the polarisation of the formed states. Therefore an extension to this model, the Improved Colour Evaporation Model (ICEM) has been introduced [26], which provides predictions for polarisation.

2.3.4 Colour Glass Condensate + non-relativistic QCD

The Colour Glass Condensate (CGC) [27] model has been combined with the NRQCD treatment employed in the COM in order to extend the predictions into the low- p_T region. The CGC is a type of matter, where the gluon density is high enough, that they can be described by a wavefunction of a high energy hadron [28]. The perturbative part of Eq. 2.6 in the COM is replaced by a CGC-based calculation. It also employs the dense/dilute proton picture, which works best at forward rapidities. The dilute proton contains high- x gluons, whereas the dense proton includes low- x gluons and is described by a classical field. The x here is the Bjorken scaling variable, which refers to the fraction of momentum carried by an inclusively observed particle [29, 30]. This approach has yielded results consistent with charmonium production at the major accelerator experiments [31].

2.4 Quarkonium suppression

The quark-gluon plasma (QGP) is an extreme state of matter, where the quarks and gluons, which under normal conditions are bound in colour neutral hadrons, can exist in a so called *asymptotic freedom*. This is possible at energy densities and temperatures, which are achievable in ultrarelativistic heavy ion collisions at the LHC and RHIC particle colliders [32]. Above the Hagedorn temperature $T_H \sim 150$ MeV the quarks and gluons are no longer bound and become deconfined.

The quarkonia are a convenient quark gluon plasma probe, as they are formed early in the collision evolution. The heavy quark-antiquark pair is formed before the creation of QGP and therefore they can provide information about the early stages of the medium, as they interact via the strong interaction. One crucial component involved in this studies is the Debye-like screening of the di-quark potential, which causes the sequential suppression of the quarkonium states [33].

Such suppression can be used to determine the approximate temperature of the medium the quarkonia traverse. The lighter states possess more binding energy and therefore require higher temperatures to dissociate in QGP. Thus, observing a decrease in the yield of a particular state may be an indication that the state is suppressed in the medium. Nevertheless, the suppression is necessarily not an indication of a specific state being dissociated. If a heavier state, which contributes significantly toward the yield of a lighter state is suppressed, it also decreases the yield of the lighter state.

The colour screening is not the only phenomenon involved in modifying the quarkonium yield. In heavy ion collisions, the cold nuclear matter (CNM) effects also affect

quarkonia. These are caused by the quarkonium interacting with a remnant of the nucleus, which was not involved in the collision. These include:

- **Nuclear absorption** [34] - a phenomenon, where the quarkonium interacts with a nucleon left after the collision causing it to lose energy;
- **Comover interaction** [35, 36] - interaction of a quark from the quark-antiquark pair with another parton flying in close proximity;
- **Parton Distribution Function Shadowing** [37] - changes to the quarkonium yield due to the distribution of quarks and gluons in the nucleus.

2.5 Multiplicity dependence of quarkonium production

The link between the yield of quarkonia and the charged particle event multiplicity in proton-proton collisions is a widely explored part of the quarkonium research. This connection is a key component in understanding the quarkonium formation. Multiple phenomena may play a role in quarkonium production, among which lay multi-parton interactions, colour glass condensate or string percolation.

Multi-parton interactions (MPIs) is a phenomenon, where more than one binary parton-parton interaction occurs in a single proton-proton collision [38]. Protons are complex composite objects comprised of three valence quarks (two u quarks and one d quark), as well a number of sea quarks and gluons. The composition of a proton is a subject of extensive studies [39]. Multi-parton interactions are the cause of large number of particles produced in proton-proton collisions and contributes to quarkonium production [40]. They may serve as a measure of event activity and momentum transfer.

The CGC formalism has been introduced in a previous section. There are possible links, which connect the CGC description of relativistic proton-proton collisions to the production of quarkonia. Multiplicity dependence dependence of two gluon and three gluon fusion production channels are examined and compared to the results achieved at the RHIC and LHC [41, 42]. These studies may explain a link between quarkonium production and parton saturation.

Another phenomenological model used to describe conditions in relativistic particle collisions is the string percolation model [43]. The model utilises strings of non-abelian colour field to describe the collective behaviour exhibited in $A - A$ and possibly even $p - p$ collisions. This model is also involved in the connection between J/Ψ production and the event multiplicity.

To study the connection between the production of quarkonia and event activity, the normalised yield of a quarkonium in dependence on self-normalised charged particle

event multiplicity is used. The experimental observable $N_{\Upsilon}/\langle N_{\Upsilon}\rangle$, the normalised Upsilon meson yield, is defined as:

$$N_{\Upsilon}/\langle N_{\Upsilon}\rangle = (N_{\text{MB}}/N_{\text{MB}}^{\text{bin}})(N_{\Upsilon}^{\text{bin}}/N_{\Upsilon}), \quad (2.7)$$

where:

- $N_{\text{ch}}/\langle N_{\text{ch}}\rangle$ is the self-normalised particle multiplicity,
- N_{Υ} is the total number of events containing Upsilon meson,
- $N_{\Upsilon}^{\text{bin}}$ is the number of Upsilon events in the corresponding multiplicity bin,
- N_{MB} is the total number of minimum bias (MB) events,
- $N_{\text{MB}}^{\text{bin}}$ is the number of MB events in the corresponding $N_{\text{ch}}/\langle N_{\text{ch}}\rangle$ bin.

Chapter 3

Recent results of quarkonia measurements

Currently, the major experiments contributing towards quarkonium production research utilise primarily the LHC collider (the ALICE, ATLAS, CMS and LHCb experiments), the RHIC collider (at the moment only the STAR experiment with previous measurements conducted by the now defunct PHENIX experiment) and the SuperKEKB collider (BELLE II experiment). This chapter presents a review of the most notable recent results published by the experiments located at the RHIC and LHC accelerators.

Two areas of quarkonium studies are discussed in this chapter: the measurement of transverse momentum and rapidity spectra, and the dependence of quarkonium yield on the charged particle multiplicity produced in the event. These measurements serve mainly for the study of production mechanisms, which is done by the comparison to phenomenological model predictions. Other studied areas connected with quarkonium measurements include the polarisation of quarkonium states, associated jet production, quarkonium pair production or quarkonium-hadron correlation femtoscopy.

3.1 Cross section transverse momentum and rapidity dependence

3.1.1 J/ψ meson spectra

The J/ψ transverse momentum distribution has been studied at the RHIC collider using both the STAR and PHENIX experiments. The results of these measurements are presented on Fig. 3.1. This figure shows the J/ψ cross section multiplied by the branching ratio in dependence on transverse momentum p_T , which was produced in proton-proton collisions at $\sqrt{s} = 200$ GeV. Included are multiple measurements performed by the STAR detector at mid-rapidity and a measurement performed by the PHENIX detector at forward rapidity [44]. They are compared with several model

calculations: the Colour Octet Model, Colour Glass Condensate + non-relativistic quantum chromodynamics and the next-to-leading-order non-relativistic quantum chromodynamics. The data is consistent with the CEM and NLO NRQCD model calculations in the measured transverse momentum ranges [44].

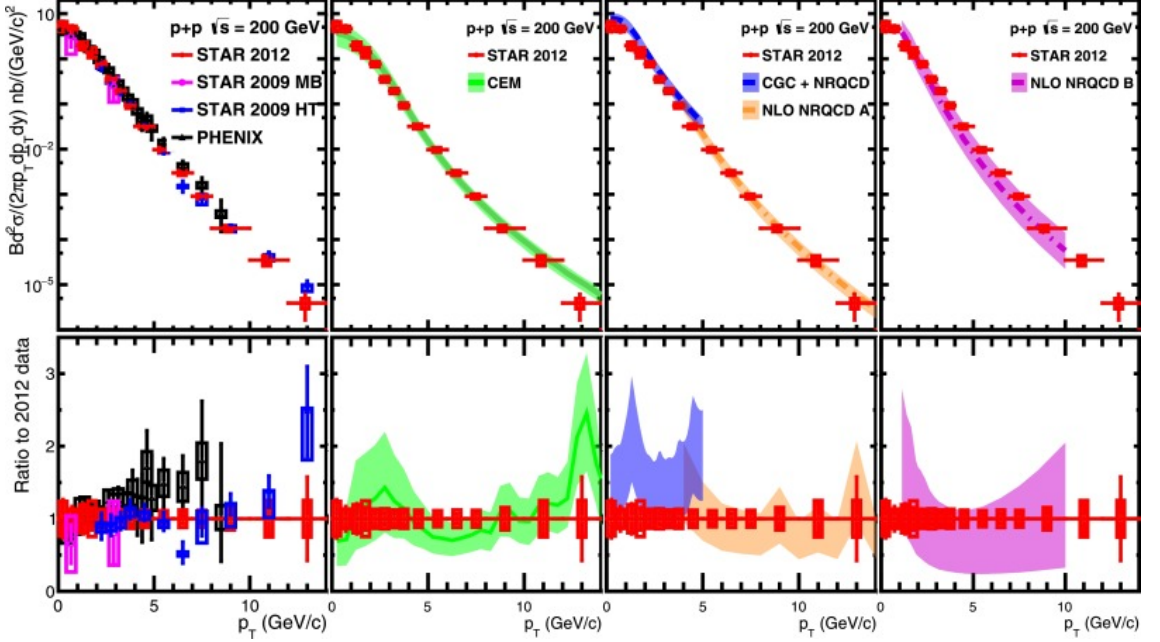


Figure 3.1: Top: The J/ψ cross section multiplied by the branching ratio as a function of transverse momentum p_T measured by STAR and PHENIX in $p + p$ collisions at $\sqrt{s} = 200$ GeV compared to model calculations. Bottom: the ratios of the presented results with regards to the STAR 2012 data. Taken from [44].

The PHENIX detector presented a unique possibility of studying the forward rapidity region at the RHIC collider, since the STAR experiment does not offer such forward coverage. The J/ψ differential cross section measurement by the PHENIX collaboration is shown on Fig. 3.2. The cross section is measured as a function of p_T . The figure offers data from both 200 GeV and 510 GeV centre-of-mass proton-proton collisions by the RHIC collider. It also includes the comparison to the leading order (LO) CGC+NRQCD and the NLO+NRQCD model calculations performed for $\sqrt{s} = 510$ GeV. The predictions are consistent with the presented results. [45]

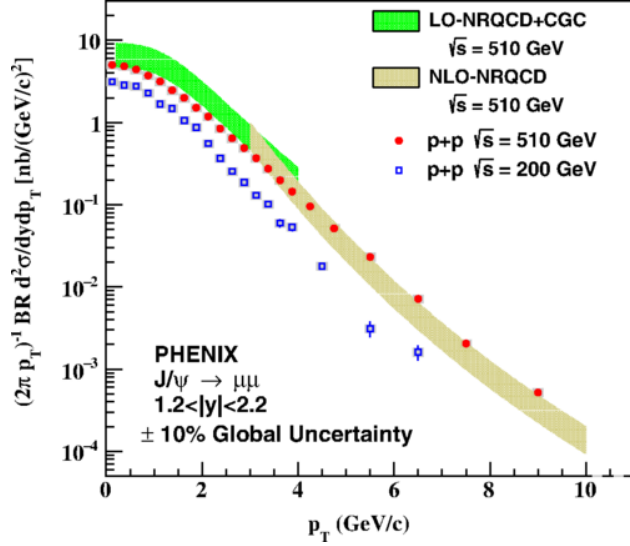


Figure 3.2: The inclusive J/ψ differential cross section as a function of transverse momentum p_T measured by PHENIX at forward rapidity $1.2 < |y| < 2.2$ in proton-proton $\sqrt{s} = 510$ GeV (closed red circles) and at $\sqrt{s} = 200$ GeV (open blue squares) with included model calculations. Taken from [45].

Similar measurements have been conducted by the STAR experiment at mid-rapidity. Fig. 3.3 presents the J/ψ full production differential cross sections with regards to the charmonium transverse momentum. The included results measured in the di-muon channel at $\sqrt{s} = 510$ GeV in a narrower rapidity range of $|y| < 0.4$ and the di-electron channel at $\sqrt{s} = 500$ GeV in a wider rapidity range $|y| < 1$. The lower rapidity reach of the di-muon measurement is due to the muon identification by STAR's Muon Telescope Detector, which has a smaller acceptance than the other detectors in STAR, such as the TPC or BEMC. This measurement combines two different leptonic decay channels and their comparison. Also included are the comparisons to the FONLL $B \rightarrow J/\psi$, FONLL+CGC+NRQCD, FONLL+NLO NRQCD and ICEM+FONLL model predictions. The FONLL is calculations are responsible for the B meson production and are necessary to include non-prompt J/ψ from B decays. The calculations match the result within the provided uncertainties [46].

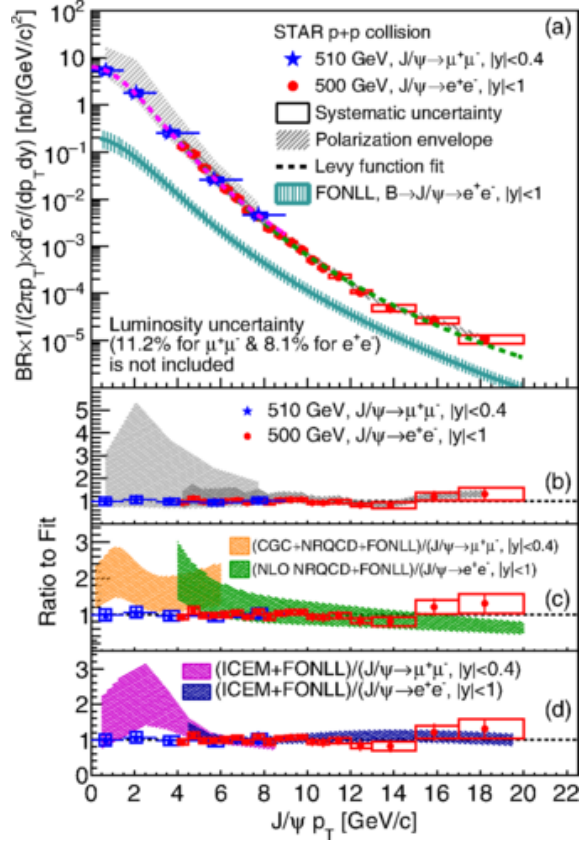


Figure 3.3: The J/ψ full production differential cross sections as a function of transverse momentum p_T measured by STAR in proton-proton collisions at $\sqrt{s} = 510$ and 500 GeV measured through the $\mu^+\mu^-$ (blue stars) and e^+e^- decay channels (red circles) compared to model calculations. Taken from [46].

The LHC also provides a thorough and precise measurements of the J/ψ meson using its multiple experiments. This subsection will review a mid-rapidity inclusive differential cross section of J/ψ measured by the ALICE detector. This measurement may be seen on Fig. 3.4. It features proton-proton collisions performed by the LHC collider at centre-of-mass energy of 5.02 TeV, which is an order of magnitude higher than the one offered by RHIC. The cross section is again studied in dependence on transverse momentum p_T . The figure also presents calculations by the NRQCD, NRQCD+CGC and NRQCD CS and CO models for prompt J/ψ with included FONLL corrections for J/ψ from b decay. The shown data correlates with the predictions offered by phenomenology [47].

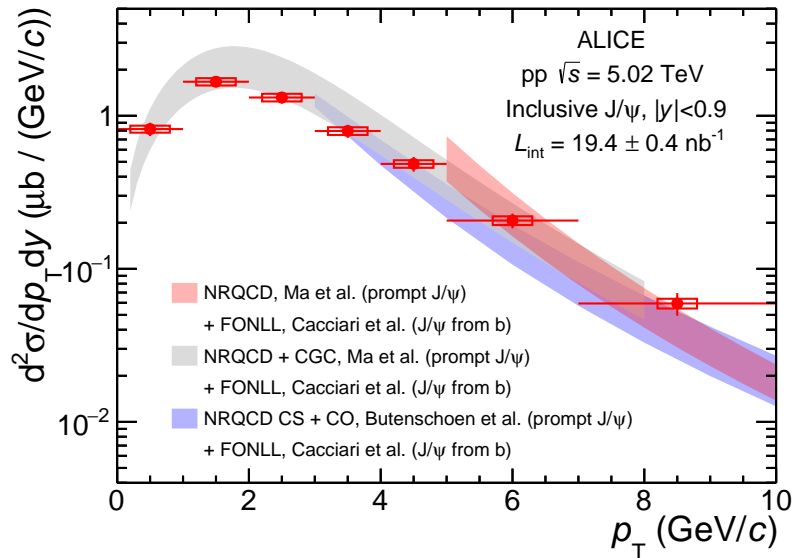


Figure 3.4: The differential inclusive J/ψ cross section with relation to transverse momentum p_T measured by the ALICE collaboration in proton-proton collisions at 5.04 TeV with comparison to model calculations. Taken from [47].

The presented J/ψ measurements present a brief overview of the many measurements performed in charmonium studies. It offers a wide range of rapidities, with central rapidity measured by the STAR and ALICE experiments and forward rapidity by the PHENIX experiment. It also features multiple decay channels, as studied by STAR, as well as a wide centre-of-mass energy (from 200 GeV up to 5.04 TeV). The measurements perform a good coverage of low- p_T charmonia. The results also presents a comparison to predictions by a variety of phenomenological models with good correspondence. Nevertheless, additional studies are needed to help distinguish between the models.

3.1.2 Υ meson spectra

The STAR collaboration is also involved in the studies of the Υ meson. One such measurement of the inclusive cross section in dependence on the quarkonium p_T is presented on Fig. 3.5. The study was performed using proton-proton collisions at centre-of-mass energy of 500 GeV. It shows the separate $\Upsilon(1S)$ spectrum, as well as the combined $\Upsilon(1S+2S+3S)$ and the $\Upsilon(2S+3S)$ spectra at low- p_T . The figure also includes the comparison to the CEM and the CGC+NRQCD theoretical models. When compared to the data, the CGC+NRQCD model overestimates the low- p_T $\Upsilon(1S)$ cross section, whereas the CEM model prediction is coherent with the data. The data also illustrates the lower cross sections of the two heavier states compared to the $\Upsilon(1S)$ state, which is to be expected [48].

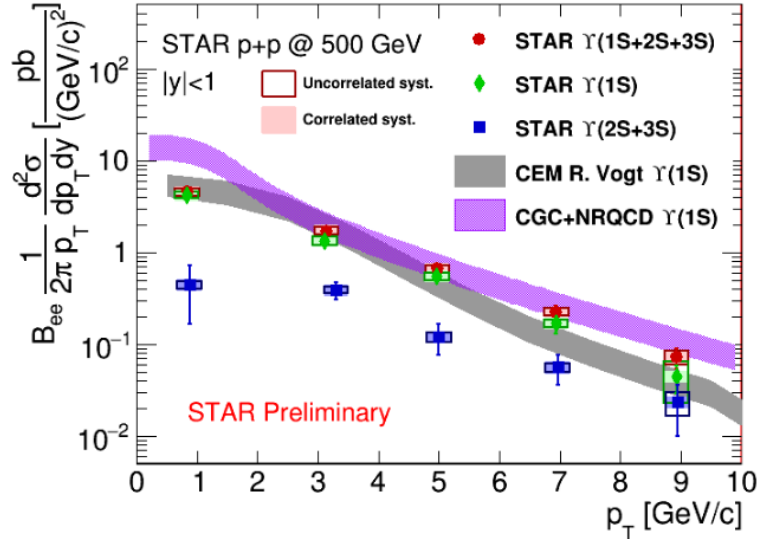


Figure 3.5: Inclusive cross section dependence on p_T of $\Upsilon(1S)$ (blue squares) and combined $\Upsilon(1S+2S+3S)$ (red dots) and $\Upsilon(2S+3S)$ (green diamonds) measured by the STAR experiment in proton-proton collisions at 500 GeV with included model predictions. Taken from [48].

The rapidity dependence of Υ meson production is also studied at the STAR detector. A study of the cross section of Υ with regards to the quarkonium rapidity may be seen on Fig. 3.6. This has been performed, as with the previous measurement, using 500 GeV proton-proton collisions at the RHIC collider. It features the individual data for $\Upsilon(1S)$, $\Upsilon(2S)$ and $\Upsilon(3S)$ states, as well as the combined $\Upsilon(2S+3S)$ and $\Upsilon(1S+2S+3S)$. Similarly, comparison to CEM and CGC+NRQCD model predictions for the $\Upsilon(1S)$ is featured. The CEM model also describes the data better, as the CGC+NRQCD model again overestimates the cross section at central rapidity. Also to note is, that both of the models predict an increasing cross section at mid-rapidity, whereas the data indicates an opposite trend [49].

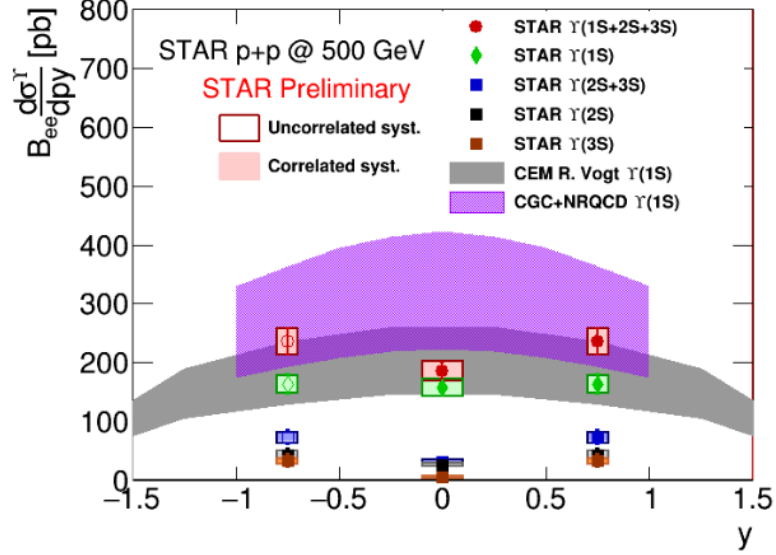


Figure 3.6: Cross section of individual $\Upsilon(1S)$ (green diamonds), $\Upsilon(2S)$ (black squares) and $\Upsilon(3S)$ (brown squares) and combined $\Upsilon(1S+2S+3S)$ (red squares), $\Upsilon(2S+3S)$ (blue squares) in dependence on rapidity y measured by STAR in 500 GeV proton-proton collisions with model calculations included. Taken from [49].

The Υ studies at the LHC benefit from the higher collision energy offered by the LHC collider, since the Υ meson production cross section increases with the energy. This may help for example in extending the p_T range of the measurements. A measurement by the CMS collaboration is shown on 3.7. This measurement offers the differential cross section of $\Upsilon(1S)$, $\Upsilon(2S)$ and $\Upsilon(3S)$ states in dependence on quarkonium transverse momentum done in 7 TeV proton-proton collisions. It features a wide transverse momentum range up to 100 GeV/c. Also shown are the previous results of the collaboration, which are consistent with the new results. The data is compared to theoretical prediction of the NRQCD calculation at NLO precision with good correspondence [50].

This subsection summarised a few of the Υ measurements done by the LHC and RHIC experiments. The STAR collaboration published results for low- p_T separate and combined Υ mesons. The data for $\Upsilon(1S)$ matches the predictions given by the CEM model. Also discussed was a measurement of the CMS detector, which offered a wide p_T range. The data was well described by the NRQCD NLO theory.

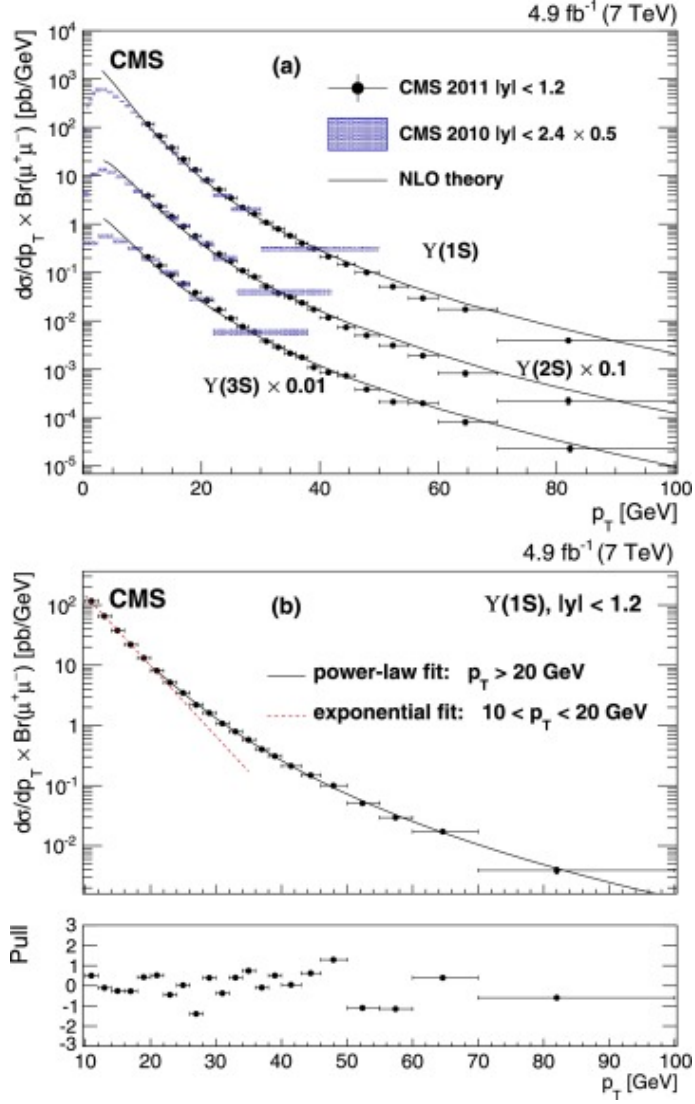


Figure 3.7: The $\Upsilon(1S)$, $\Upsilon(1S)$ and $\Upsilon(1S)$ differential cross sections in dependence on p_T multiplied by the dimuon branching fractions in $|y| < 1.2$ by the CMS collaboration on proton-proton collisions at 7 TeV. The $\Upsilon(2S)$ and $\Upsilon(3S)$ measurements are scaled by 0.1 and 0.01 respectively for display purposes. Previous CMS measurements for $|y| < 2.4$ are shown as cross-hatched areas. These results have been scaled by 0.5 to account for the smaller $|y|$ range in the latest measurement, where the scaling assumes that the rapidity distribution is flat. Comparison to NRQCD calculations at NLO precision is included. Taken from [50].

3.2 Quarkonium yield event multiplicity dependence

3.2.1 J/ψ meson multiplicity dependence

The quarkonium yield dependence on charged particle multiplicity has been studied at the RHIC collider using the STAR experiment. Fig. 3.8 presents the measurement of J/ψ multiplicity dependence in proton-proton collisions at the centre-of-mass energy of 200 GeV in mid-rapidity. The measurement is presented for several transverse momentum ranges (inclusive p_T , $p_T > 1.5$ GeV/c and $p_T > 4$ GeV/c). Also shown is the data measured by the ALICE detector for inclusive p_T . The figure further features the comparison for prediction given by Monte Carlo event generators PYTHIA8 and EPOS3.2 and the string percolation model. Both the Monte Carlo calculations appear to match the data. The percolation model also appears to quantitatively represent the trend exhibited by the data. One can observe the dependence of the measured yield on event multiplicity to be stronger than linear [51].

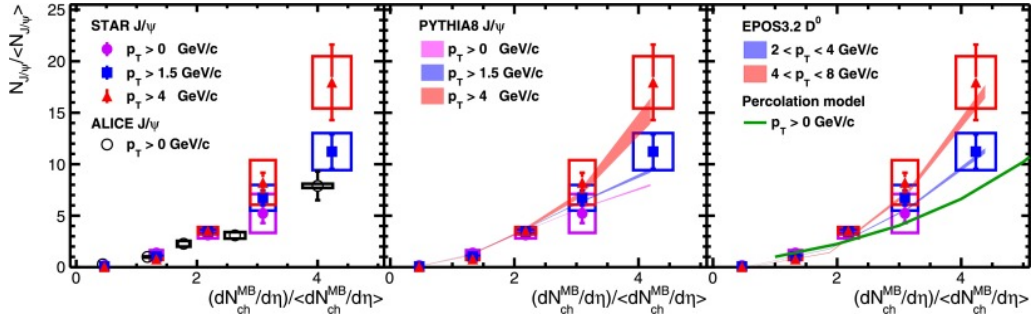


Figure 3.8: The multiplicity dependence of J/ψ meson yield in proton-proton collisions at $\sqrt{s} = 200$ GeV measured by the STAR collaboration with comparison to Monte Carlo and theory predictions. Taken from [51].

The ALICE collaboration offers results for inclusive J/ψ mesons. On Fig. 3.9 one may see the results for J/ψ yield dependence on charged particle event multiplicity measured in proton-proton collisions at 13 TeV observed in central rapidity, which is the most recent LHC result. The figure also offers the comparison to PYTHIA and EPOS Monte Carlo event generator predictions, as well as the CPP [52], 3-pomeron CGC [41], string percolation [43] and CGC [27, 31] phenomenological model calculations. Also illustrated is the linear dependence. The CPP, 3-pomeron CGC and CGC models agree with the data well, while the results given by the string percolation model and the PYTHIA and EPOS generators copy the trend while not predicting the correct magnitude. Both the data and all of the predictions again indicate the stronger than linear increase of the measured quantity [53].

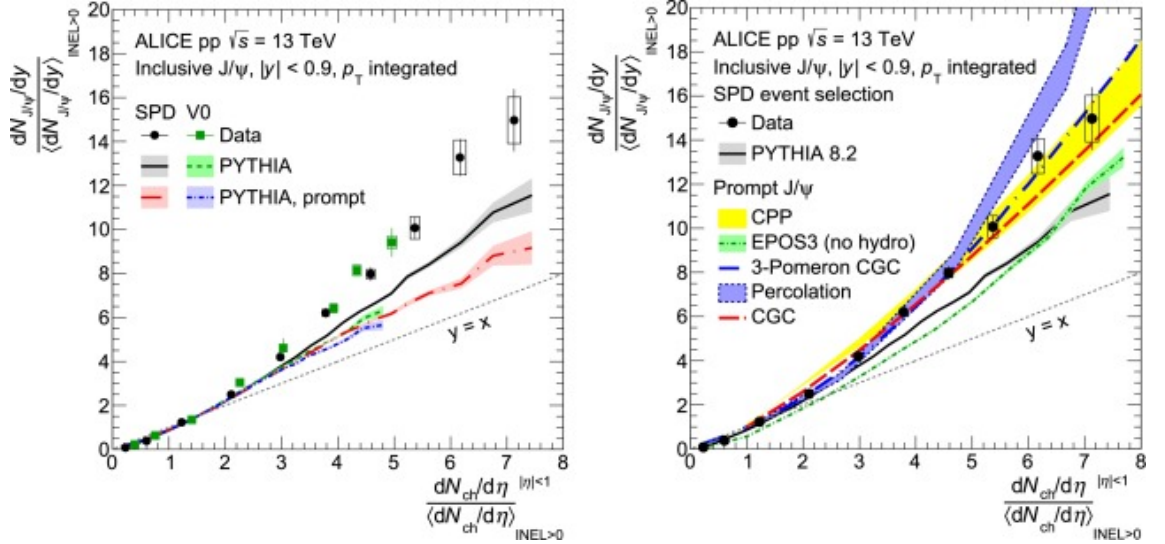


Figure 3.9: Normalized inclusive J/ψ yield as a function of charged particle event multiplicity in proton-proton collisions at $\sqrt{s} = 13$ TeV measured by the ALICE collaboration. Comparison to models and Monte Carlo generators is shown. Taken from [53].

Data from both LHC and RHIC show the same trend for the measured yield, where the normalised yield dependence on normalised event multiplicity grows stronger than linear. This may be an indication, that the quarkonia are produced in multiparton interactions. However, more data and model development is needed to confirm this connection. Nevertheless, all of the models and Monte Carlo generators predict the same trend as observed in data with varying success at matching the measured magnitudes.

3.2.2 Υ meson multiplicity dependence

Fig. 3.10 and Fig. 3.11 show the preliminary measurement of normalised $\Upsilon(1S)$ meson yield with regards to self-normalised charged particle event multiplicity in 500 GeV proton-proton collisions done by the STAR collaboration. Fig. 3.10 includes comparisons to other measurements performed at the CMS experiment for $\Upsilon(1S)$ mesons at 2.76 TeV and at STAR and ALICE experiments for J/ψ at 200 GeV and 7 TeV respectively. It also features a line indicating the linear trend. All of the measurements show a comparable trend with the yield increasing stronger than linear. The Fig. 3.11 also includes predictions of the PYTHIA Monte Carlo event generator, as well as CGC+saturation and string percolation model calculations. The data again presents a stronger than linear increase in the measured yield with regards to the event multiplicity. The model predictions and PYTHIA describe the data well with regards to the trend and magnitude [54].

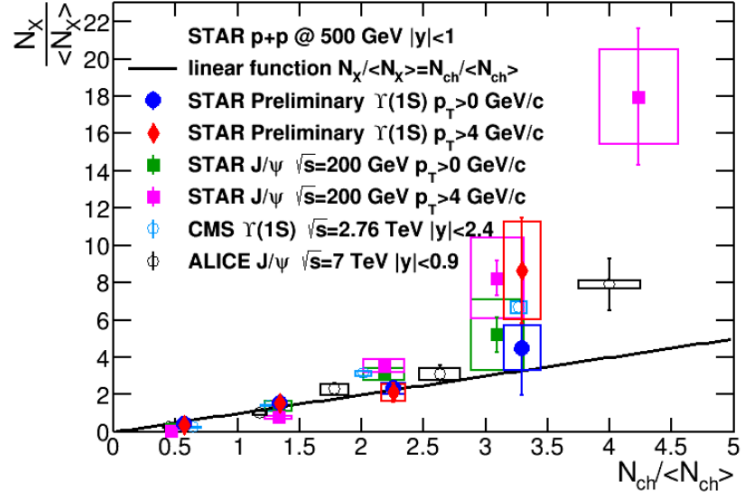


Figure 3.10: The multiplicity dependence of $\Upsilon(1S)$ yield in 500 GeV proton-proton collisions measured by the STAR detector. Also included are the data from other measurements for comparison. Taken from [54].

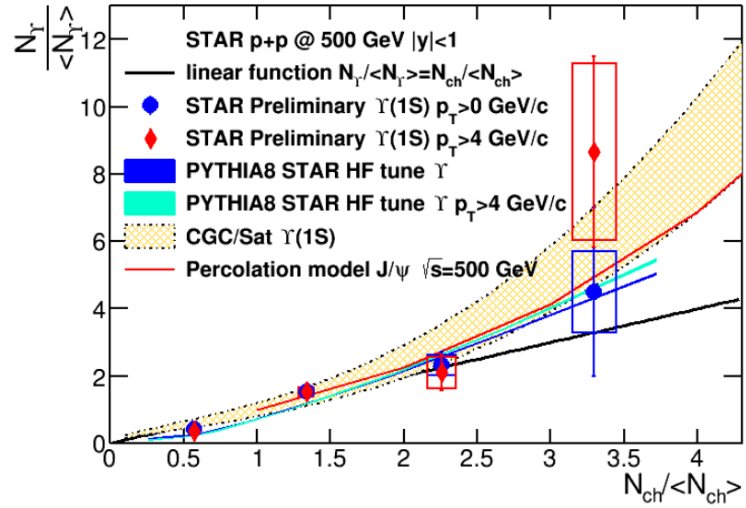


Figure 3.11: The multiplicity dependence of $\Upsilon(1S)$ yield in 500 GeV proton-proton collisions measured by the STAR detectors. The figure features the comparison to model and Monte Carlo calculations. Taken from [54].

The ALICE collaboration has done a measurement of J/ψ and Υ mesons in both central and forward rapidities, offering a unique comparison. Presented of Fig. 3.12 are the results for inclusive J/ψ at mid-rapidity and for J/ψ , $\Upsilon(1S)$ and $\Upsilon(2S)$ in forward rapidities done in proton-proton collisions at 13 TeV centre-of-mass collision energy. The figure also features an indication of the linear trend. The central rapidity results show a strong increase observed in all previously discussed measurements. The forward rapidity data seems to have a more linear increase. It is important to note the last point form the J/ψ measurement, which may indicate, that the trend may be stronger than linear [55].

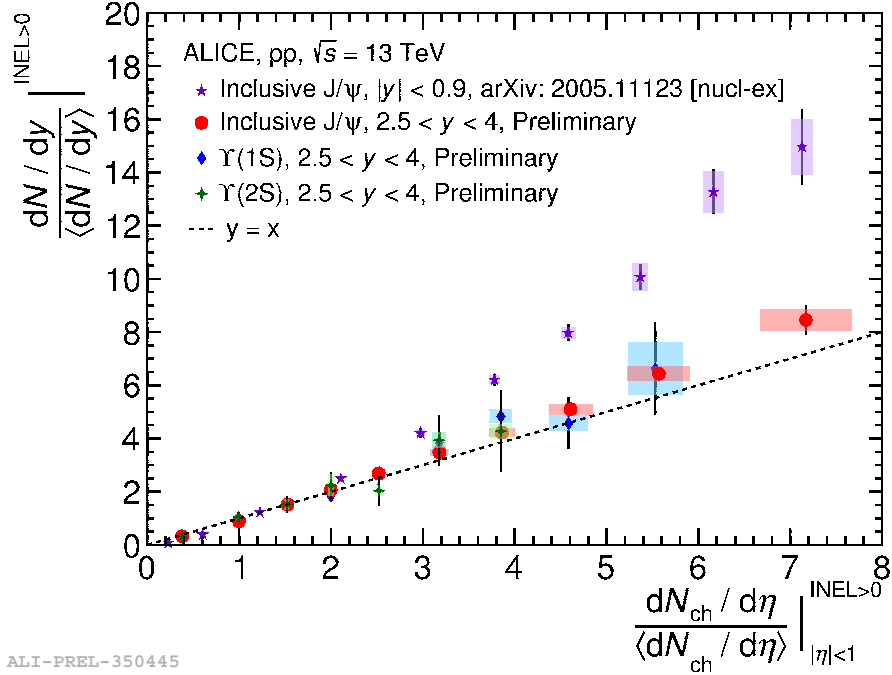


Figure 3.12: Normalized yields of J/ψ (red dots), $\Upsilon(1S)$ (blue diamonds) and $\Upsilon(2S)$ (green crosses) at forward rapidity and of J/ψ at mid-rapidity (purple stars) as a function of the normalised event multiplicity in 13 TeV proton-proton collisions measured by the ALICE collaboration. Taken from [55]

Both STAR collaboration measurement for central rapidity $\Upsilon(1S)$ exhibits the same trend observed for J/ψ (which can be also seen in the ALICE measurement), which is consistent with the hypothesis of quarkonia being produced in multi-parton interactions. A comparison with forward rapidity data is offered by the ALICE measurement. Here the trend is much weaker in comparison and more measurements are needed to definitely see, whether the trend is linear or stronger.

Chapter 4

The STAR experiment

4.1 RHIC

The Relativistic Heavy Ion Collider (RHIC) is a heavy ion collider located at the Brookhaven National Laboratory (BNL), which is situated in Upton, NY in the United States of America. It was the first heavy ion collider ever build and is currently one of the two operational, the other one being the Large Hadron Collider (LHC) in CERN, Geneva, Switzerland. The RHIC has been first put into use in 2000 and until the completion of the LHC in 2010 it offered the highest energies of any machines capable of performing heavy ion collisions. The possibility of accelerating heavy ions opens new opportunities for studying the quark gluon plasma, such as the Beam Energy Scan (BES) programme (currently finished with the second phase [56]). This allows the STAR experiment located at RHIC to probe the transition between hadronic matter and the QGP. The aim of the BES programme is to locate the critical point of nuclear matter, where a first order transition between hadron gas and the QGP phase becomes a second order transition (smooth crossover). The position of this critical point is currently not known precisely and the BES II, with its energy range from 3 to 19.5 GeV, attempts to study the QCD phase diagram.

Different collisions configurations are possible using the RHIC accelerator, thanks to the fact it is designed for heavy ion use and thus is able to accelerate various different ions. It has been utilised for the measurement of symmetric $Au-Au$, $Cu-Cu$, $U-U$ collisions and asymmetric $He-Au$, $Cu-Au$ or $d-Au$. As mentioned before, it allows for proton acceleration as well offering the possibility of studying $p-p$ or $p-Au$ events. On top of utilising two beam collisions, it also includes the opportunity for fixed-target experiments, such as the ones included in the BES II programme.

Another rarity of the RHIC collider is the ability to study spin polarised protons. Using the "Siberian Snake" magnets located at the ring, which interact with the spin of the proton, it creates beams of polarised protons, which can then be used in experimental measurements.

In the course of its more than 20 year operation, the RHIC collider has been used

as a source of high energy particle beams for 4 major experiments positioned along its circumference. The only experiment in use at the moment is the STAR detector situated at the 6 o'clock position of the RHIC ring. It was designed for the detection of a large count of hadrons in central rapidity utilising an extensive Time Projection Chamber detector inside of a solenoidal magnet. The main motivation behind this detector's design was probing the QGP. Continuing clockwise, the next major detector was the PHENIX located at the 8 o'clock position, which was used for electromagnetic particle detection in axial magnetic field. It was also the biggest of the detectors used at RHIC. Currently, an improved version of this detector, the sPHENIX [57], is being assembled at the same position as is intended to be used in the next run of the RHIC collider, starting in late 2022. The PHOBOS detector at 10 o'clock was intended for multiplicity measurements and therefore featured the widest rapidity acceptance of the used detectors. Nowadays it is not in use anymore. The last major detector was the BRAHMS positioned at 2 o'clock. The role of the BRAHMS detector was the measurement of momentum spectra. It is also defunct. Another detector also operated at the RHIC ring independently, PP2PP, which studied the proton-proton scattering spin dependence. Currently, it is being operated as a part of the STAR experimental collaboration.

The RHIC is designed as an intersecting storage ring. In comparison to the CERN's LHC, which features both beampipes in a single housing, the RHIC utilises two independent storage rings denoted *yellow* and *blue*. The RHIC is built in a hexagonal shape and features six interaction points, where the beampipes intersect and allow for the interaction of the accelerated beams travelling in opposite directions (in order to maximise the collision energy in the centre-of-mass frame). The interaction points are highlighted on Fig. 4.1 as white squares along the RHIC collider. The length of the entire accelerator is 3834 m, along which 1740 superconductive magnets made of niobium-titanium alloy used for beam containment, focusing and steering. The magnetic field generated by the dipole magnets in the RHIC collider is 3.45 T.

The RHIC accelerator itself can only operate with already accelerated particle beams due to constraints posed by its design. These beams are injected into the RHIC ring around the 6 o'clock position. A simplified illustration of the series of accelerators used for RHIC pre-acceleration is shown on Fig. 4.1. For the protons, they are generated by emitting 35 keV hydrogen anions from a polarised ion source. These particles are first accelerated in the Linear Particle Accelerator LINAC, which is shown in red. The exit energy of the beam from the LINAC is 200 MeV. Illustrated in blue is the BOOSTER synchrotron, which uses its circular design for multiple *kicks*, which accelerate the protons further up to 2 GeV. The last step before the RHIC collider is the Alternating Gradient Synchrotron (AGS), which is shown in green. Again, thanks to utilising multiple *kicks*, the beams are boosted to 23 GeV, when they are injected directly into the RHIC rings, which offer the maximum beam energy of 255 GeV, which results in a centre-of-mass collision energy of 510 GeV.

Currently, BNL uses the Electron Beam Ion Source (EBIS) to produce ions used in its experiments. This is illustrated in purple, next to the LINAC. Previously, Tandem Van de Graaff ion source was used. The ions are produced at energies of

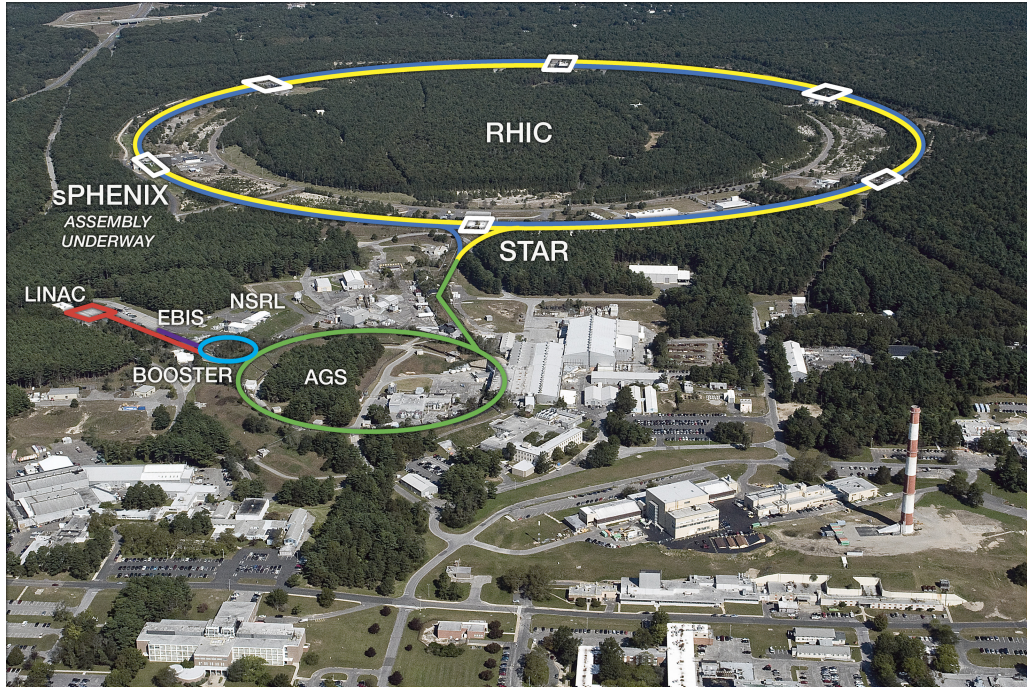


Figure 4.1: An illustration of the RHIC accelerator complex highlighted on the BNL site photograph. Taken from [59].

2 AMeV (MeV per nucleon) while being stripped of some of its electrons. In the case the gold ions, 32 out of the total of 79 electrons are removed by the EBIS. The further acceleration is the same as for protons after exiting the LINAC, so the BOOSTER and AGS synchrotrons. At the point of RHIC injection the ions possess 10 AGeV of beam energy. The RHIC can further accelerate them up to 255 AGeV.

The RHIC accelerator is scheduled to be upgraded into the Electron Ion Collider (EIC) [58], which would add another beam pipe to the RHIC ring. This beam pipe would serve for accelerating electrons and this would make it the world's only working electron-hadron collider, which would allow to probe the structure of protons and nuclei, allow the study of gluon saturation and colour glass condensate, and improve the proton spin polarisation measurement capabilities. The EIC is scheduled to begin construction in 2024 with the machine starting its operation in the early 2030's.

4.2 STAR

The Solenoidal Tracker at RHIC (STAR) detector [60, 61] is currently the only major experiment utilising the RHIC collider (until the launch of sPHENIX). The design of the STAR detector has been optimised to study the quark-gluon plasma. Therefore it primarily focuses on the measurement of hadrons using its large time projection chamber encased by a large solenoidal magnet, which gave name to the detector. The entire detector, including the magnet, weigh at 1200 tonnes and stands at 7 metres tall. The magnet itself accounts for a significant part of the detector, with

nearly 1100 tonnes of weight and 5 metre height. The magnetic field generated by the solenoid has a strength of 0.5 T, which is directed in the perpendicular direction with the accelerator beampipe. This magnetic field is used to curve the trajectories of the particles in order to measure their p_T and charge. The STAR detector is shown on Fig. 4.2.

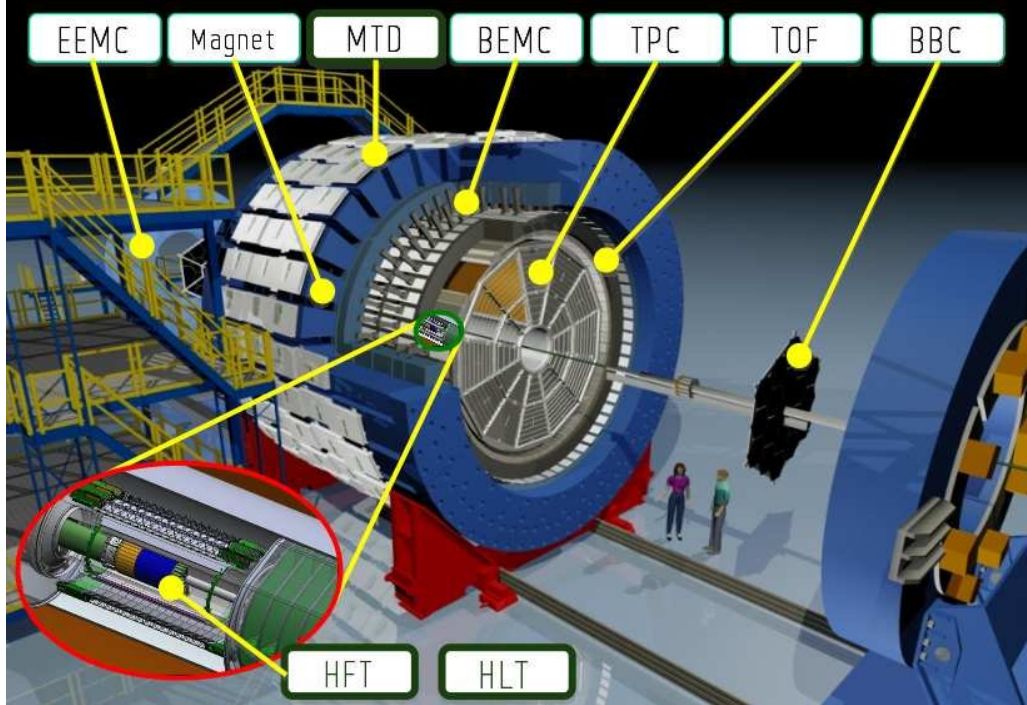


Figure 4.2: A scheme of the STAR detector. Taken from [62].

The STAR detector itself is comprised of many different subdetectors, which specialise in particular measurements. An overview of the main detectors used in this analysis will be listed here and two of the major ones, the Time Projection Chamber and the Barrel Electromagnetic Calorimeter will be introduced in more detail in the following subsections. The detectors contributing to this analysis are:

- The **Time Projection Chamber** (TPC) [63] is the central part of the STAR detector and the innermost component surrounding the beampipe. It works based on a proportional ionisation chamber principle and is a hollow cylinder filled with a gas mixture. It offers a pseudorapidity acceptance of $|\eta| \leq 1.0$ and covers the entire azimuthal range $0 < \phi < 2\pi$. It is used in this analysis for particle identification based on ionisation energy loss and the momentum measurement.
- The **Inner Time Projection Chamber** (iTPC) [64] is an upgrade to the TPC, which replaced the inner part of the TPC adding more pad rows. This improves the reconstruction efficiency of high pseudorapidity particles in the range of $1.0 < |\eta| < 1.7$. It also features an increased segmentation of the inner sectors and improved wiring. On top of the forward extension of the pseudorapidity range it offers a better ionisation energy loss resolution.

- The **Barrel Electromagnetic Calorimeter** (BEMC) [65] is a complementary detector to the TPC, offering the same pseudorapidity and azimuthal range. As an electromagnetic calorimeter it focuses on the measurement of deposited energy in the material by electromagnetically interacting particles. This allows for a better hadron-lepton/photon separation. It is most efficient at measuring high momentum particles with p_T larger than 2 GeV/c. This analysis uses the BEMC for electron identification and high- p_T electron triggering.
- The **Time of Flight** detector (TOF) [66] utilises hits in multi-gap resistive plate chambers (MRPCs) in coincidence with collision time provided by the Vertex Position Detector to determine the time of flight of the measured particle. This allows the identification of particles based on their time of flight and measured momentum. Due to its construction it offers a fast readout rate and therefore is useful in pile-up rejection. This analysis utilises it for charged particle event multiplicity. It offers a narrower range than the TPC and the BEMC of $|\eta| \leq 0.9$, while retaining the same azimuthal range. The TOF works best with low- p_T particles with p_T lower than 2 GeV/c.
- The **Vertex Position Detector** (VPD) [67] consists of two scintillators placed near the beampipe in a distance of 5.7 metres on both sides of the centre of the detector. It serves for charged particle and photon detection and is used to reconstruct the position of the main interaction vertex. Proton-proton collisions utilise this detector for triggering as well. Since it is a forward detector close to the beampipe, the pseudorapidity range offered is $4.24 \leq |\eta| \leq 5.1$.
- The **Beam Beam Counter** (BBC) [68] is a set of scintillator rings installed around the RHIC beamline outside of the STAR detector magnet. It is composed of two parts on the opposite sides of the STAR detector (BBC EAST and BBC WEST), each made up of 18 tiles. They cover a forward pseudorapidity range of $3.4 < \eta < 5.0$. It is utilised in a BBC trigger, which is a part of the trigger used in this analysis. This trigger requires a coincident signal in at least one tile on both the east and west sides.

4.2.1 Time Projection Chamber

The Time Projection Chamber [63] of the STAR detector plays a major role in the measurement of the high energy collisions in the RHIC. It is responsible for detecting the tracks of particles and the subsequent determination of their momentum and the ionisation energy loss, which serves for particle identification purposes. Therefore a large coverage is required in order to capture as many charged particle tracks as possible. The TPC offers a full azimuthal acceptance of $0 < \phi < 2\pi$ and a wide pseudorapidity window of $|\eta| \leq 1.8$. However, the particles detected in the more forward parts of the detector usually are not reconstructed with a high efficiency and quality, which would result in improper track measurement and identification, therefore a more narrow range of $|\eta| \leq 1.0$ is typically used in analyses, including this one. The iTPC [64] upgrade improved the efficiency of track reconstruction in the

more forward region of $1.0 < |\eta| < 1.7$, by adding more pad rows and thus increasing the number of possible hits in the TPC in this range.

The particle identification provided by the TPC based on the ionisation loss dE/dx serves reliably for low momentum particles with $0.1 < p < 1$ GeV/ c , whereas the momentum measurements can be done with a good resolution for particles with $0.1 < p < 30$ GeV/ c . However, particles with transverse momentum lower than 0.2 GeV/ c are usually excluded in data analysis, as they can barely reach the TPC due to their trajectory curvature caused by the solenoidal magnet and therefore are for the most part not reconstructed to a sufficient degree. This is the case for this work as well. Further discussion on the particle identification and the constraints placed on the track properties is in Chapter 6.

From a constructional standpoint, the TPC is a large hollow cylinder with an outer radius of 2 metres and an inner radius of 0.5 metres. The length of the chamber is 4.2 metres along the beamline. The chamber is filled with a P10 gas mixture (comprised of 9:1 volume ratio of argon and methane gases), which serves as an ionisation medium. The endcaps of the detector are comprised of 24 Multi-Wire Proportional Chambers (MWPCs), 12 inner and 12 outer, on each side, which track the trails caused by gaseous ionisation caused by the particles entering the detector. It also utilises a central membrane to create a voltage of 28 kV, which causes the electrons created during the gas ionisation to drift towards the endcaps with an average drift velocity of 5.45 cm/ μ s. The MWPCs detect such electrons and use them to reconstruct the trajectory of the original particle in the transverse xy plane, whereas the longitudinal coordinate z (the beam direction) is reconstructed via the drift time. A schematic view of the TPC detector is shown on Fig. 4.3.

4.2.2 Barrel Electromagnetic Calorimeter

The Barrel Electromagnetic Calorimeter [65] serves for electron and photon detection and identification by measuring their energy. The particles are detected via electromagnetic cascades, which they produce while travelling the detector material. It is comprised of alternating layers of lead, which serves for the electromagnetic interaction and cascade production, and scintillator, which records the cascades created in the lead strips. This design is commonly referred to as a Shashlik calorimeter.

Physically, the BEMC is built of 4800 independent towers, which are grouped into 120 modules, each covering 0.1 radian in azimuthal angle ϕ and and 1 unit of pseudorapidity η at their base. The detector features the same effective acceptances as the TPC detector. The BEMC, as can be seen on a schematic view of the STAR detector in Fig. 4.2, is placed on on the outer side of the TOF detector and inside the solenoidal magnet. Another schematic can be seen on Fig. 4.4, which represents the BEMC as either a *barrel*, or *barrel EMC*.

Each of the towers is constructed from 20 layers of lead and 21 layers of a scintillator. The point behind using lead is increasing the rate of the interactions of electromagnetically interacting particles traversing the material. This is due to the

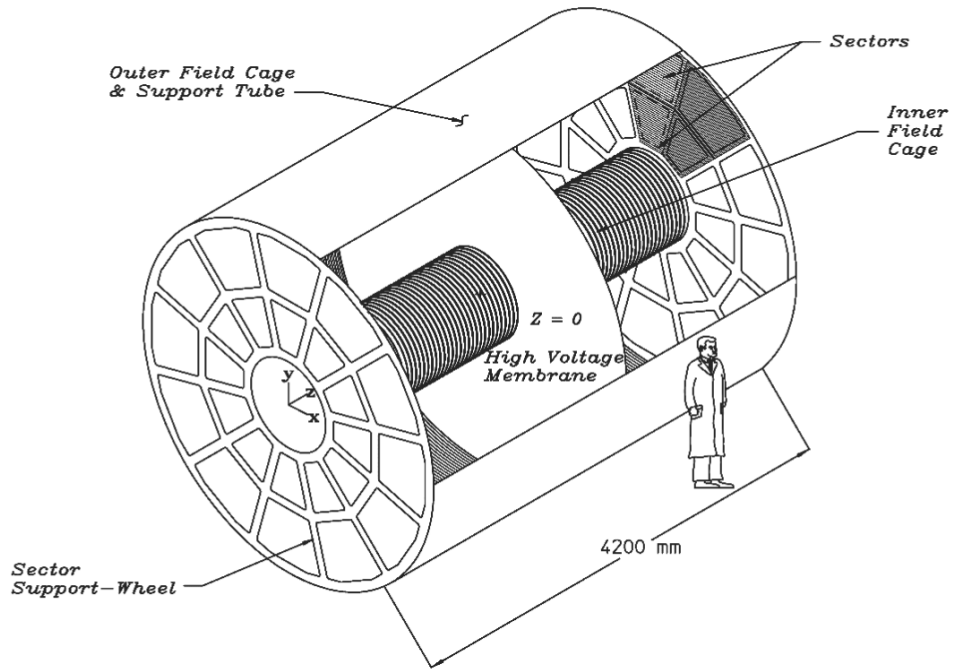


Figure 4.3: A schematic view of the TPC detector used in the STAR experiment. Taken from [63].

high atomic number of the lead nucleus, as the radiation length of a material decreases with increasing number of nucleons. The plastic scintillator is used to detect the produced electromagnetic cascade by absorbing it and re-emitting the energy in the form of light. These photons are then collected using optical fibres and measured using photomultiplier tubes placed outside of the STAR detector. A schematic of the BEMC tower is shown on Fig. 4.5.

The BEMC is especially useful in detecting high energy electrons, as they can not be easily identified in the TPC. This is due to the fact, that electrons are expected to deposit the vast majority of their energy in the BEMC due to the energy loss of electrons in lead. Additionally, the electron energy deposit is expected to be primarily in a single tower with a slight leakage in the surrounding towers. The importance of the BEMC in electron identification and the information used for their selection are discussed in Chapter 6.

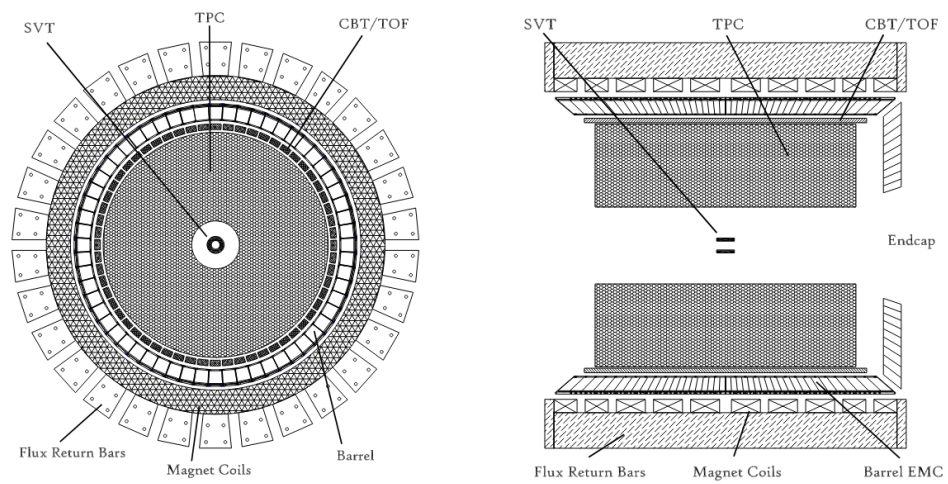


Figure 4.4: A schematic showing two cross sections of the STAR detector. Taken from [65].

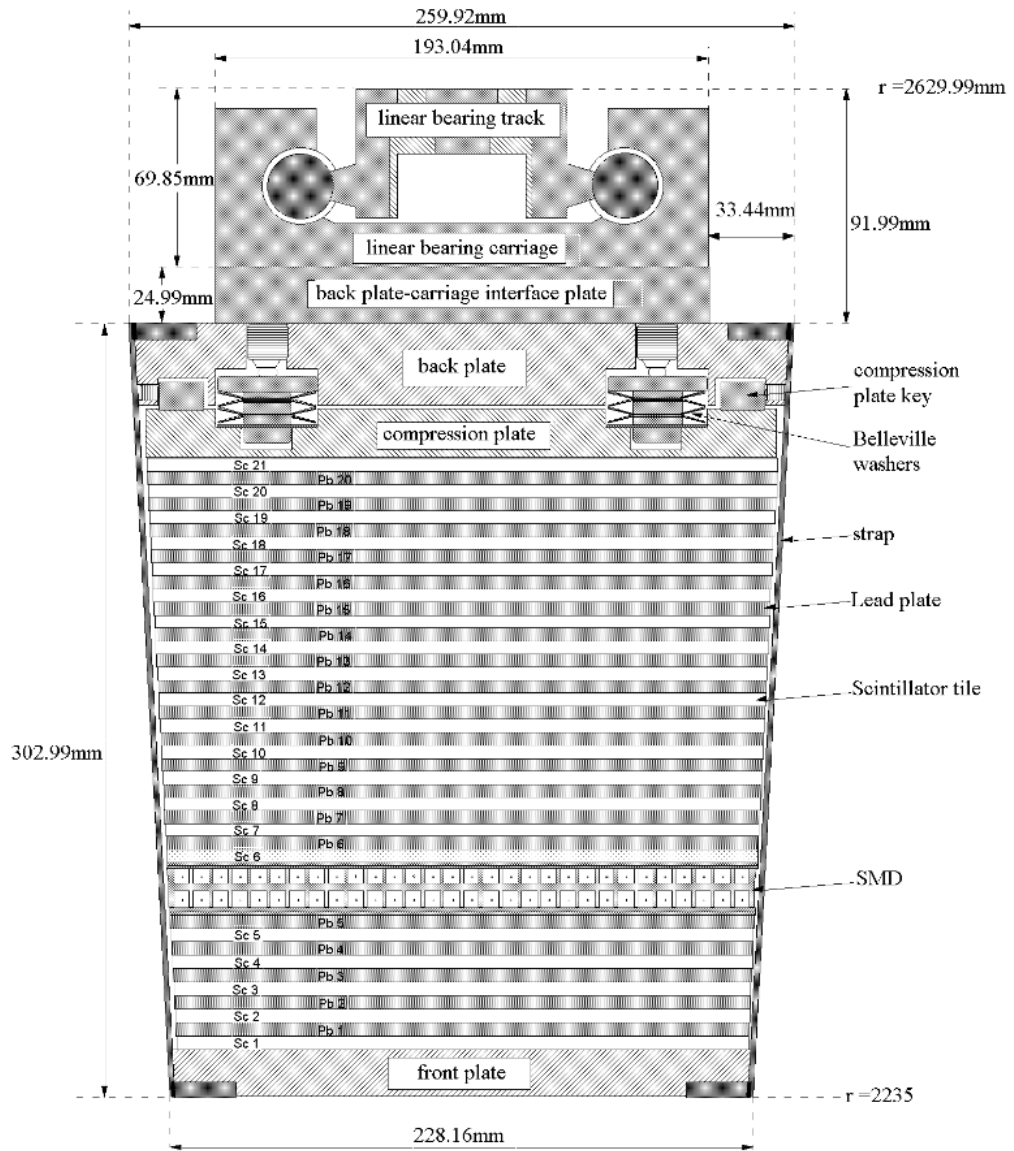


Figure 4.5: A schematic showing a cross sections of the BEMC tower. Taken from [65].

Chapter 5

Monte Carlo simulations of Upsilon meson production

Monte Carlo event generators (MCEGs) are a widely used tool in both theoretical and experimental high energy physics. In general, the Monte Carlo (MC) method refers to a variety of computational algorithms, which use stochastic (pseudo)random sampling to obtain numerical results of a given problem, which would be complicated to solve analytically. In the field of particle physics, they are widely used as a method to compare theoretical model predictions with real data, correct measured results for detector and other effects or to predict the results of experiments.

The author has used two MCEGs, PYTHIA 8.240 [69] and HERWIG 7.1.2 [70, 71] in his bachelor's thesis [72] to study the yield of the Υ meson on charged particle multiplicity in 500 GeV proton-proton collisions. The study focused on comparing the predictions given by the two different generators due to the different mechanisms they use to produce quarkonia. This analysis has served as a basis for a more in-depth study using the PYTHIA MCEG to examine the effects of either direct or inclusive Υ meson production, as well as differences between $\Upsilon(1S)$, $\Upsilon(2S)$ and $\Upsilon(3S)$ state yields with regards to the event multiplicity. This chapter will present a simple introduction to Monte Carlo event generators (specifically PYTHIA) and then will present and discuss the obtained results.

5.1 Monte Carlo event generators

When simulating particle collisions, Monte Carlo event generators employ multiple steps to describe the entire picture, from the initial partonic interactions, through hadronisation, to the decay of unstable particles. For the quarkonium production studied in this thesis, the simulation sequence of an event generator can be divided into following steps:

1. hard process,
2. parton showers,

3. hadronisation,
4. particle decay.

The entire process starts with the initial interaction of selected particles, in this case two protons. This consists of multiple processes, such as a hard perturbative process, MPI, initial and final state radiation or beam remnants. Using the pQCD framework, the generators utilise so called parton distribution functions (PDFs), which describe the positions of the partons in the proton. The hard process can be described by a short distance matrix element (SDME), which is responsible for a $Q\bar{Q}$ quark pair creation. However, the hard process is usually described in terms of partonic cross section for a process (in this case for example $gg \rightarrow Q\bar{Q}$). The produced pair is then used to form a bound state, which utilises the long distance matrix elements mentioned in Chapter 2. This allows for the selection of a specific bound state in a particular production channel to be generated. In the case of PYTHIA, it allows for Υ meson production in different ways, such as gluon fusion, as well as quark-gluon interaction and quark-antiquark interaction (also discussed in Chapter 2) via the selection of SDMEs. The Υ states can also be produced in multiple channels, such as the colour singlet or colour octet channel using the LDMEs.

The next part of the process consists of partonic showers, which describe the evolution of the partons from the initial process. Since the partons (quarks and gluons) carry a colour charge, there is the possibility of a gluon emission. This is true for any partons, whether they are interacting or leaving the interaction zone. And since the gluons carry such a charge as well, they too can emit additional gluons. This results in a series of increasingly softer partons, which can be modelled using sequential algorithms describing the time evolution. This can be utilised from the moment of interaction up to the point, where the momenta are so low they can no longer be described using perturbative calculations. PYTHIA uses p_T -ordered showers in its algorithm.

After modelling the parton showers, the remaining particles need to be bound into colourless hadrons in a process called hadronisation. PYTHIA uses a so called Lund string hadronisation model [73]. The basis for this model is the assumption, that a quark and an antiquark, which the model treats as massless, originate in the same space-time point and begin moving away from each other at the speed of light. As they continue, the strong interaction causes the aforementioned strings of colour field to be formed between them, which are under a constant tension until all of the quark-antiquark pair's kinetic energy is converted into the potential energy contained in the string. At this point this process reverses and the string's tension begins to pull the partons back together. Another option is, that the pair has enough kinetic energy to break the string's tension. At this point, since the quarks cannot exist individually, but have to be bound in colourless composite particles, a new $q\bar{q}$ pair is formed in the middle of the broken string in a process which fragments the original hadron into a system of two mesons. This fragmentation occurs in every pair with a high enough energy. The model's most important idea is the colour confinement, which is motivated by phenomenological predictions. Its downside is a large amount of free parameters, which need to be tuned in order to match the experimental data.

5.2 Simulation

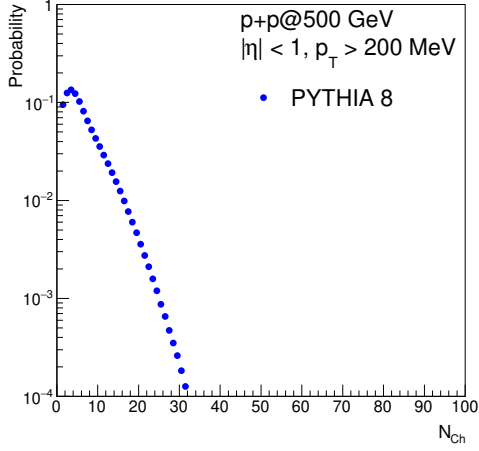
In this study, PYTHIA was used to simulate both direct and inclusive $\Upsilon(1S)$, $\Upsilon(2S)$ and $\Upsilon(3S)$ samples. Directly produced bottomonium is created from a $b\bar{b}$ pair at the beginning of the collision, whereas inclusive bottomonium refers to a particle created either directly, or via a feed-down. It implements their production using the aforementioned long distance matrix elements in colour singlet and colour octet states. On top of these three $\Upsilon(nS)$ states, PYTHIA implements three bottomonium P -states: $\chi_{bj}(1P)$, $j = 0, 1, 2$, which have a mass greater than $\Upsilon(1S)$, but smaller than $\Upsilon(2S)$ (for a more detailed information about these states see chapter 2). These all contribute towards the inclusive studies, since the feed-down into lighter bottomonia is also implemented.

An important note needs to be raised here. The cross sections of the $\chi_{bj}(1P)$ states may not be accurate and therefore their contribution to the yield of the $\Upsilon(1S)$ state may not be physically accurate. This is due to the values of the long distance matrix elements PYTHIA uses. While for the $\Upsilon(nS)$ states the values seem to correspond to the theoretical calculations and the values obtained from experimental data [74, 75], for the $\chi_{bj}(1P)$ only a value for $\chi_{b0}(1P)$ is given [74, 75], which is then used for $\chi_{b1}(1P)$ and $\chi_{b2}(1P)$ as well. This calls for a more thorough study, which should look more into the cross sections of the implemented bottomonia and compare the sources of $\Upsilon(nS)$ given by PYTHIA with the ones from experimental measurements shown in Fig. 2.2.

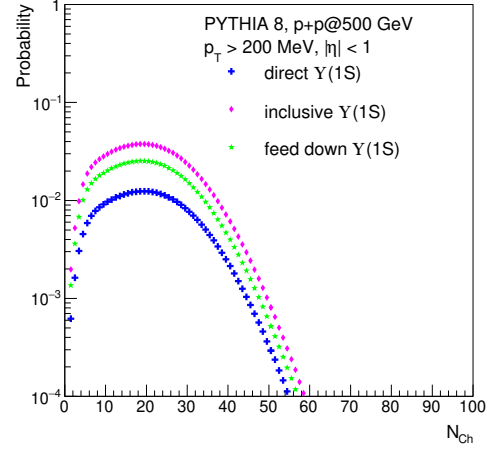
PYTHIA's implementation of those states allows for the comparison of direct and inclusive $\Upsilon(1S)$, where the feed-down is possible from $\Upsilon(2S)$, $\Upsilon(3S)$, $\chi_{b0}(1P)$, $\chi_{b1}(1P)$ or $\chi_{b2}(1P)$, as well as direct and inclusive $\Upsilon(2S)$, where the feed-down contribution is from $\Upsilon(3S)$ only. Since $\Upsilon(3S)$ is the heaviest bottomonium state implemented in PYTHIA, it can be produced only directly.

Since the study was intended as a comparison to the STAR experiment data studied in this thesis, the simulation was set up to reflect that. The chosen collision system was proton-proton at a centre-of-mass energy of 500 GeV. The tracks used for charged particle multiplicity measurement were selected in order to match the STAR detector acceptance. The pseudorapidity of a given particle was required to be $|\eta| < 1$, the transverse momentum $p_T > 0.2$ GeV/ c and the particle had to be stable ($\tau > 10$ mm/ c). A dataset of minimum bias events containing 1.6 billion events was generated in order to be used in calculating the normalised event multiplicity. Three distinct datasets for $\Upsilon(1S)$, $\Upsilon(2S)$ and $\Upsilon(3S)$ were generated. In each case, the state in question has been set up to decay into an electron-positron pair in order to streamline the generation as much as possible and to save up computational resources. Only the matrix elements of the particles, which could contribute via the feed-down effect, were enabled in each of the simulations. The datasets contained 1.5 billion events for $\Upsilon(1S)$, 700 million events for $\Upsilon(2S)$ and 600 million events for $\Upsilon(3S)$. Fig. 5.1 shows the distributions of charged particle multiplicity for minimum bias and Υ events and Fig. 5.2 shows the Υ meson transverse momentum distributions. Fig. 5.3 shows multiplicity and transverse momentum distributions for $\Upsilon(1S)$

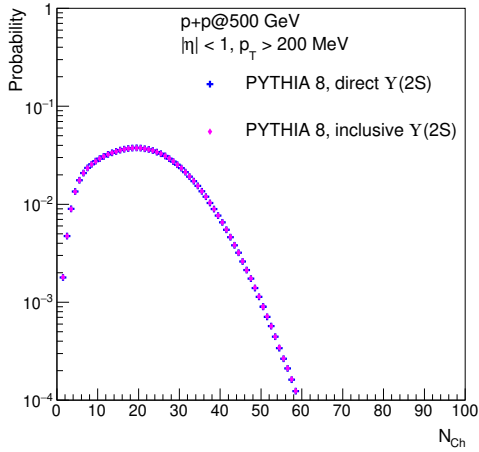
separated by the source of the feed-down, as well as the comparison between the three Υ states studied.



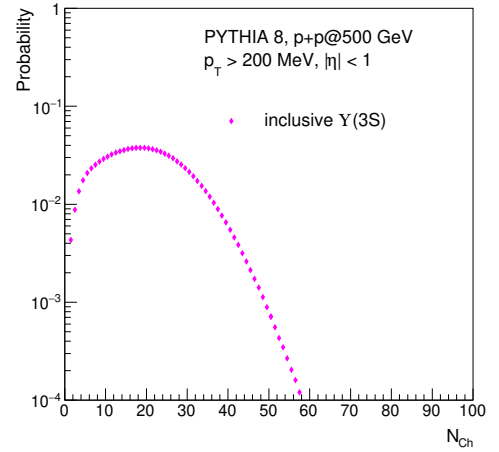
(a) Multiplicity distribution of minimum bias events generated by PYTHIA MCEG.



(b) Multiplicity distributions of direct, inclusive and feed-down $\Upsilon(1S)$ events generated by PYTHIA MCEG.

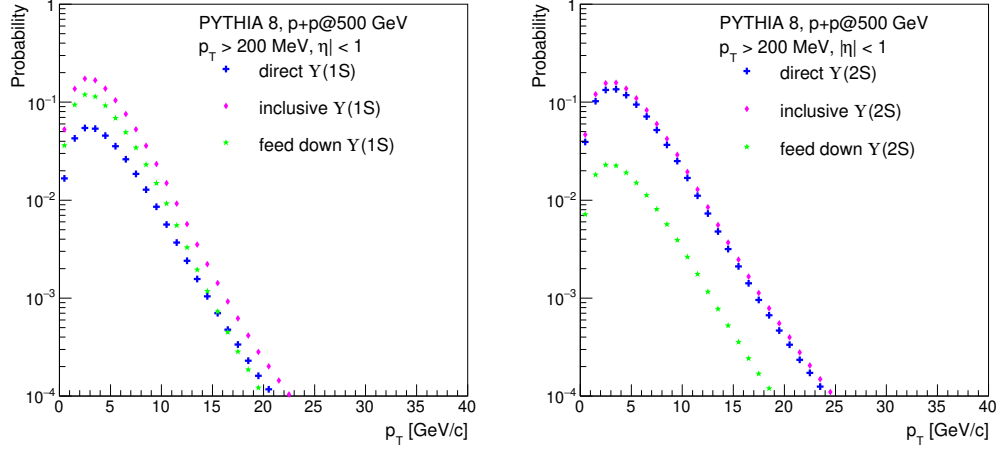


(c) Multiplicity distributions of direct and inclusive $\Upsilon(2S)$ events generated by PYTHIA MCEG.

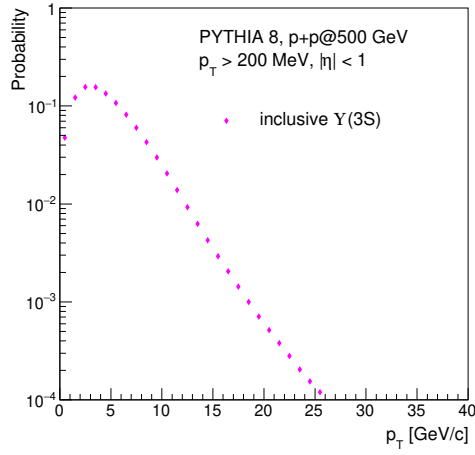


(d) Multiplicity distribution of inclusive $\Upsilon(3S)$ events generated by PYTHIA MCEG.

Figure 5.1: Multiplicity spectra generated by PYTHIA MCEG.

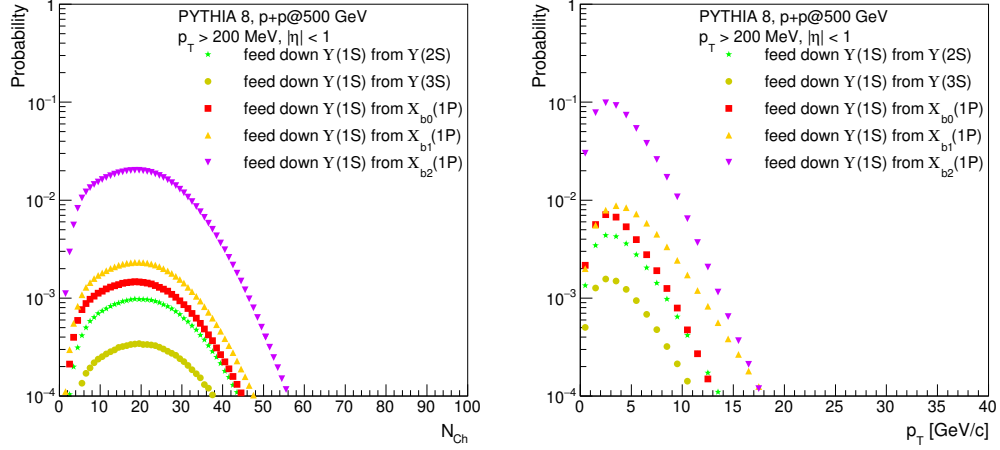


(a) Transverse momentum distributions of direct, inclusive and feed-down $\Upsilon(1S)$ events generated by PYTHIA MCEG. (b) Transverse momentum distributions of direct, inclusive and feed-down $\Upsilon(2S)$ events generated by PYTHIA MCEG.

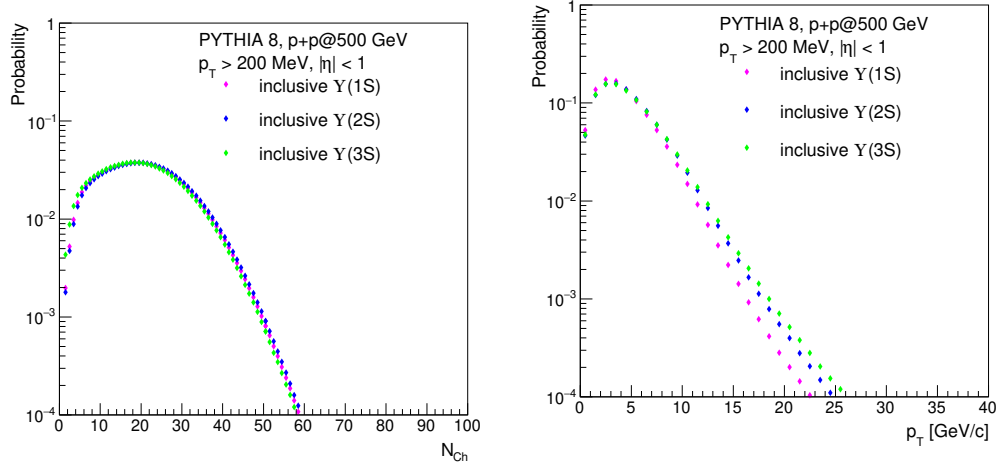


(c) Transverse momentum distribution of inclusive $\Upsilon(3S)$ events generated by PYTHIA MCEG.

Figure 5.2: Transverse momentum spectra generated by PYTHIA MCEG.



(a) Multiplicity distributions of non-direct $\Upsilon(1S)$ events separated by the originating particle of the Υ state. (b) Transverse momentum distributions of non-direct $\Upsilon(1S)$ events separated by the originating particle of the Υ state.



(c) Multiplicity distributions of inclusive $\Upsilon(1S)$, $\Upsilon(2S)$ and $\Upsilon(3S)$ events. (d) Transverse momentum distributions of inclusive $\Upsilon(1S)$, $\Upsilon(2S)$ and $\Upsilon(3S)$ events.

Figure 5.3: Multiplicity and transverse momentum spectra generated by PYTHIA MCEG.

This study includes the comparison to preliminary STAR data [76]. Normalised event multiplicity of Upsilon yield was calculated using the equation Eq. 2.7 and both PYTHIA and HERWIG simulations. $N_{ch}/\langle N_{ch} \rangle$ binning was selected in correspondence to STAR preliminary data: 0-1, 1-2, 2-3, 3-8 and 8-100 (overflow bin). The results for direct, inclusive and non-direct $\Upsilon(1S)$ with the comparison with STAR preliminary data is seen on Fig. 5.4. It can be seen, that at higher multiplicities the data generated in this thesis predicts higher values for the normalised yield, whereas in the lower multiplicities the STAR preliminary data shows higher yield. Both show a higher than linear increase of the yield with regards to normalised charged particle multiplicity. Fig. 5.5 shows the non-direct $\Upsilon(1S)$ separated

by the particle, from which they originate. Direct, inclusive and non-direct $\Upsilon(2S)$ results are presented in Fig. 5.6 and inclusive $\Upsilon(3S)$ results are shown in Fig. 5.7. Fig. 5.8 shows the comparison of the inclusive data for all studied states. For the $\Upsilon(1S)$ and $\Upsilon(2S)$ states the results show little to no quantitative difference between direct and inclusive Υ mesons. This is despite the fact that two pions are produced in the $\Upsilon(nS) \rightarrow \Upsilon(1S)\pi^+\pi^-$ decays. It is important to note, that the $\Upsilon(3S)$ state is produced only directly via direct matrix elements in PYTHIA. The difference between the marker placement of the data generated in this study and the STAR preliminary data [76] may be attributed to the suspected difference between the multiplicity spectra and subsequent different normalised multiplicity.

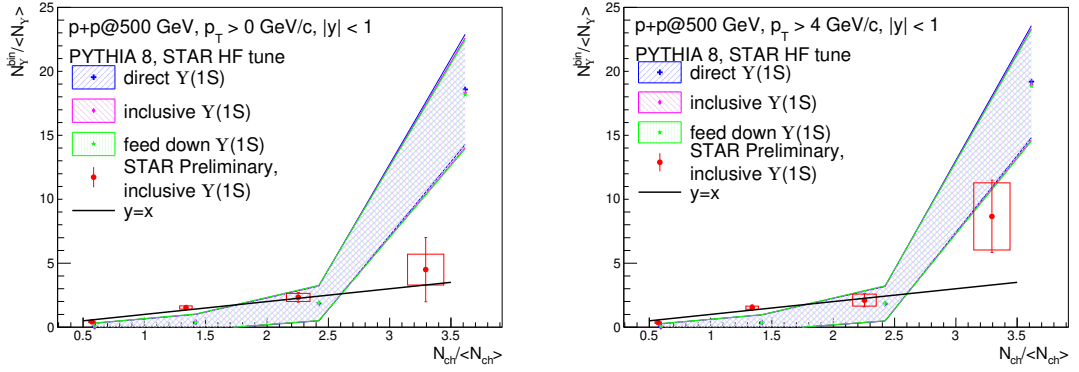


Figure 5.4: Normalised direct, inclusive and non-direct (feed-down) $\Upsilon(1S)$ yield dependence on normalised multiplicity for PYTHIA compared to STAR preliminary data [76]; Left: p_T integrated; Right: $p_T > 4$ GeV/c. The results for directly, inclusively and non-directly produced states simulated by PYTHIA are overlapping.

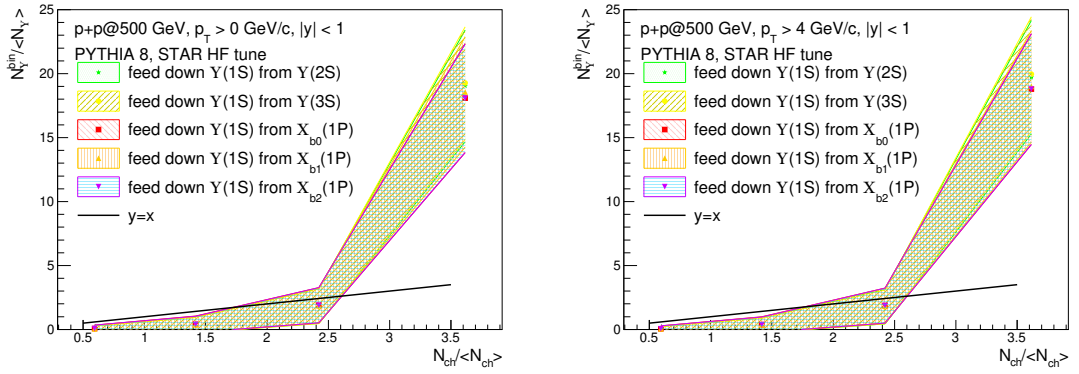


Figure 5.5: Normalised non-direct (feed-down) $\Upsilon(1S)$ yield dependence on normalised multiplicity for PYTHIA. The data is separated by the quarkonium state, from which the $\Upsilon(1S)$ originated; Left: p_T integrated; Right: $p_T > 4$ GeV/c. The results for non-directly produced states simulated by PYTHIA are overlapping.

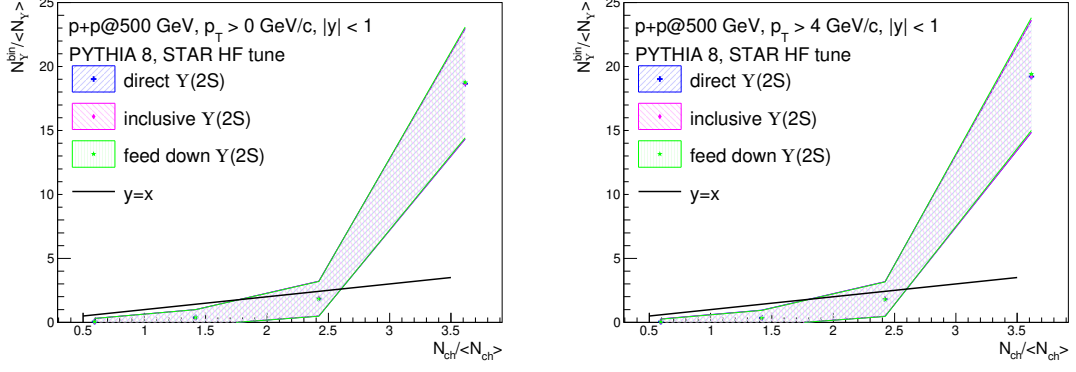


Figure 5.6: Normalised direct, inclusive and non-direct (feed-down) $\Upsilon(2S)$ yield dependence on normalised multiplicity for PYTHIA; Left: p_T integrated; Right: $p_T > 4$ GeV/c. The results for directly, inclusively and non-directly produced states simulated by PYTHIA are overlapping.

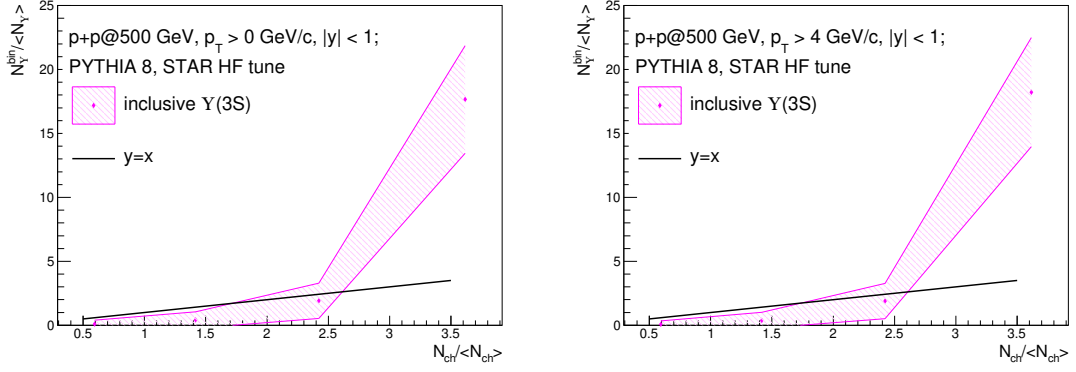


Figure 5.7: Normalised inclusive $\Upsilon(3S)$ yield dependence on normalised multiplicity for PYTHIA; Left: p_T integrated; Right: $p_T > 4$ GeV/c.

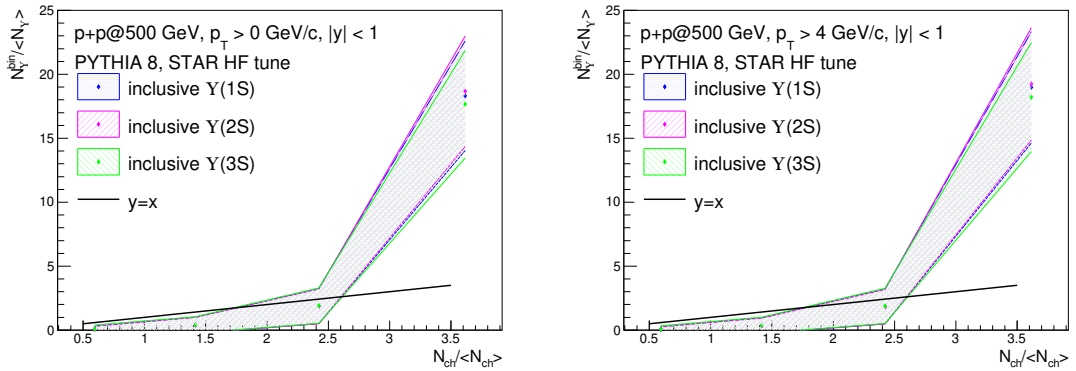


Figure 5.8: Normalised inclusive $\Upsilon(1S)$, $\Upsilon(2S)$ and $\Upsilon(3S)$ yield dependence on normalised multiplicity for PYTHIA; Left: p_T integrated; Right: $p_T > 4$ GeV/c.

Chapter 6

Experimental data analysis

The figures and results presented in this thesis are a work in progress. They should not be considered neither preliminary or final and are not approved by the STAR collaboration.

6.1 Software and resources

The analysis performed in this study is based on the ROOT data analysis framework [77]. The ROOT package is an object oriented data analysis framework directed towards large volume data analysis and is widely used in the field of high energy physics. The used version of ROOT is based on the C++ programming language, which is the main programming language utilised for data analysis in this study. The `root4star` is an extension of the ROOT package developed by the STAR collaboration for the use on the machines available to its members.

This work has been done utilising the computational resources provided by the Scientific Data and Computing Center (SDCC) [78], an organisation subject to the Brookhaven National Laboratory, which is responsible for data storage, transfer and computational resources, which is in use by BNL members and associates. In this study it was used to access the data and to run the analysis. The data used is stored in the STAR `picoDst` format, which makes use of standard ROOT classes and contains ready to analyse classes representing reconstructed events and tracks.

The calculations needed for the analysis were done using SDCC's RHIC and Atlas Computing Facility (RACF), which is a computing and data storage cluster. It can be accessed using the `ssh` package and offers the user a remote terminal utilising the `tcsh` shell. It offers a STAR scheduler which interfaces with the `condor` high throughput computing system system used for effective distribution and management of parallel computing tasks on the RACF cluster.

6.2 Dataset

This thesis is aimed at analysing the proton-proton particle collisions at centre-of-mass energy of 510 GeV, which was performed by the RHIC particle collider and measured by the STAR experiment in 2017 in its Run17. This entire dataset contains about 2.9 billion recorded particle collisions using various triggers. A trigger is a system, which decides whether to record a collision during the data taking process and can be implemented in hardware or software. This is done in order to reject unsatisfactory collisions, as well as to help the physicists interpreting the data in event selection, which saves time, computational resources and disk space. The main trigger used in this analysis is the Barrel High Tower (BHT) trigger 2 in conjunction with two hits in the Beam Beam Counter (BBC) - BHT2*BBCMB. The BHT2 trigger requires a high energy hit in a BEMC tower to trigger. Around 560 million events satisfy these trigger conditions and are used in subsequent analysis. The BHT2*BBCMB is an immediate, level 0 (L0 - lowest level electronics) trigger. Another trigger was also used, the BHT1*VPD100, for additional checks on the validity of the analysis. This trigger also requires an energetic hit in the BEMC (although lower energy than the BHT2), as well as the z position (along the beamline) of the primary vertex recorded by the VPD to be less than 100 cm in either direction.

The BHT2*BBCMB triggered subset of the data offers an integrated luminosity of $\int \mathcal{L} dt \simeq 340 \text{ pb}^{-1}$. Luminosity is a quantity used in collider experiments as a measure of the accelerator. It is defined in Eq. 6.1 as a ratio of the number of particle collisions N in a time t to the interaction cross section. The integrated luminosity (often denoted \mathcal{L}_{int}) is a cumulative luminosity over a given time period (in this case, the entire Run17). The integrated luminosity provided by this dataset is an improvement over the previous STAR preliminary results [76], which offers $\int \mathcal{L} dt \simeq 22 \text{ pb}^{-1}$ recorded during Run11 using the BHT1 trigger.

$$\mathcal{L} = \frac{1}{\sigma} \frac{dN}{dt} \quad (6.1)$$

As hinted in the previous section, the data is not in a raw form when the analysis is performed. Rather, the information from the detectors is collected and subsequently *reconstructed* - converted in a more convenient format for physical analysis. Among other things, the reconstruction finds the hits the particles leave in the detectors, as well as reconstructs the vertices. These hits are then fitted in order to find the presumed tracks of the particles. The STAR algorithm uses the Kalman filter to reconstruct the tracks. The information is then converted into the `picoDst` data storage scheme and stored in ROOT files. The size of the entire `picoDst` Run17 proton-proton reconstructed dataset is roughly 45 terabytes. The data used in this thesis was reconstructed with the BEMC information missing in the final data available to the user. The consequences of this will be addressed later. The author was involved in the quality assurance of the new Run17 p+p data reconstruction. This work is discussed later in Section 6.4.

6.3 Data analysis

The entire analysis is done in several parts, each of which is directed towards extracting useful information from the entire dataset. The analysis starts with finding the corresponding dataset on the computational cluster and submitting the analysis and the dataset into the submission queue. The analysis code first performs an event selection, where it accepts only the events satisfying the trigger conditions and the cuts imposed on the entire event. Next, the code goes through the reduced dataset event by event, where it applies the main body of the code directed towards selecting valid particles in a form of tracks. The track selection is done in order to ensure only properly reconstructed tracks are selected and used in the further part of the analysis. Simultaneously, tracks are selected for the charged particle event multiplicity measurement. In this analysis this is done via a quantity called *TofMult*, which also uses the coincidence in the Time Of Flight detector. Furthermore electron and positron candidates are selected from the accepted tracks. Since this study is aimed at measuring the Υ meson in the electron-positron decay channel, properly finding the candidates for its reconstruction is the key part in obtaining a clean sample. This step will utilise data from the Barrel Electromagnetic Calorimeter, which provides a good separation of leptons and hadrons. This is needed due to the fact that at relativistic speeds the Time Projection Chamber has a hard time separating electrons and pions. After the electron and positron candidates are found, they are used to reconstruct the Υ candidates, as well as combinatorial background, which is then used to extract the Υ signal from the data.

6.3.1 Event selection

As mentioned in the introduction to this section, event selection is the first part of the actual analysis. This is performed to reduce the computational complexity of the analysis. This analysis is directed towards finding the electrons, which are presumed to come from a Υ decay. Since the Υ meson is heavy ($m_{\Upsilon} \simeq 9.46 \text{ GeV}/c^2$; for the precise value see Chapter 2), the electron and positron from the decay will be very energetic due to energy conservation. Therefore, it would be efficient to analyse only those events, where at least one electron or positron with high energy are found. This is implemented via various triggers, which help to categorise events using certain conditions. The aforementioned BHT2*BBCMB trigger primarily requires a high energy track to be recorded in the BEMC. This is implemented by an online *DSMadc* trigger threshold represented by a 6-bit variable. The value of this hit is roughly $E_T = 3.5 \text{ GeV}$ of transverse energy. This makes it an ideal trigger to select events, which may contain an Υ decay. The trigger information is stored in the data structure of the `picoDst` files. Each event is represented as a C++ class, `StPicoEvent`, which contains an attribute, which stores all of the so called trigger flags. If the event passes a particular cut, the trigger ID of said trigger will be included in this attribute. The used BHT2*BBCMB trigger is represented by three distinct flags: 30, 570205 and 570215. Events, which were recorded during the time, when the detector was not functioning properly (a so called bad run) and thus are

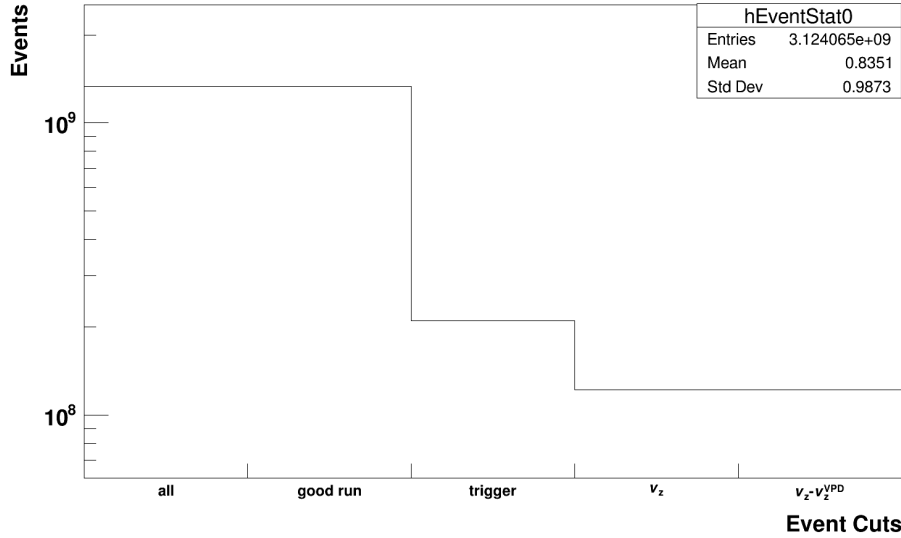


Figure 6.1: Comparison of the number of accepted events in the stages of event acceptance. The stages (going from left to right) are: before applying cuts, after removing bad runs, after applying trigger conditions, after applying the V_z cut and after applying the $v_z - v_z^{\text{VPD}}$ cut.

deemed bad are listed in a list of bad runs, which is also checked at this time. No bad runs were removed in this analysis due to no bad run lists being available.

Additional requirement on the events is also imposed in this step of the analysis on top of the trigger flags. The only one used is the position of the primary vertex. The reconstructed primary vertex needs to be positioned within 40 centimetres, $|v_z| < 40$ cm, on either side from the centre of the TPC detector in the longitudinal direction, or the z axis (along the beamline). If there are more primary reconstructed vertices, the one with the best reconstruction is selected. This is imposed to ensure the uniform acceptance of the tracks in the detector. If the primary vertex is positioned outside of this range, the tracks on one side of the detector may not be detected in the rapidity window, in which the analysis is performed. Some analyses also apply the difference between the primary position given by the reconstruction algorithm v_z and the Vertex Position Detector v_z^{VPD} . This is not used in this analysis, since this cut is mainly used in ion-ion collisions and since this is a proton-proton dataset, it was deemed unnecessary towards the quality of the selected events. A comparison of the number of events accepted in each step of the analysis is shown in Fig. 6.1. An overview of the cuts used in the event selection part of the analysis is presented in Tab. 6.1.

trigger ID	30, 570205, 570215
$ v_z $	< 40 cm

Table 6.1: An overview of the cuts used in the event selection part of the analysis.

6.3.2 Track selection

Selection of only good quality tracks is necessary due to detector effects such as deadtime and pileup, as well as imperfections in the tracks reconstructed by the track finding and fitting algorithm. The tracks, which are rejected in this step include improperly or inefficiently reconstructed tracks, pileup tracks, secondary tracks knocked out of the detector material or split tracks. The pileup tracks are particles, which originate from a particular event, but are read out in a subsequent event due to the TPC being a slow detector. This brings many complications, notably it changes the charged particle multiplicity of both events, which would bring unnecessary biases into this particular measurement. The secondary tracks emerge, when a particle knocks out another particle upon hitting the material of the detector. This introduces additional tracks, which do not originate in the particle collision and therefore would only spoil the measurement of the given event. These can be removed using a DCA cut. Split tracks are an artefact originating from the fitting algorithm, which poorly reconstructs a presumed particle's track. Another issue are tracks, which are reconstructed using an insufficient amount of hits in the detector. These would introduce a significant amount of uncertainty into the measurement and are therefore also removed. Another point is also only selecting primary tracks. The primary tracks originate from the main collision vertex, compared to secondary tracks, which are created by the decay or interaction of the primary tracks with the detector. In the first part of the track reconstruction, all of the tracks are labelled as global and are fitted without the primary vertex. In the next pass the algorithm extends the tracks towards the main vertex and if the trajectory includes this vertex, they are labelled as primary tracks. This creates two distinct tracks for the primary particles - a global version without the vertex used for fitting and a primary version with the vertex included. These tracks may have different properties. An overview of the used track quality cuts is presented in Tab. 6.2.

$nHitsFit$	≥ 20
$nHitsRatio$	> 0.52
DCA	$< 3 \text{ cm}$
p_T	$> 0.2 \text{ GeV}/c$

Table 6.2: An overview of cuts applied in the track selection part of the analysis.

In order to avoid the badly reconstructed and split tracks, one can use the amount of hits, which are used to reconstruct a track. When a particle is produced in a collision and enters the TPC detector, it ionises the TPC gas creating electrons, which are collected and used for track reconstruction and finding. In the barrel part of the TPC, which covers the pseudorapidity range of $-1 < \eta < 1$ and a full azimuthal range of $0 < \phi < 2\pi$, the maximum number of possible hits a particle can leave and can be read out is 46, which is denoted $nHitsMax$. This quantity is called $nHitsFit$ in this thesis and refers to the number of said hits used to reconstruct a given track by the fitting algorithm. This allows an adequate resolution of the track, mainly the reconstructed particle's momentum. The value chosen in this analysis is $nHitsFit \geq 20$. The choice was based on previous analyses (such as [76]) and

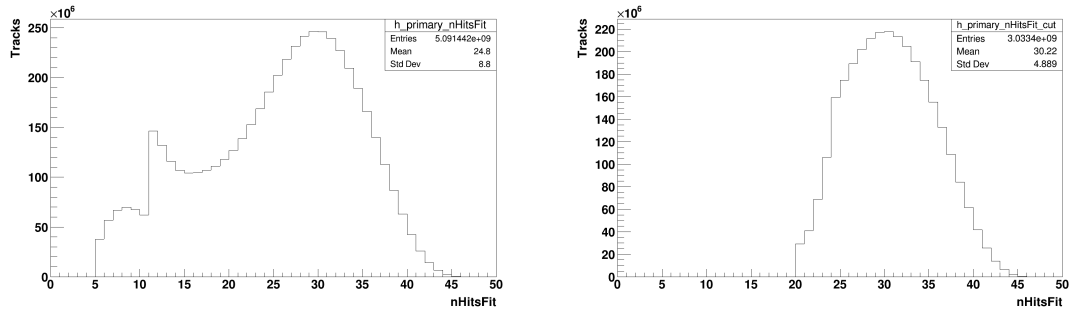


Figure 6.2: The distribution of TPC hits used for track fitting $nHitsFit$ for all analysed primary tracks before (left) and after (right) applying track quality cuts.

testing. An additional cut on the amount of hits is imposed. The distribution of track $nHitsFit$ before and after applying the track quality cuts is shown in Fig. 6.2. This is the ratio of the hits of the track and the maximum amount of hits, which is 45, with an additional one being the primary vertex. This quantity is defined as $nHitsRatio = nHitsFit/nHitsMax$. This cut is implemented due to the fact, that during the data taking, parts of the TPC may be turned off for various reasons, changing the $nHitsMax$. The $nHitsMax$ also depends on the pseudorapidity of the track, since the particles in forward directions may miss some of the pad rows of the MWPCs and are not able to produce the maximum 45 tracks. The value of $nHitsRatio$ used in this thesis is $nHitsRatio > 0.52$. The distribution for primary tracks with and without track quality cuts can be seen on Fig. 6.3.

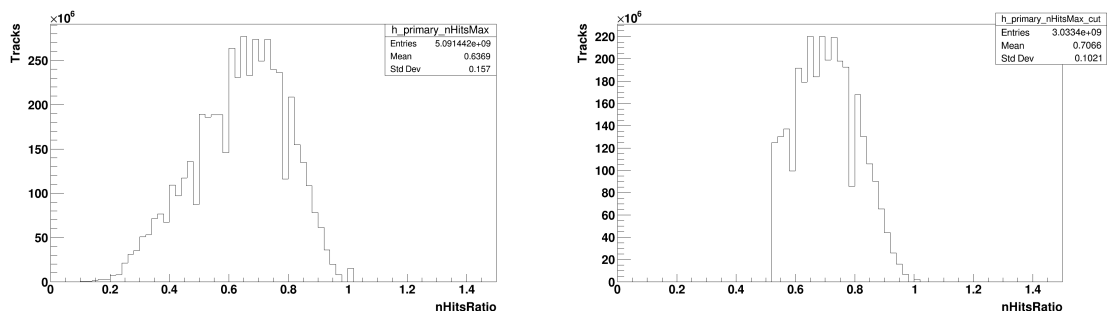


Figure 6.3: The distribution of the ratio of TPC hits used for track fitting to the maximum number of TPC hits $nHitsRatio$ for all analysed primary tracks before (left) and after (right) applying track quality cuts.

Additionally, on top of only requiring primary tracks for the further part of the analysis, the track's distance of closest approach to the main collision vertex DCA is checked and cut. This is already done in the reconstruction of the data, where the tracks with a small enough DCA are labelled as primary, but is implemented in this analysis, where various values were tested. The value of $DCA < 3$ cm was used, which coincides with the value used by the track fitting algorithm. Requiring the track to originate in the primary vertex removes the secondary knock-out tracks. The distribution of DCA in the xy plane is shown on Fig. 6.4. As can be seen, some of the primary tracks were removed by applying the track quality cuts.

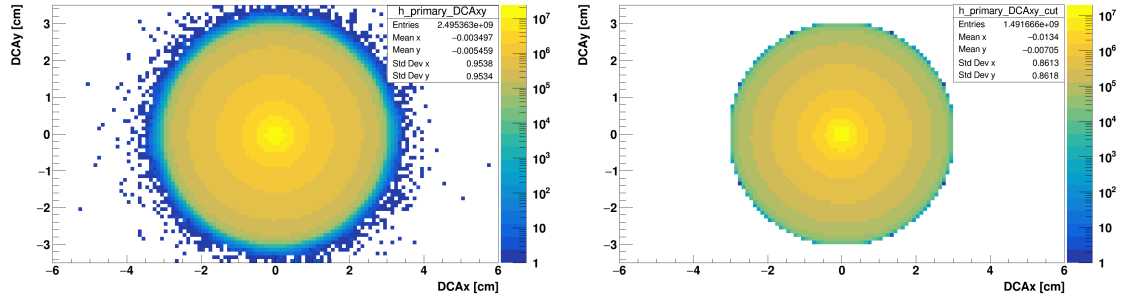


Figure 6.4: The distribution of the distance of closest approach DCA of primary tracks to the primary vertex in a transverse plane before (left) and after (right) applying track quality cuts. The plot features a logarithmic scale.

The STAR detector, as its name suggests, includes a strong solenoidal magnet, which is used to curve particles' trajectories in order to determine their momentum and charge sign. The momentum can only be measured thanks to the magnetic field bending the tracks. The strength of the STAR detector magnet is $B = 0.5$ T. This intense field and the curvature of the charged tracks it causes results in particles with low transverse momentum not reaching the detector. With increasing transverse momentum the particles are able to reach the detector, but are not properly reconstructed and need to be rejected. The cutoff used in this analysis is $p_T > 0.2$ GeV/c, which is consistent with other analyses done by the STAR collaboration. The primary track transverse momentum spectra can be seen on Fig. 6.5. The right plot, showing the version with the applied cut, uses the global p_T value to reject the small momentum tracks. Since the global p_T and primary p_T may vary, one does not observe a sharp cut-off precisely at 0.2 GeV/c.

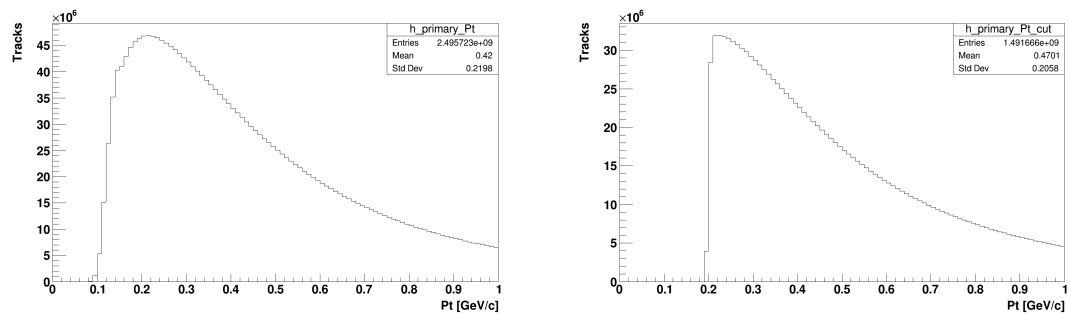


Figure 6.5: The distribution of the primary track global transverse momentum p_T before (left) and after (right) track quality cuts. The low p_T range of 0-1 GeV/c was selected to highlight the effect of the imposed cuts.

6.3.3 Electron and positron identification

The key part of this analysis is identifying the electrons and positrons which originate from the Υ meson decay. This requires isolating a pure sample of high energy electrons and therefore the rejection of as many hadrons as possible. Many hadrons

are produced during high energy collisions, e.g. pions π , kaons K or protons p . Two subdetectors of the STAR detector are primarily used to separate the leptons from the hadrons: the TPC and the BEMC. The TPC provides the characteristic energy loss for the particle travelling through the detector, while the BEMC provides the amount of energy deposited by the particle, which is the main purpose of an electromagnetic calorimeter.

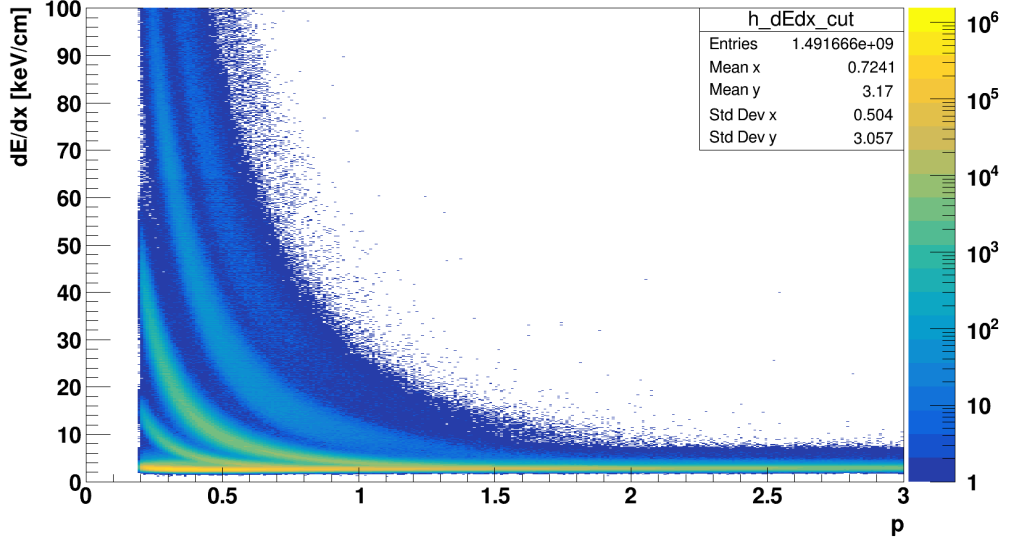


Figure 6.6: The dependence of TPC ionisation energy loss dE/dx on track momentum p for primary tracks with track quality cuts applied.

The characteristic ionisation energy loss of a particle travelling through a medium dE/dx is measured directly by the TPC. Each particle has a specific energy loss, which can be calculated using the Bichsel function [79] (which describes the dE/dx in gas better than the Bethe-Bloch formula). The dE/dx in dependence on the momentum p of the analysed tracks is shown on Fig. 6.6. As can be seen in the figure, certain 'bands' (area of the plot with increased amount of tracks) can be identified in the plot. Each of these bands corresponds to a different particle species. At low track momentum the particle type separation is significant and the ionisation energy loss could be used to identify particles precisely. However, with increasing track momentum the bands get closer together due to relativistic effects, until they overlap with each other. The apparent material density is higher for a relativistic particle due to Lorentz contraction. At high momenta, the velocity, at which the dE/dx depends, becomes similar for particles with different masses, resulting in a similar energy loss. Since this analysis requires electrons with a high p_T (the specific values will be discussed later), the energy loss alone is not sufficient to determine a particular particle species.

In order to illustrate this effect, it is necessary to introduce another variable. While the dE/dx may be used to try and identify the particle on its own, by comparing it to the predicted value, a more convenient approach is implemented in the `picoDst` data structure as a method of the `StPicoTrack` class. This quantity is the $n\sigma$, which is defined as

$$n\sigma_{\text{particle}} = \ln \left(\frac{dE/dx}{dE/dx|_{\text{expected}}} \right) / \sigma_{\text{TPC}}, \quad (6.2)$$

where the 'expected' energy loss is the one predicted by the Bichsel formula and the σ_{TPC} is the energy resolution of the TPC detector. This gives a deviation from the expected values in terms of the number of standard deviations $n\sigma$. The distribution of $n\sigma$ for electrons, pions, kaons and protons can be seen on Fig. 6.7. One may note, that the plots resemble the dE/dx plot (Fig. 6.6). This is due to the definition of $n\sigma$, which in essence 'shifts', or distorts the dE/dx distribution, to place the band corresponding to a certain particle species to be close to 0. As can be seen, the plots for electrons (top left) and pions (top right) look very similar, which is due to the pion being the lightest hadron to be detected in significant quantities and thus requiring a lower energy in order to become relativistic. Therefore, by using only TPC information, a significant pion contamination is introduced into the sample of electrons used for Υ signal reconstruction. However, $n\sigma_e$ is used as a cut on particles, which are selected as electron candidates. The value of the cut is $-3 < n\sigma_e < 3$. This is a wide acceptance window compared to other analyses which focus on identifying electrons (which often use a lower bound of -1.2). The reason is to offer a greater flexibility in the next part of the analysis. Since this information is stored, additional cuts on this quantity may be performed afterwards.

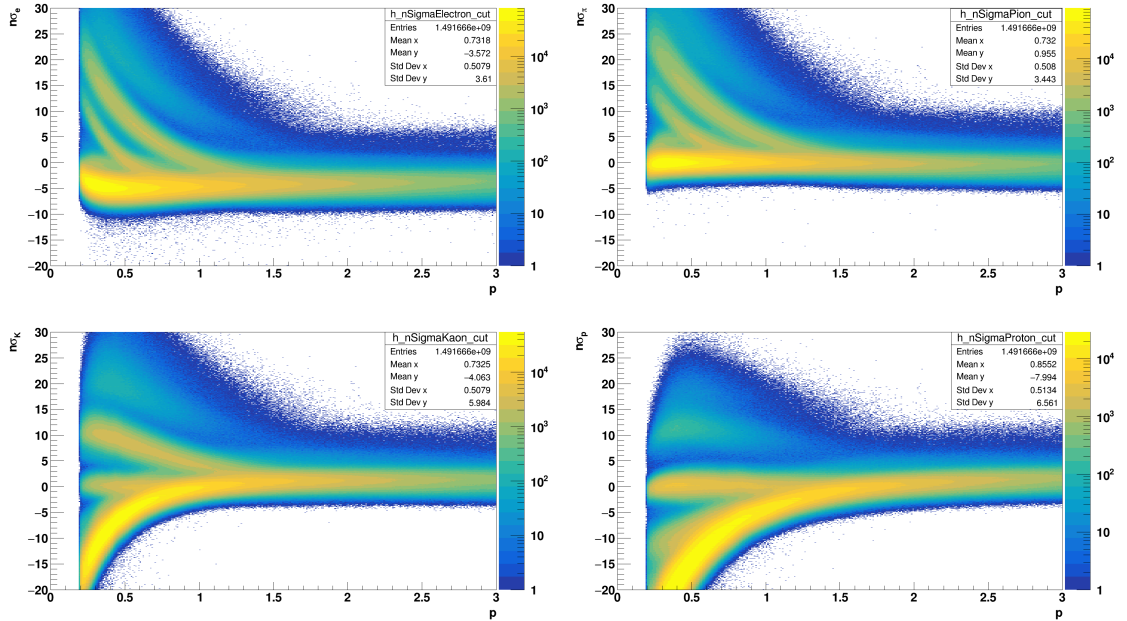


Figure 6.7: The distribution of $n\sigma$ and track momentum p for electrons (top left), pions (top right), kaons (bottom left) and protons (bottom right) for primary tracks with track quality cuts applied..

The BEMC offers precisely the information, which is required for the separation of electrons and pions. An electromagnetic calorimeter (compared to a hadronic one) is designed precisely towards the identification of particles, which interact primarily

via the electromagnetic interaction. A performance of an electromagnetic calorimeter may be described in terms of the response to leptons and photons, compared to hadrons. The BEMC of the STAR detector offers the same pseudorapidity and azimuthal coverage as the TPC. It is comprised of individual towers, which act independently. When a particle enters the electromagnetic calorimeter, it may hit one or more of these towers. When multiple towers are hit, the reconstruction algorithm attempts to group the towers, which are presumed to be hit by a single track, together into a cluster. The information about the energy deposited by a track into the cluster E_{CLU} and each particular tower E_{TOW} is accessible.

During the time the author was able to work on the analysis and thesis the dataset analysed was improperly reconstructed, resulting in the unavailability of the BEMC information. This prevented the author from applying any cuts requiring BEMC data. Therefore, only TPC information was used in order to select electrons in the presented results. A reproduction of the data has been discussed with the members of the STAR collaboration and the author has been involved in the quality assurance part of this process, which will be elaborated on further in the text. At the time of this thesis' submission the entire properly reconstructed dataset was made available to the users. However, this was not done in time to analyse this dataset and validate the results. Nevertheless, the author suggests two cuts utilising the newly available BEMC information to be used in the analysis in the future. The first cut is intended to select clusters, where the majority of energy has been deposited in a single tower, which should result in compact clusters with a high probability of only containing a single track. Such compact clusters are expected to be created by electrons, since they deposit most of their energy in a single tower. This should be done by applying $E_{\text{TOW}}/E_{\text{CLU}} > 0.5$. The second cut should purify the electron spectrum by requiring the ratio of the track's energy and momentum E/p to be close to the speed of light c . Since electrons are three orders of magnitude lighter than pions, this should ensure sufficient separation. The proposed cut would then be $0.5 < E_{\text{CLU}}/p < 1.5$. The applied and proposed cuts for electron and positron identification are summarised in Tab. 6.3.

$-3 < n\sigma_e < 3$
$E_{\text{TOW}}/E_{\text{CLU}} > 0.5$
$0.5 < E_{\text{CLU}}/p < 1.5$

Table 6.3: An overview of cuts used for electron selection. The applied cut is above the double-line, the proposed cuts are below.

6.3.4 Candidate reconstruction

The selected electrons and positrons are then considered as candidates from a Υ meson decay. In order to conserve disk space and computing resources, only high energy particles are selected. For a given pair, one particle is required to have a transverse momentum $p_{\text{T},1} > 3 \text{ GeV}/c$, while the other one needs a lower value of $p_{\text{T},2} > 1 \text{ GeV}/c$. This should be a conservative estimate. It should retain electrons from

Υ meson decay due to high efficiency. Additionally, the cuts should remove a significant portion of the background, which can be seen as a large decrease in the number of electron pairs. Those values are listed in Tab. 6.4. This analysis utilises both unlike-sign pairs (which include one electron and one positron), as well as like-sign pairs (either two electrons or two positrons). The unlike-sign pairs are considered Υ candidates. However, this sample also includes a background. The like-sign pairs are also reconstructed and then used as an estimate of a combinatorial background.

$p_{T,1} > 3 \text{ GeV}/c$
$p_{T,2} > 1 \text{ GeV}/c$

Table 6.4: An overview of cuts used for Υ candidate reconstruction.

Before discussing the background estimation and subtraction, it is important to introduce the concept of invariant mass of a pair. The invariant mass is a Lorentz invariant quantity. For a single particle, it corresponds to its rest mass. For a system of particles, it is a square root of the difference between the square of energy and a square of momenta. The invariant mass of the decay products is the same as that of the original resonance, as its rest mass-energy is converted into the kinetic energy of the decay products. In the centre-of-mass frame the relations for momenta $\vec{p}_1 = -\vec{p}_2$ and $\vec{p}_1 + \vec{p}_2 = 0$ hold true. This leaves only the energy component corresponding to the mass-energy of the resonance. For the case of an electron pair, the invariant mass is calculated as

$$m_{ee} = \sqrt{(E_1 + E_2)^2 - (\vec{p}_1 + \vec{p}_2)^2}, \quad (6.3)$$

where E_1 and E_2 are the energies and \vec{p}_1 and \vec{p}_2 are the momenta of the two particles used to construct the pair. In this analysis, the invariant mass is calculated for each unlike- and like-sign pair. Using this information, these spectra can be plotted out. One such example is shown on Fig. 6.8 for illustration. The next part of the signal extraction is the subtraction of the like-signed invariant mass distribution from the unlike-signed one. This is done using the TH1D class from the ROOT framework. This class provides an implementation of a histogram, where this subtraction can be conveniently implemented on a bin-by-bin basis.

6.3.5 Charged particle multiplicity

Another important component of the analysis is the determination of the charged particle multiplicity in a given event, since this is the aim of the study. The requirements on this measure are strict, since the event multiplicity may be influenced by detector effects, such as pile-up, which would influence the measurement and introduce systematic errors. The Time Of Flight detector works at a fast rate and can be used to remove the pile-up, which may be present in other detectors such as the TPC. In order to get a reliable measure of N_{ch} , tracks need to be matched to hits in the TOF, as well as further cuts need to be applied. The quantity used for this purpose is named *TofMult*.

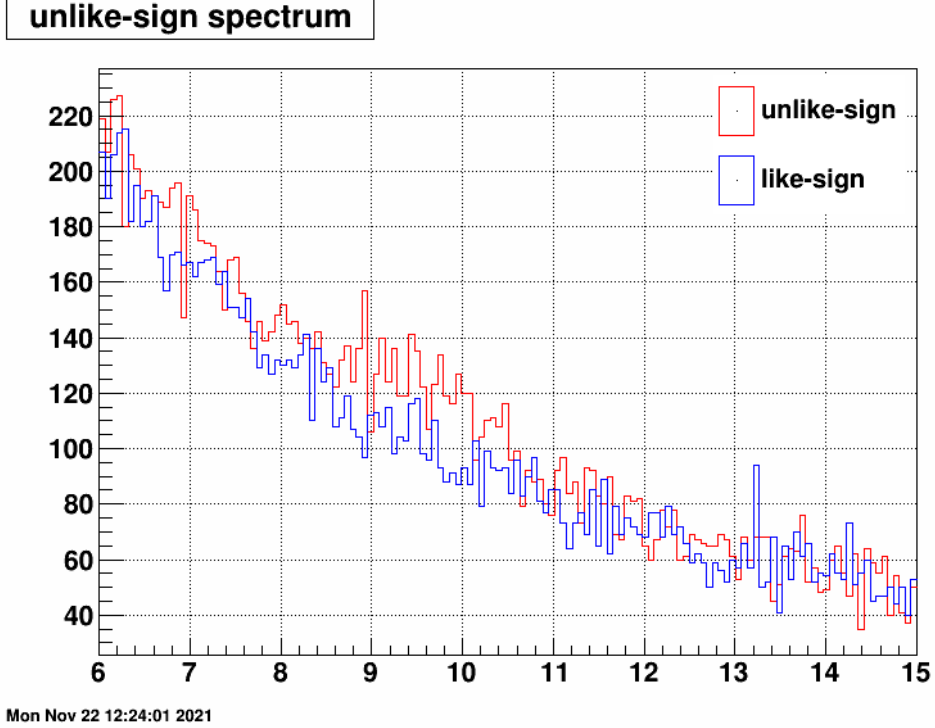


Figure 6.8: The invariant mass spectra for unlike-signed (red) and like-signed (blue) pairs.

The tracks require additional cuts in order to ensure uniformity and reliability of the measurement. Therefore a pseudorapidity constraint of $|\eta| < 1$ is implemented. For the same reason as for other tracks (see Subsection 6.3.2), a transverse momentum is required to be $p_T > 0.2$ GeV/c. The TPC hit requirement was selected to be consistent with other measurements done by the STAR collaboration and was $nHitsFit \geq 15$. Lastly, a $DCA < 0.5$ cm cut was used for consistency. The cuts are summarised in Tab. 6.5.

matched TOF hit	
$ \eta $	< 1
$nHitsFit$	≥ 15
p_T	> 0.2 GeV/c
DCA	< 0.5 cm

Table 6.5: An overview of cuts used for the charged particle multiplicity $TofMult$ measurement.

6.4 Tests and validation of data reproduction

The author was involved in the reproduction of the dataset used in this thesis. This was due to the fact, that the dataset was not produced properly and therefore did not include the majority of the BEMC information required by the analysis for

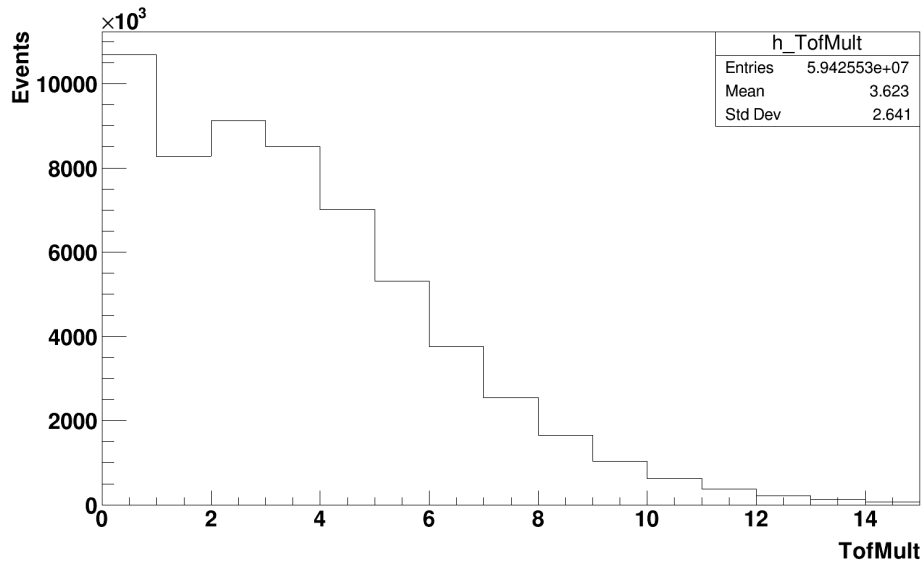


Figure 6.9: A distribution of the TOF matched charged particle multiplicity $TofMult$.

lepton and hadron separation. The fact was reported to the STAR collaboration and the dataset was scheduled for reproduction. The author was asked to be involved in the process by validating the quality of the reproduced data and checking, whether all of the necessary information was included and could be accessed properly. This section presents a brief overview of the work done and illustrates, that the newly produced files contain the BEMC information and it could be used in the future for the purpose of this analysis. This quality assurance work was done on a small subset of the entire dataset, which was made available for this purpose. The conducted tests allowed the production team to continue the reproduction work on the full dataset.

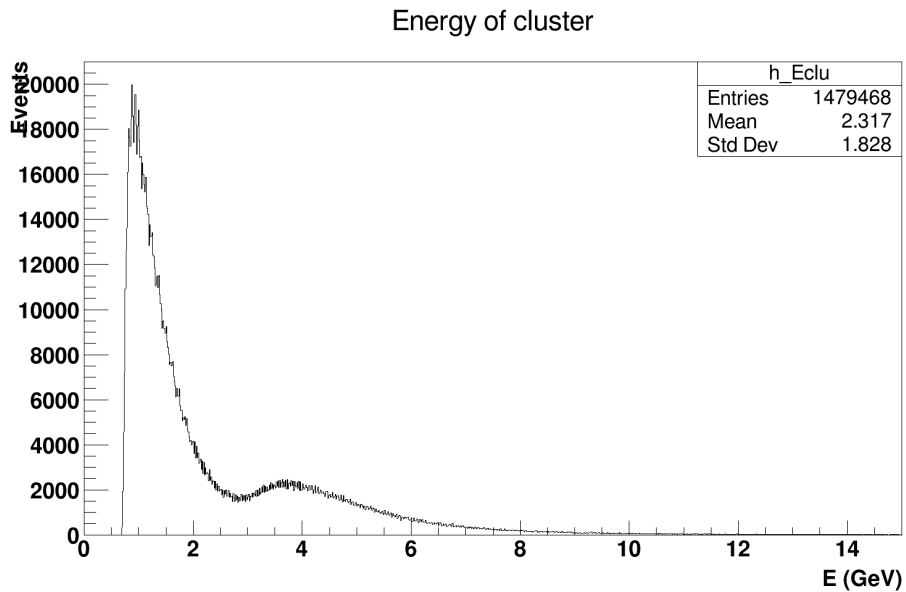


Figure 6.10: The distribution of the energy of a BEMC cluster E_{CLU} .

The Fig. 6.10 shows a distribution of the cluster energy in the BEMC. This is a distribution of all the clusters recorded, therefore the inverse relation between the number of counts and the cluster energy is to be expected. However, one may note the abundance of counts between 3 a 4 GeV. This corresponds to the BHT2*BBCMB trigger threshold, which was used for the QA work.

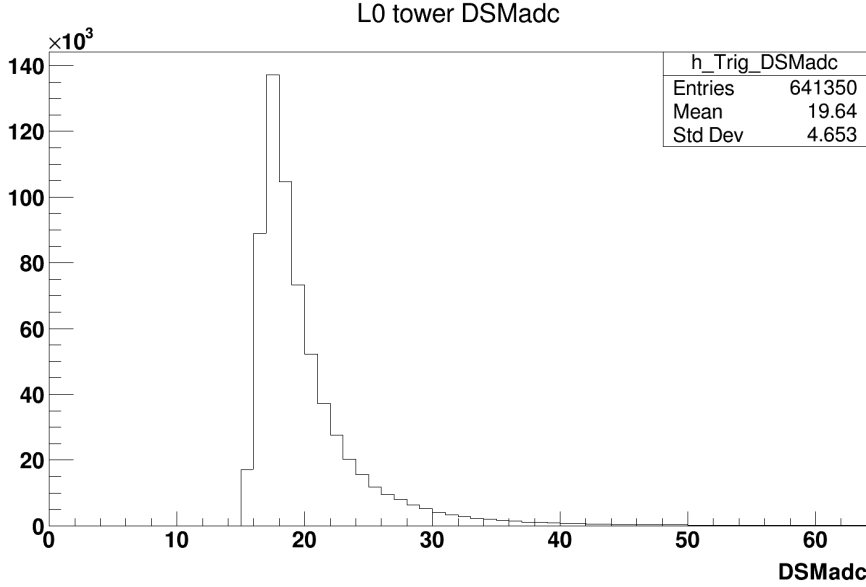


Figure 6.11: The distribution of the triggering tower $DSMadc$.

The quantity $DSMadc$ is the hit energy deposited in a particular tower converted into a 6-bit value. The *adc* stands for Analog to Digital Converter, which is a part of the detector. It reads out the electric signal produced by the detector and converts it to a digital value, which is then stored and further manipulated. This value is used in the L0 trigger to determine whether the event fulfils the trigger condition (for BHT2 in Run17 the $DSMadc$ threshold value was 18). The distribution of the triggering tower $DSMadc$ can be seen on Fig. 6.11, which shows the trigger threshold. This was also studied in dependence on the identification number of the tower $towID$ is order to ensure a uniform distribution and check, whether there are any sectors exhibition anomalies. This is presented in Fig. 6.12.

In Subsection 6.3.4 two quantities are mentioned as a future cuts used in candidate selection. These are the fraction of a tower energy to the energy of a cluster E_{TOW}/E_{CLU} and a ratio of cluster energy to the track momentum E_{CLU}/p . The Fig. 6.13 and Fig. 6.14 show these distributions obtained during the QA process and are included here for illustration.

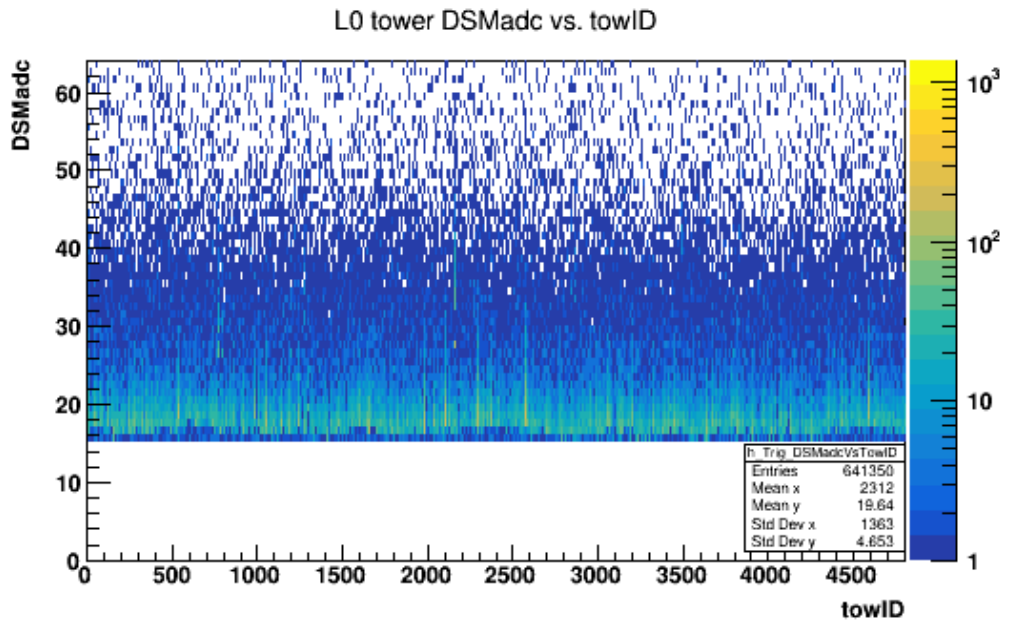


Figure 6.12: The distribution of the triggering tower $DSMadc$ in dependence on the on the identification number of the triggering tower $towerID$.

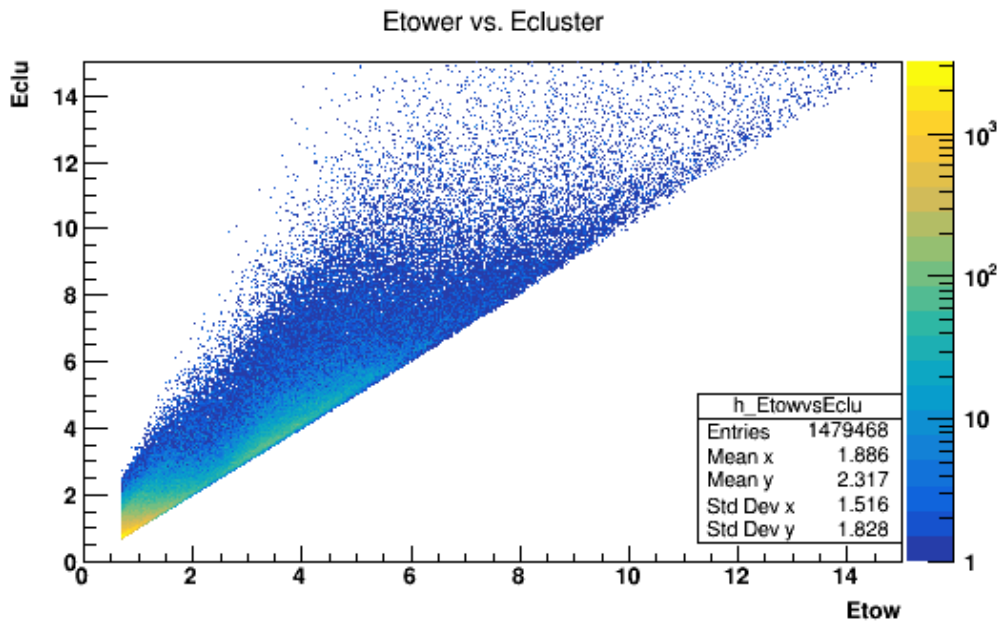


Figure 6.13: The distribution of the energy of a cluster E_{CLU} and the energy deposited to a tower E_{TOW} .

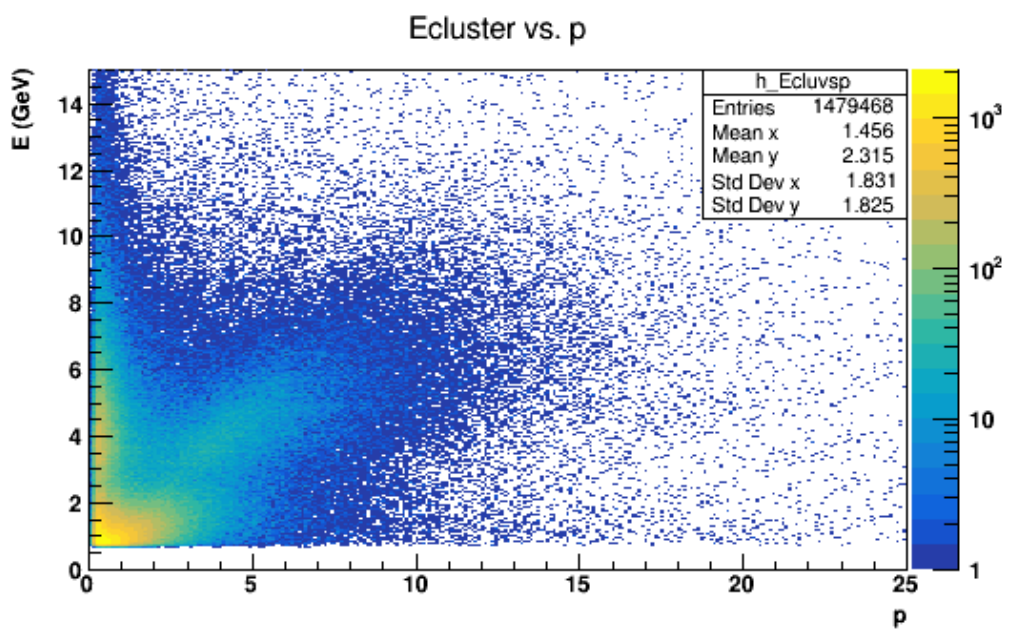


Figure 6.14: The distribution of the energy of a cluster E_{CLU} in dependence on track momentum p .

Chapter 7

Results and discussion

The Run17 510 GeV proton-proton data were analysed. The analysis is successful at selecting events fulfilling the trigger conditions selected as appropriate for Υ study (a required high energy hit) and offer an uniform detector acceptance. Furthermore, the code includes a selection of properly reconstructed primary tracks, while rejecting short, split, pile up or those originating from knock-out from the detector material. Additionally, the analysis implements an electron candidate selection based on TPC information and the subsequent calculation of the invariant mass of like-sign and unlike-sign pairs created from the selected candidates. The spectra are shown in Fig. 6.8. Further cuts can be implemented on the found Υ candidates, which are stored in ROOT trees, which allows for applying additional cuts to optimise signal reconstruction, without having to analyse the entire dataset once again.

The work on the analysis included extensive testing of various cuts combining the available TPC information in a form of $n\sigma_e$ and $n\sigma_\pi$, which are based on the TPC dE/dx , as well as the kinematics of the two electron/positron candidates. However, none have been effective at obtaining a clean and significant Υ meson signal - either the cuts are too broad and include a major pion contamination resulting in any potential signal being lost in the statistical uncertainties, or too strict, which produces a very limited amount of candidates tainted heavily by random fluctuations. It shows, that obtaining Υ signal was not possible with TPC information only and BEMC information is required for the lepton/hadron separation needed to obtain a clean sample of electrons to be used for Υ meson candidate reconstruction.

In order to test the signal reconstruction algorithm a J/ψ signal was used. The cross section of the J/ψ is orders of magnitude higher than the Υ meson's, mainly due to its lower mass (~ 3.096 GeV/ c^2 [6]) and therefore is produced more frequently and may be observed with only TPC information used. The unlike- and like-sign spectra obtained from this validation are shown on Fig. 7.1. One may notice the slight abundance in the unlike-sign invariant mass spectrum around 3.1 GeV/ c^2 when compared to the like-signed. This matches the expectation of the J/ψ meson. After subtracting the like-sign spectrum (used for a combinatorial background estimate) from the unlike-sign spectrum, which contains the signal, the peak should become much more pronounced. This is performed and shown in Fig. 7.2. As per expectations, a peak

is found in the invariant mass region corresponding to the charmonium.

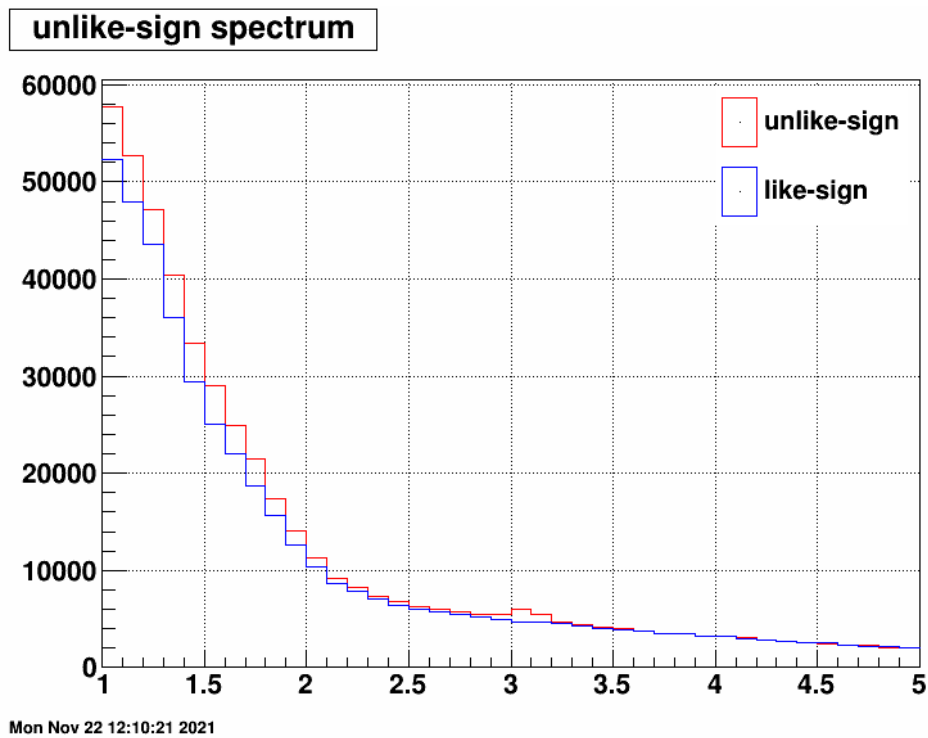


Figure 7.1: The invariant mass spectra for unlike-signed (red) and like-signed (blue) pairs from a J/ψ analysis.

The analysis algorithm with a basic set of kinematic and TPC-based cuts can produce a peak in the region corresponding to the J/ψ meson thanks to its high cross section compared to the Υ meson. This leads the author to the belief, that this code, with the addition to the newly included BEMC information in the new reproduction of the dataset, will be used successfully in order to obtain an Υ signal. The main roadblock at the moment is the absence of a clean electron sample, which will be remedied by the new dataset, which was made available to the RACF users recently.

The author has been involved in the reproduction of the dataset and performed tests on a small sample of BHT2 triggered events. The reproduction included BEMC information, as the tests confirmed, including the E_{CLU} and E_{TOW} , the two values believed to be sufficient to separate the pions from the relativistic electrons. Thanks to this work the production could continue, but the dataset wasn't available in time to complete the Υ signal reconstruction.

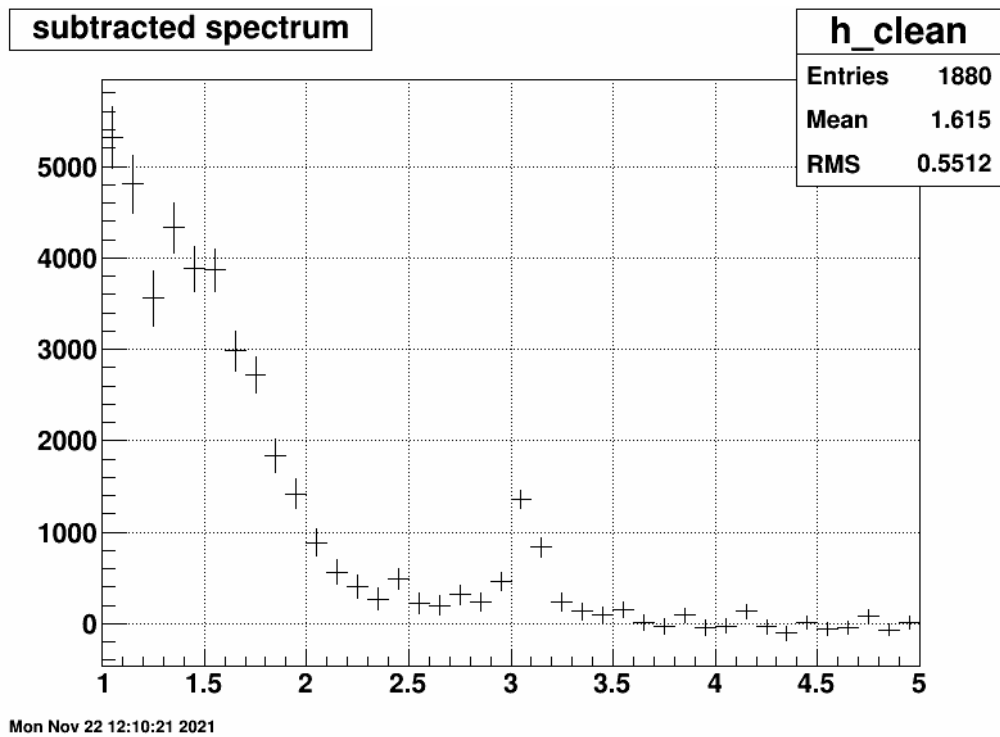


Figure 7.2: The invariant mass spectrum for from a J/ψ analysis after background subtraction.

Conclusion

This thesis presented an overview of the Υ meson yield dependence on charged particle event multiplicity analysis of proton-proton collisions at 510 GeV centre-of-mass energy at the RHIC collider. The event selection, track selection, electron identification, multiplicity measurement and pair reconstruction stages of the process were introduced and discussed. The analysis is capable of identifying an electron-positron pair and estimate the combinatorial background.

The dataset available to the author during the work on the thesis did not include the BEMC information and therefore the analysis relied purely on TPC information and kinematic variables to identify electrons. At the high energies, which are necessary for Υ meson reconstruction, the TPC is inadequate for electron hadron separation. Nevertheless, the analysis was used to try and obtain a J/ψ signal, which should be easier to find than the Υ signal due to the charmonium's larger cross section. This was an attempt to verify, that the analysis was able to perform a signal reconstruction from found electron candidates. An indication of J/ψ signal was observed, which confirms the signal reconstruction is one correctly. The BEMC information is essential in reconstructing and obtaining the Υ signal.

Author's contribution towards the quality assurance of the reproduction of the data, which was done in order to fix the unavailability of the BEMC information necessary for obtaining a pure electron sample needed to properly reconstruct Υ mesons from the dielectron channel, was listed. The author tested a small subset of the data, which was made available for testing, and verified the presence of BEMC information in the newly reproduced data.

The points 5 and 6 in the thesis assignment were not completed due to missing BEMC information in the original dataset. This is mainly due to external reasons beyond the author's influence, described in the thesis in more detail. However, in order to solve this and speed up the reconstruction of the data, the author provided QA tests mentioned above. Because of this unfortunate situation more time was invested in the Monte Carlo studies.

A Monte Carlo study performed using the PYTHIA event generator of the same measurement was performed. This was a continuation and extension done in the author's bachelor thesis. The study focused on investigating the difference between the $\Upsilon(1S)$, $\Upsilon(2S)$ and $\Upsilon(3S)$ states and the contribution of the feed-down interactions. There were no major differences found between the various Υ states with regards

to multiplicity spectra and the dependence of their yield on the multiplicity. The consequence of the feed-down effect was observed. It is apparent the multiplicity spectra, as the $\Upsilon(1S)$ and $\Upsilon(2S)$ states are produced either directly or via feed-down, but no major influence on the yield in relation to multiplicity was found. The feed-down contribution may warrant a more thorough study due to the values of the long distance matrix elements of the χ_b states included in PYTHIA. This caused the largest yield of χ_{b2} , which has the highest mass of the χ_b , whereas the lightest χ_{b0} should be the easiest to produce. This is unexpected and may need to be verified by experimental data.

The thesis also discusses the utilisation of the BEMC data from the newly acquired dataset towards the further development of the analysis by introducing the cuts, which should aid in obtaining a pure electron sample needed to observe an Υ meson signal.

Bibliography

- [1] D. Croon et al. “GUT Physics in the Era of the LHC”. *Frontiers in Physics* 7 (2019).
- [2] M. Chown. *What is the standard model?* 2020. URL: <https://www.sciencefocus.com/science/what-is-the-standard-model/>.
- [3] R. Hagedorn. “Statistical thermodynamics of strong interactions at high-energies”. *Nuovo Cim. Suppl.* 3 (1965), pp. 147–186.
- [4] R. Aaij et al. “Observation of New Resonances Decaying to $J/\psi K^+$ and $J/\psi \phi$ ”. *Phys. Rev. Lett.* 127.8 (2021).
- [5] R. Aaij et al. “Observation of $J/\psi p$ Resonances Consistent with Pentaquark States in $\Lambda_b^0 \rightarrow J/\psi K^- p$ Decays”. *Phys. Rev. Lett.* 115.7 (2015).
- [6] P.A. Zyla et al. “Review of Particle Physics”. *PTEP* 2020.8 (2020), p. 083C01.
- [7] Y. Fukuda et al. “Evidence for oscillation of atmospheric neutrinos”. *Phys. Rev. Lett.* 81 (1998), pp. 1562–1567.
- [8] M. Aker et al. “Direct neutrino-mass measurement with sub-electronvolt sensitivity”. *Nat. Phys.* 18.2 (2022), pp. 160–166.
- [9] G. Aad et al. “Observation of a new particle in the search for the Standard Model Higgs boson with the ATLAS detector at the LHC”. *Phys. Lett. B* 716.1 (2012), pp. 1–29.
- [10] A.M. Sirunyan et al. “A measurement of the Higgs boson mass in the diphoton decay channel”. *Phys. Lett. B* 805 (2020), p. 135425.
- [11] K. Tanabe and H. Sugawara. “G-Parity and Unitary Symmetry”. *Prog. Theor. Phys.* 32.6 (1964), pp. 911–921.
- [12] A. Andronic et al. “Heavy-flavour and quarkonium production in the LHC era: from proton–proton to heavy-ion collisions”. *Eur. Phys. J. C* 76.3 (2016).
- [13] C. Biino. “CMS quarkonium Production at 13 TeV”. *J. Phys. Conf. Ser.* 1137 (2019), p. 012030.
- [14] C. H. Chang. “Hadronic production of J/ψ associated with a gluon”. *Nucl. Phys. B* 172 (1979), 425–434. 17 p.
- [15] R. Baier and R. Ruckl. “Hadronic Production of J/ψ and Upsilon: Transverse Momentum Distributions”. *Phys. Lett. B* 102 (1981), pp. 364–370.
- [16] E. L. Berger and D. L. Jones. “Inelastic Photoproduction of J/ψ and Upsilon by Gluons”. *Phys. Rev. D* 23 (1981), pp. 1521–1530.

- [17] G. T. Bodwin et al. “ P -wave charmonium production in B -meson decays”. *Phys. Rev. D* 46.9 (1992), R3703–R3707.
- [18] G. T. Bodwin, E. Braaten, and G. P. Lepage. “Rigorous QCD analysis of inclusive annihilation and production of heavy quarkonium”. *Phys. Rev. D* 51 (3 1995), pp. 1125–1171.
- [19] G. T. Bodwin, E. Braaten, and G. P. Lepage. “Erratum: Rigorous QCD analysis of inclusive annihilation and production of heavy quarkonium [Phys. Rev. D 51, 1125 (1995)]”. *Phys. Rev. D* 55 (9 1997), pp. 5853–5854.
- [20] M. Butenschoen and B. A. Kniehl. “World data of J/ψ production consolidate nonrelativistic QCD factorization at next-to-leading order”. *Phys. Rev. D* 84.5 (2011).
- [21] H. Fritzsch. “Producing Heavy Quark Flavors in Hadronic Collisions: A Test of Quantum Chromodynamics”. *Phys. Lett. B* 67 (1977), pp. 217–221.
- [22] V. D. Barger, W.-Y. Keung, and R. J. N. Phillips. “On psi and Upsilon Production via Gluons”. *Phys. Lett. B* 91 (1980), pp. 253–258.
- [23] V. Barger, W. Y. Keung, and R. J. N. Phillips. “Hadroproduction of ψ and Υ ”. *Z. Phys. C Part. Fields* 6.2 (1980), pp. 169–174.
- [24] R. E. Nelson, R. Vogt, and A. D. Frawley. “Narrowing the uncertainty on the total charm cross section and its effect on the J/ψ cross section”. *Phys. Rev. C* 87.1 (2013), p. 014908.
- [25] R. Vogt. “Shadowing effects on J/ψ and Υ production at energies available at the CERN Large Hadron Collider”. *Phys. Rev. C* 92.3 (2015), p. 034909.
- [26] Y.-Q. Ma and R. Vogt. “Quarkonium production in an improved color evaporation model”. *Phys. Rev. D* 94.11 (2016).
- [27] Z.-B. Kang, Y.-Q. Ma, and R. Venugopalan. “Quarkonium production in high energy proton-nucleus collisions: CGC meets NRQCD”. *JHEP* 01 (2014), p. 056.
- [28] F. Gelis et al. “The Color Glass Condensate”. *Annu. Rev. Nucl. Part. Sci.* 60.1 (2010), pp. 463–489.
- [29] J. D. Bjorken. “CURRENT ALGEBRA AT SMALL DISTANCES”. *Conf. Proc. C* 670717 (1967), pp. 55–81.
- [30] J. D. Bjorken. “Asymptotic Sum Rules at Infinite Momentum”. *Phys. Rev.* 179 (5 1969), pp. 1547–1553.
- [31] Y.-Q. Ma and R. Venugopalan. “Comprehensive Description of J/ψ Production in Proton-Proton Collisions at Collider Energies”. *Phys. Rev. Lett.* 113.19 (2014), p. 192301.
- [32] M. Gyulassy. *The QGP Discovered at RHIC*. 2004. DOI: 10.48550/ARXIV.NUCL-TH/0403032.
- [33] S. Chatrchyan et al. “Observation of Sequential Υ Suppression in PbPb Collisions”. *Phys. Rev. Lett.* 109 (22 2012), p. 222301.
- [34] Ziwei Lin and C.M. Ko. “ Υ absorption in hadronic matter”. *Physics Letters B* 503.1 (2001), pp. 104–112. ISSN: 0370-2693.

- [35] S. Gavin and R. Vogt. “Charmonium Suppression by Comover Scattering in $Pb + Pb$ Collisions”. *Phys. Rev. Lett.* 78 (6 1997), pp. 1006–1009.
- [36] S. Gavin et al. “ J/ψ suppression as evidence for high densities in nuclear collisions”. *Z. Phys. C Part. Fields* 61.2 (1994), pp. 351–355.
- [37] R. Vogt. “Shadowing effects on J/ψ and Υ production at energies available at the CERN Large Hadron Collider”. *Phys. Rev. C* 92 (3 2015), p. 034909.
- [38] P. Bartalini et al. *Multi-Parton Interactions at the LHC*. 2011. DOI: 10.48550/ARXIV.1111.0469.
- [39] H. Abramowicz et al. “Combination of measurements of inclusive deep inelastic $e^\pm p$ scattering cross sections and QCD analysis of HERA data”. *Eur. Phys. J. C* 75.12 (2015), p. 580.
- [40] J. Adam et al. “Measurement of charm and beauty production at central rapidity versus charged-particle multiplicity in proton-proton collisions at $\sqrt{s}=7$ TeV”. *J. High Energy Phys.* 2015.9 (2015), p. 148.
- [41] E. Levin and M. Siddikov. “ J/ψ production in hadron scattering: three-pomeron contribution”. *Eur. Phys. J. C* 79.5 (2019), p. 376.
- [42] E. Levin, I. Schmidt, and M. Siddikov. “Multiplicity dependence of quarkonia production in the CGC approach”. *Eur. Phys. J. C* 80.6 (2020), p. 560.
- [43] E. G. Ferreira and C. Pajares. “High multiplicity pp events and J/ψ production at energies available at the CERN Large Hadron Collider”. *Phys. Rev. C* 86 (3 2012), p. 034903.
- [44] J. Adam et al. “ J/Ψ production cross section and its dependence on charged-particle multiplicity in $p + p$ collisions at $s=200$ GeV”. *Phys. Lett. B* 786 (2018), pp. 87–93.
- [45] U. A. Acharya et al. “ J/ψ and $\psi(2S)$ production at forward rapidity in $p + p$ collisions at $\sqrt{s} = 510$ GeV”. *Phys. Rev. D* 101 (5 2020), p. 052006.
- [46] J. Adam et al. “Measurements of the transverse-momentum-dependent cross sections of J/ψ production at mid-rapidity in proton + proton collisions at $\sqrt{s} = 510$ and 500 GeV with the STAR detector”. *Phys. Rev. D* 100 (5 2019), p. 052009.
- [47] S. Acharya et al. “Inclusive J/Ψ production at mid-rapidity in pp collisions at $\sqrt{s} = 5.02$ TeV”. *Jour. High Energy Phys.* 2019.10 (2019). ISSN: 1029-8479. DOI: 10.1007/jhep10(2019)084. URL: [http://dx.doi.org/10.1007/JHEP10\(2019\)084](http://dx.doi.org/10.1007/JHEP10(2019)084).
- [48] L. Kosarzewski. “Overview of quarkonium production studies at the STAR experiment”. *J. Phys. Conf. Ser.* 1667 (2020), p. 012022.
- [49] L. Kosarzewski. “Recent results of Upsilon production measured with the STAR experiment”. 20th Conference of Czech and Slovak Physicists. 2020. URL: <https://drupal.star.bnl.gov/STAR/presentations/20th-conference-czech-and-slovak-physicists/recent-results-epsilon-production-measured>.

- [50] V. Khachatryan et al. “Measurements of the $\Upsilon(1S)$, $\Upsilon(2S)$, and $\Upsilon(3S)$ differential cross sections in pp collisions at $\sqrt{s}=7\text{TeV}$ ”. *Phys. Lett. B* 749 (2015), pp. 14–34. ISSN: 0370-2693.
- [51] J. Adam et al. “ J/ψ production cross section and its dependence on charged-particle multiplicity in p+p collisions at $\sqrt{s} = 200 \text{ GeV}$ ”. *Phys. Lett. B* 786 (2018), pp. 87–93. ISSN: 0370-2693.
- [52] B. Patel and V. Chackara. “Properties of $QQ(Q \in b, c)$ mesons in Coulomb plus power potential (CPP ν)”. *J. Phys. G: Nucl. Part. Phys.* 36 (Jan. 2009), p. 035003.
- [53] S. Acharya et al. “Multiplicity dependence of inclusive J/ψ production at midrapidity in pp collisions at $\sqrt{s} = 13 \text{ TeV}$ ”. *Phys. Lett. B* 810 (2020), p. 135758. ISSN: 0370-2693.
- [54] L. Kosarzewski. “Overview of Υ production studies performed with the STAR experiment”. *PoS ICHEP2020* (2021), p. 545. DOI: 10.22323/1.390.0545.
- [55] W. Shaikh. *Recent bottomonium measurements in pp, p-Pb and Pb-Pb collisions at forward rapidity with ALICE at the LHC*. 2021. arXiv: 2103.13685 [hep-ex].
- [56] Y. Yang. “The STAR detector upgrades for the BES II and beyond physics program”. *Nucl. Phys. A* 1005 (2021). The 28th International Conference on Ultra-relativistic Nucleus-Nucleus Collisions: Quark Matter 2019, p. 121758. ISSN: 0375-9474.
- [57] C. Aidala et al. “sPHENIX: An Upgrade Concept from the PHENIX Collaboration” (2012). arXiv: 1207.6378 [nucl-ex].
- [58] A. Accardi et al. *Electron Ion Collider: The Next QCD Frontier - Understanding the glue that binds us all*. 2012. DOI: 10.48550/ARXIV.1212.1701.
- [59] *Start-up of 22nd run at the relativistic heavy ion collider (RHIC)*. 2021. URL: <https://www.bnl.gov/newsroom/news.php?a=119262>.
- [60] M. Harrison, T. Ludlam, and S. Ozaki. “RHIC project overview”. *Nucl. Instrum. Meth. A* 499 (2003), pp. 235–244.
- [61] K.H. Ackermann et al. “STAR detector overview”. *Nucl. Instrum. Meth. A* 499 (2003), pp. 624–632.
- [62] D. Arkhipkin and J. Lauret. “STAR Online Meta-Data Collection Framework: Integration with the Pre-existing Controls Infrastructure”. *J. Phys. Conf. Ser.* 898 (2017), p. 032023.
- [63] M. Anderson et al. “The STAR time projection chamber: a unique tool for studying high multiplicity events at RHIC”. *Nucl. Instrum. Meth. A* 499.2 (2003), pp. 659–678.
- [64] C. Yang. “The STAR beam energy scan phase II physics and upgrades”. *Nucl. Phys. A* 967 (2017), pp. 800–803.
- [65] M. Beddo et al. “The STAR barrel electromagnetic calorimeter”. *Nucl. Instrum. Meth. A* 499 (2003), pp. 725–739.

- [66] W.J. Llope et al. “The TOFP/pVPD time-of-flight system for STAR”. *Nucl. Instrum. Meth. A* 522.3 (2004), pp. 252–273.
- [67] W.J. Llope et al. “The STAR Vertex Position Detector”. *Nucl. Instrum. Meth. A* 759 (2014), pp. 23–28.
- [68] C. A. Whitten. “The beam-beam counter: A local polarimeter at STAR”. *AIP Conf. Proc.* 980.1 (2008), pp. 390–396.
- [69] T. Sjöstrand et al. “An introduction to PYTHIA 8.2”. *Comput. Phys. Commun.* 191 (2015), pp. 159–177.
- [70] M. Bähr et al. “Herwig++ physics and manual”. *Eur. Phys. J. C* 58.4 (2008), pp. 639–707.
- [71] J. Bellm et al. “Herwig 7.0/Herwig++ 3.0 release note”. *Eur. Phys. J. C* 76.4 (2016), p. 196.
- [72] J. Češka. “Fyzika těžkých kvarků v jádro-jaderných srážkách”. Fakulta jaderná a fyzikálně inženýrská ČVUT v Praze, 2020.
- [73] B. Andersson et al. “Parton fragmentation and string dynamics”. *Phys. Rep.* 97.2 (1983), pp. 31–145.
- [74] P. Nason et al. *Bottom Production*. 2000. DOI: 10.48550/ARXIV.HEP-PH/0003142.
- [75] M. Bargiotti and V. Vagnoni. *Heavy Quarkonia sector in PYTHIA 6.324: tuning, validation and perspectives at LHC(b)*. Tech. rep. Geneva: CERN, 2007. URL: <https://cds.cern.ch/record/1042611>.
- [76] L. Kosarzewski. “Overview of quarkonium production studies at the STAR experiment”. *J. Phys. Conf. Ser.* 1667 (2020), p. 012022.
- [77] R. Brun and F. Rademakers. “ROOT — An object oriented data analysis framework”. *Nucl. Instrum. Meth. A* 389.1 (1997). *New Computing Techniques in Physics Research V*, pp. 81–86.
- [78] *SDCC - Scientific Data and computing center*. URL: <https://www.sdcc.bnl.gov/>.
- [79] Y. Xu et al. “Improving the calibration of the STAR TPC for the high- hadron identification”. *Nucl. Instrum. Meth. A* 614.1 (2010), pp. 28–33.